ELECTRONIC STRUCTURE OF HIGHLY-CORRELATED LOW-DIMENSIONAL ORGANIC CONDUCTORS

Dissertation

zur Erlangung des Grades
„Doktor der Naturwissenschaften“
am Fachbereich Physik, Mathematik und Informatik
der Johannes Gutenberg-Universität
in Mainz

vorgelegt von
Alisa Chernenkaya
Geboren in Novovoronezh (UdSSR)
Mainz, 2016

Dekanin:

Gutachter 1:
Gutachter 2:

Datum der Prüfung: 15. Juni 2016

Die vorliegende Arbeit wurde in der Zeit von Januar 2013 bis Januar 2016 am Institut für Physik im Fachbereich Physik, Mathematik und Informatik der Johannes Gutenberg-Universität, Mainz unter der Leitung von Herrn Prof. Dr. Gerd Schönhense angefertigt.

Mainz, 2016

Hiermit versichere ich, dass ich die vorliegende Dissertation selbstständig verfasst und keine anderen als die angegebenen Hilfsmittel benutzt habe. Alle der Literatur entnommenen Stellen sind als solche gekennzeichnet.

Mainz, 2016

Zusammenfassung

Organische Leiter sind eine große Klasse von niederdimensionalen Materialien mit starken elektronischen Korrelationseffekten, die viele verschiedene grundlegende Phänomene aufweisen. Einige dieser Materialen sind attraktiv für einen breiten Industrieeinsatz als Komponenten für organische Elektronik und alternative Energietechnik. Alle von ihnen sind sehr interessant für die Grundlagenforschung, weil diese Materialien eine Vielzahl besonderer Phänomene aufweisen und nicht natürlich auftreten. Die vorliegende Arbeit beschäftigt sich mit grundlegenden Fragen zur Untersuchungen der elektronischen Struktur und ihrer Korrelation mit anderen bekannten Eigenschaften der organischen Materialien. Um dieses Ziel zu erreichen, wurde die Phasencharakteristik des organischen Komplexes $(DOEO)_4[HgBr_4]\cdot TCE$ auf Basis von spektroskopischen Daten (Röntgenabsorption und Photoelektronenspektroskopie mit Synchrotronstrahlung im Nieder- und Hochenergiebereich) im Vergleich mit elektrischem Widerstand, magnetischer Suszeptibilität und Elektronenspinresonanz untersucht. Darüber hinaus wurde die elektronische Struktur der unbesetzten Bänder in Kristallen des organischen Metalls TTF-TCNQ untersucht. Bei der Abkühlung tritt eine markante Änderung der elektronischen Zustände auf. Kurz vor dem Peierls Phasenübergang wurden strukturelle Fluktuationen des Akzeptors (Pyramidalisierung von TCNQ) beobachtet. Zwei weitere organische Komplexe mit Ladungstransfer: DTBDT-TCNQ und DTBDT-F_4TCNQ wurden mittels kantennaher Röntgenabsorption (NEXAFS) untersucht. Durch Vergleich mit systematischen Berechnungen (der Gruppe R. Valentí, Universität Frankfurt (M)) konnte der Einfluß des Loches in der inneren Schale erstmalig quantiziert werden. Dies führte zu einer Neuzuordnung der Röntgenabsorptionssignale.

Abstract

Organic conductors are a large class of strongly-correlated low-dimensional materials, exhibiting a variety of fundamental phenomena. Some of these materials are close to wide implementation in industry as components for electronics and alternative power engineering. All of the organic conductors are interesting for fundamental research because of their variety of phenomena and because these materials do not occur naturally. The present work addresses the fundamental questions of electronic structure investigations and their correlation with other known properties of the organic materials. Following this goal, the phase characterization of the $(DOEO)_4[HgBr_4]\cdot TCE$ organic charge transfer complex was performed based on spectroscopic data (X-ray absorption and photoelectron spectroscopy using soft and hard X-rays from synchrotron sources) compared to resistivity, magnetic susceptibility and electron spin resonance. Furthermore, observed changes of the electronic structure of the unoccupied states in TTF-TCNQ organic metal crystals, which develop with cooling, suggest band gap opening at the Peierls transitions. Additionally, pre-transitional structural fluctuation of the acceptor (pyramidalization of TCNQ) was observed. Two more charge transfer organic complexes were investigated in scope of the present work using X-ray absorption: DTBDT-TCNQ and DTBDT-F_4TCNQ. Comparison of the X-ray absorption spectra with theoretical calculations (performed in the group of R. Valentí, University of Frankfurt (M)) reveals and quantifies the strong effect of the core-hole that leads to a reassignment of the X-ray absorption signals.

„Erfolg hat drei Buchstaben: TUN“

-Johann Wolfgang von Goethe

Contents

1. Introduction

Organic conductors are a fascinating class of materials which are characterized by low dimensionality and relatively low concentration of charge carriers and, therefore, show the existence of strong electron correlations and various phase transitions. For example, spin-Peierls transitions [1], Mott metal-insulator transitions [2], charge ordering [3], Wigner crystallization [4], photo-induced transitions [5], multi-functionality [6], spin-liquid phases[7], metallicity [8], superconductivity [9] and even multiferroicity [10] could exist in these systems. Mostly, such phenomena appear due to contact between donor and acceptor molecules in the material's crystal structure. Such an intriguing spectrum of possible physical properties is very interesting for fundamental science. Synthetic conductors (all the organic conductors are synthetic and do not exist in nature) are a highly exciting field of research also due to the possibility of not only investigating electron correlations, but also to tune them by slight deviations during the chemical synthesis process. It is especially important for possible industrial applications to obtain easy access for manipulating the degree of charge transfer or the phase transition temperature or any other parameters of the system, for example, by adding or changing one or several atoms in the crystal structure. In particular, organic electronics are prototyped and developed based on small molecules of organic conductors. The fastest developing branches of current applications are organic field-effect transistors (OFETs), organic light emitting diodes (OLEDs) and organic photovoltaic cells (OPVs).

Within the scope of this Thesis, several organic conductors of different dimensionality and their electronic properties are discussed. Usually it is relatively easy to investigate the transport or magnetic properties of the charge-transfer crystals, and much more complicated to measure experimentally and discuss their electronic structure. This is in spite of the fact that the electronic structure and its changes drive physical properties and phase transitions in real compounds. Therefore, experimental studies of electronic properties are not very common, however, they could help to understand the relation between spin, charge and lattice degrees of freedom and discuss the observed correlations. As it was shown recently in our group, photoemission and X-ray absorption synchrotron techniques are very powerful and they open additional pathways for the investigation of charge carrier behavior when the system changes with cooling [11], [12]. The high sensitivity of these methods and good spectrometer resolution allowed us to discuss features in the occupied and unoccupied density of electronic states in the studied materials very precisely.

Following this short introduction, the present Thesis is divided into eight chapters, as follows:

- ***Chapter 2*** is about the basic theoretical aspects of phenomena discussed in the present Thesis. Several examples of the large class of organic conductors with their main properties are illustrated. Additionally, the fundamental knowledge about the instabilities and transport in organics is recalled. Also, Peierls and Mott metal-insulator, neutral-ionic and charge ordering phase transitions are discussed.
- ***Chapter 3*** describes experimental techniques used in the present work, namely photoemission methods with different excitation sources, ranging from vacuum ultraviolet to hard X-rays, near-edge X-ray absorption, infrared spectroscopy and SQUID magnetometry. In this chapter, the most important details on the measuring processes and data evaluation are discussed. In addition, the theoretical calculations used in the present work are briefly discussed.
- ***Chapter 4*** deals with the experimental results of the investigation of the correlation of electronic and magnetic properties of the two-dimensional organic conductor $(DOEO)_4[HgBr_4]$ are shown. The chapter gives an overview of the state of the art for this compound and additionally provides new information on the possible phases existing in the novel material.
- ***Chapter 5*** is dedicated to the quasi-one-dimensional charge transfer compound TTF-TCNQ investigated by temperature-dependent X-ray absorption spectroscopy. The correlation between charge and lattice distortion crossing the Peierls transition temperature is discussed.

- ***Chapter 6*** is about the properties of two novel organic complexes based on the thiophene derivative DTBDT as donor and two different well-known acceptors TCNQ and F_4TCNQ and the comparison between their charge-transfer mechanisms are presented and discussed. The comparison of the X-ray absorption spectra with systematic ab-initio calculations (R. Valentí et al., University of Frankfurt (M)) revealed the important role of the core hole in the excitation process and led to a new assignment of the absorption signals of the acceptor.
- ***In chapter 7*** the main results and conclusions of the present work are summarized.
- ***Chapter 8*** presents perspectives of the spectroscopic approach on organic conductors and an outlook is given on future experiments.

2. Basics and theoretical background

In this chapter, a brief overview of the main features and properties of low-dimensional organic conductors is recalled from literature. The phase diagrams and discussions on ground state properties are provided as well. The most intriguing and investigated phenomenon in the class of organic conductors, currently, is the correlation of the electronic structure and the transport/magnetic/optical properties of the crystals. These correlations are discussed in more detail.

2.1. Low-dimensional organic conductors and superconductors

The first theoretical prediction of possible organic superconductivity was published by W. A. Little in 1964 [13]. The main idea was to create a new type of compound where π-like molecular orbitals are involved to the charge transport rather than atomic orbitals. In other words, new compounds were supposed to have unsaturated bonds or aromatic rings to be able to transfer charge. After years of extensive synthetic work, it was possible to obtain crystals of organic charge transfer compounds where the conductivity was of almost the same order of magnitude as in solid inorganic metals. Fig. 2.1. shows the comparison of several inorganic and organic conductors and insulators. The chemical formulas of the previously mentioned compounds and some others used for synthetic metals are depicted in Fig. 2.2.

The charge transfer salt TTF-TCNQ, where TTF = tetrathiafulvalene is the donor molecule and TCNQ = tetracyanoquinodimethane is the acceptor molecule, was the first successfully synthesized conductive organic crystal. In this example the quasi-one-dimensional compound consists of stacks of both donor and acceptor molecules tilted with respect to the *b* axis and in opposite direction along the *a* axis **[14]**. Both TTF and TCNQ molecules are flat and both donor (by π-HOMO, HOMO = highest occupied molecular orbital) and acceptor (by π-LUMO, LUMO = lowest unoccupied molecular orbital) contribute to the conductivity of the crystal. Remarkably, π-HOMO and π-LUMO in this case are mostly associated with a particular molecule as a whole rather than with separate atoms. Therefore, the molecular orbitals of donors and acceptors overlap, respectively, in chains, providing strong anisotropy of charge mobility and being consequently a 1D conductor.

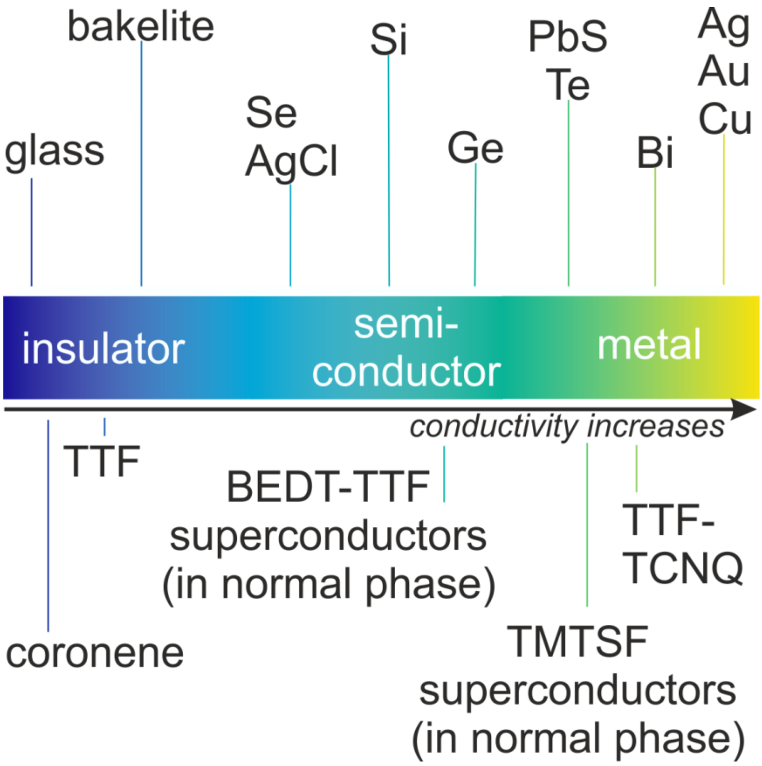

Figure 2.1. Schematic representation of the comparison of room temperature conductivity between inorganic solids (above) and organic charge transfer and single component compounds (adopted from [15]).

Up to now, the attempts to synthesize new compounds with more suitable properties oriented to the application are still demanding. They aim to control the self-assembling ability, electron correlation, and dimensionality in order to get the desired ground state and physical properties of the new materials. Since the discovery of organic conductivity, more than two thousand metallic and highly conductive organic compounds have been synthesized [15]. Fig. 2.3 illustrates the development and evolution of superconducting charge transfer complexes with their transition temperatures to the superconducting ground state in comparison to other classes of superconducting materials.

The most important issue for the successful engineering of a new compound with the desired properties is the choice of precursors – donor (D) and acceptor (A) molecules. When the novel compound forms, the HOMO of the donor and the LUMO of the acceptor become electronically coupled and therefore a partial charge transfer ρ arises. As a result, the ground state of the novel compound will be characterized by a partial ionicity $D^{\rho+}A^{\rho-}$. Depending on the donor's ionization potential I_D and acceptor's electron affinity E_A, the resulting degree of ionicity (meaning the degree of charge transfer) will be different.

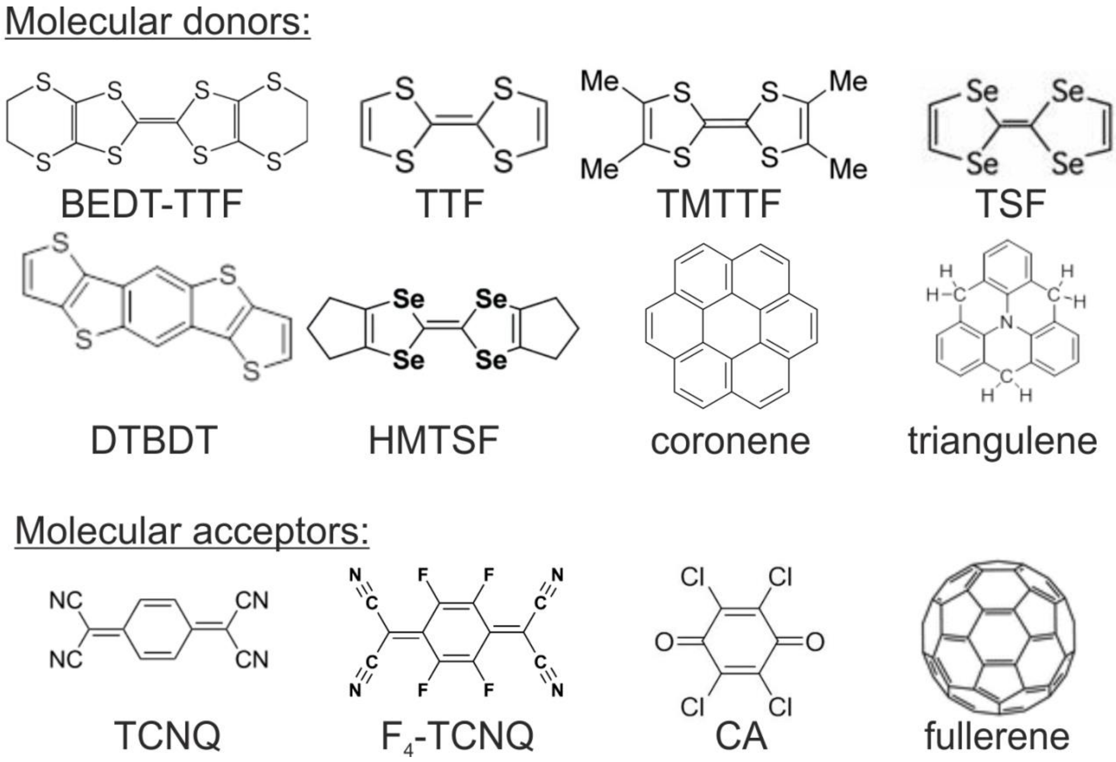

Figure 2.2. Skeletal structures of several organic donors: bis(ethylenedithio)tetrathiafulvalene (BEDT-TTF), tetrathiafulvalene (TTF), tetramethyltetrathiafulvalene (TMTTF), tetraselenefulvalene (TSF), dithienobenzodithiophene (DTBDT), hexamethylenetetraselenafulvalene (HMTSF), coronene, triangulene and acceptors: tetracyanoquinodimethane (TCNQ), tetracyanotetrafluoroquinodimethane (F_4TCNQ), tetrachloro-*p*-benzoquinone (CA), fullerene including those discussed in the present work.

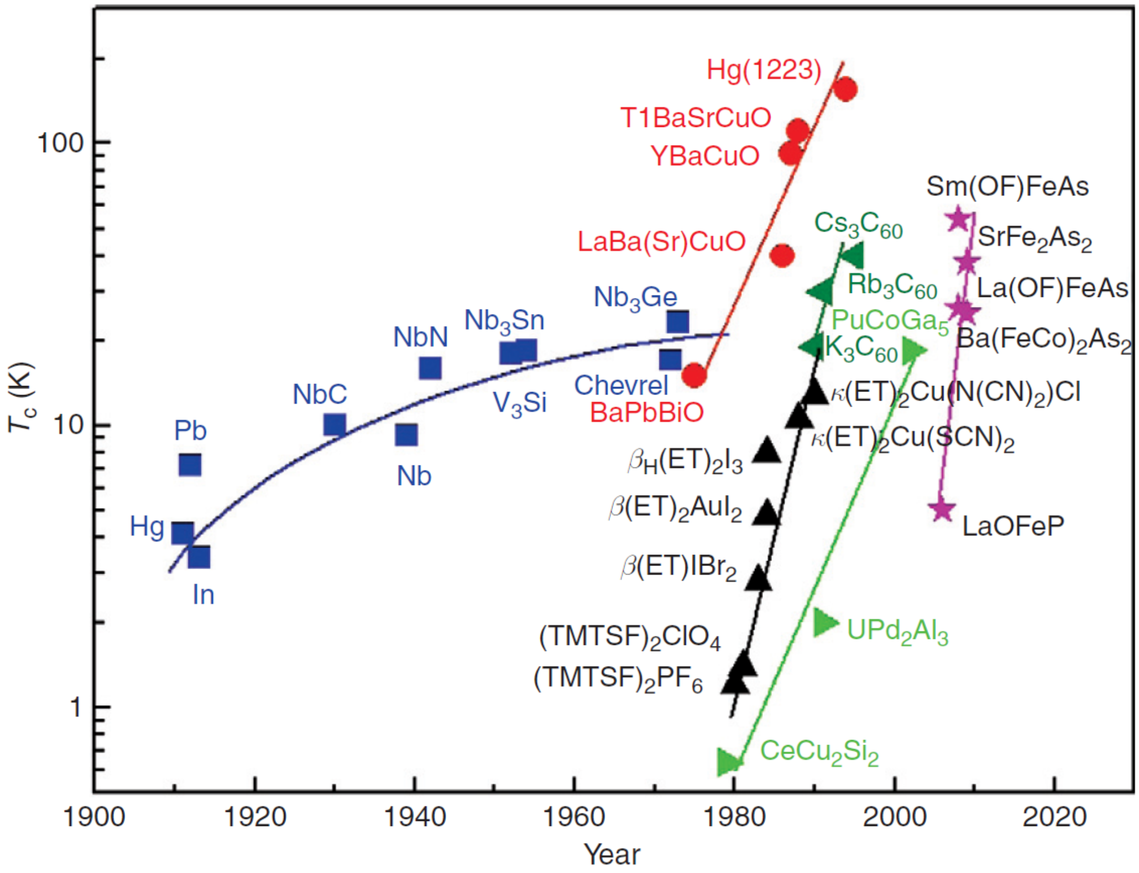

Figure 2.3. The evolution of T_c in materials according to the date of the discovery of their superconducting properties in comparison with other classes of superconductors (from [9]).

Taking into account the possible tuning of the ground state and therefore band structure manipulation, the opportunity to design novel compounds is very attractive. Fig. 2.4 represents the scheme of possible band structure engineering of a triangulene donor molecule and TCNQ acceptor molecule (their structures are shown in Fig. 2.2). At the stage of planning a future novel compound, one should first choose D and A in such a way that the quantities I_D and E_A have necessary values for the expected resulting charge transfer amount in the new compound. As follows from Fig. 2.4, the valence band of the complex is centered mostly on the D, while the conduction band is centered on the A, resulting in the defined shapes of HOMO and LUMO of the complex [16].

To synthesize a new charge transfer complex from precursors that meets the requirements of predicted band structure, four main techniques are usually used: solution growth, electrocrystallization, vapor transport, and thin film deposition. Single crystals usually have better quality and have a lower concentration of defects and therefore are more suitable for fundamental research, while thin films of charge transfer complexes are mostly oriented to the application in industry.

In the molecular growth from solution method, pure compounds of donor and acceptor precursors are dissolved in the same or in different solvents. The crystals of the charge transfer compound are formed during evaporation of the liquid solvents [17].

The electrocrystallization method requires a H-shaped cell with two platinum electrodes on both sides, where solutions of the donor and acceptor precursors are separated by a glass filter. By applying a certain electrical current, the charge transfer complex will be formed on one electrode [18]. Depending on the temperature of the system, the concentration and the current value, it is possible to control the morphology of the growing crystals.

Crystal growth by vapor transport requires a quartz ampoule where parent materials are placed in an oven that will continuously produce a temperature gradient inside this quartz tube [19]. At first, the pure donor and acceptor are sublimated, and then they are moved by convection currents inside the tube to cooler region and re-crystallize to the charge transfer complex in the form of powder or single crystals.

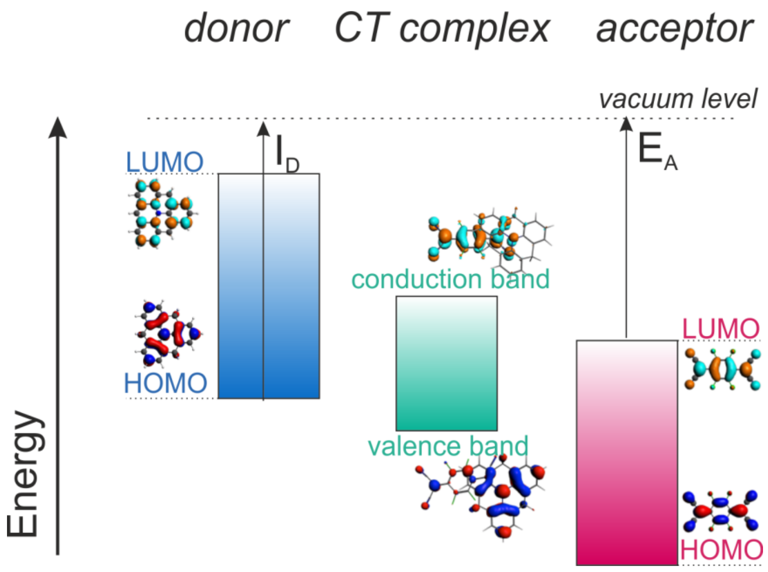

Figure 2.4. Schematic representation of the band structure of donor, acceptor and the possible way of new complex formation (adopted from [20] and [16]).

In the case of charge transfer compound formation as a thin molecular film, ultra-high vacuum (UHV) conditions are needed [21]. Inside the vacuum chamber the molecules are deposited usually by thermal evaporation on top of a suitable substrate. This method allows to produce molecular charge transfer films of defined thickness and also to investigate phenomena existing on the interface between different conducting layers. An important practical aspect of UHV-codeposition is that donor-acceptor combinations can be studied even without common solvent.

2.1.1. Fabre and Bechgaard salts

In contrast to the first synthesized conductor TTF-TCNQ discussed in the previous chapter, where the ratio of donor and acceptor molecules is 1:1, the Fabre and Bechgaard salts have a 2:1 ratio of donors and acceptors. The so-called Fabre salts have the class formula $(TMTTF)_2X$, where TMTTF is tetramethoxy-tetrathiafulvalene (see Fig. 2.2) and X is an anion. Analogously, $(TMTSF)_2X$, where TMTSF is tetramethoxy-tetraselenafulvalene are the class of Bechgaard compounds [3]. Fig. 2.5 shows one example of the Bechgaard family, $(TMTSF)_2PF_6$. Due to stoichiometry D_2A in these compounds, the band filling is commensurate with the underlying one-dimensional (1D) lattice.

Therefore, half of charge carriers (holes) per D molecule are involved in the charge transfer, meaning that one unit cell has 1/2 of hole and therefore the conduction band is quarter-filled. In these systems, strong Coulomb repulsion exists and this drives charge localization at high temperatures. Spin charge decoupling and localization influence the spin degrees of freedom and cause spin-Peierls or antiferromagnetic instabilities at low temperatures. The Fabre salts have charge localization, spin-charge decoupling and antiferromagnetic and spin-Peierls ground states. The Bechgaard salts show Fermi surface nesting driving the spin density wave ground state. Metallic and superconducting phases exist in these materials at high pressure due to suppression of the spin-density wave ground state [1], [22].

The structural arrangement of donor and acceptor stacks in Fabre and Bechgaard salts is represented as a zig-zag shape, where TMTTF or TMTSF donors are situated almost perpendicular to the *a* direction. Such a structure provides layer alternation of coupled and slightly dimerized donors and anions that fill the cavities between methyl groups of the donor molecules and therefore have spatial thermal mobility [23]. This mobility tolerates the presence of disorder in the anionic sub-system in the crystal.

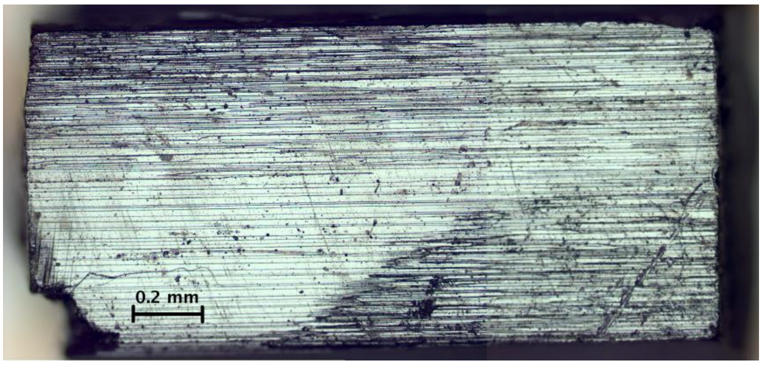

Figure 2.5. Photo of one example of the Bechgaard family – the surface of a $(TMTSF)_2PF_6$ single crystal.

The phase diagram shown in Fig. 2.6 illustrates all possible ground states and transitions in the class of Fabre and Bechgaard salts. One can see, that depending on the pressure (physical by compression the experiment or chemical by changing the size of anion) a change of the ground state from spin-Peierls (SP) through an antiferromagnetic (AF) insulator and spin density wave (SDW) phase to the superconductor (SC) could be observed. At higher temperatures, a charge ordering (CO) phase exists for the TMTTF class of materials.

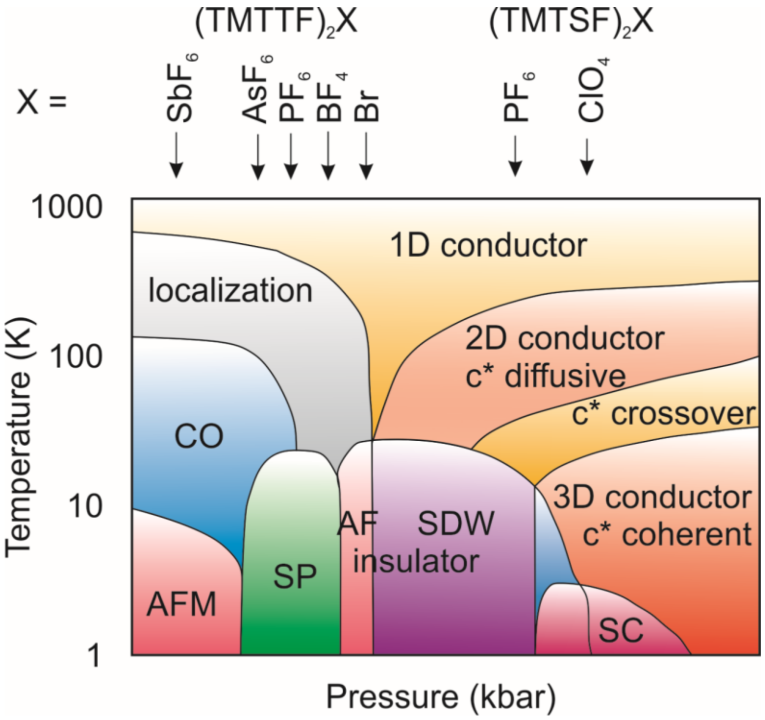

Figure 2.6. The phase diagram of the class of Fabre and Bechgaads salts (adopted from [9] and [24]). Here SP shows a spin-Peierls phase, AF means an antiferromagnetic insulator, SDW is a spin density wave phase, SC denotes a superconductor and CO is a charge ordering phase.

2.1.2. The (BEDT-TTF)-salts

The family of organic conductors based on BEDT-TTF (ET, in short) is very wide. The donor molecule ET is not completely planar due to the existence of two different configurations of ethylene groups in the structure (see Fig. 2.2). Organic conductors of this family have quasi-two-dimensional structure, although there are several examples where dimensionality is 1D [22]. Dimensionality in these compounds varies with the change of tilt and interaction strength between face-to-face and side-by-side arrangement of the BEDT-TTF molecules in the crystal. The layers of donors and anions are spatially separated, causing strong anisotropy of all characteristics in conductive plane and perpendicular to it [25].

2D charge transfer compounds have extensive polymorphism, meaning there is different molecular arrangement in the crystal packing and phases showing different transport properties even with the same chemical composition [8]. For example, a compound with donor molecule BEDT-TTF and anion ReO_4 is known in ratios D:A 2:1 and 3:2 and in morphologies α-, β- and γ- [26]. In case of the 2:1 ratio, meaning $(BEDT\text{-}TTF)_2X$ compounds, the HOMO of the $(BEDT\text{-}TTF)_2$ cation is tree-quarters-filled due to each neutral BEDT-TTF molecule which can accommodate two electrons in the HOMO. In accordance with the band theory, during dimerization of BEDT-TTF molecules, the conduction band is split, causing the HOMO to be half-filled, which, therefore allows the existence of the metallicity in BEDT-TTF based organic conductors [22]. However, when the system has strong electron-electron interaction (when the Coulomb energy becomes larger than the transfer energy), electrons become localized and the organic conductor exhibits the Mott-Hubbard insulating state [22].

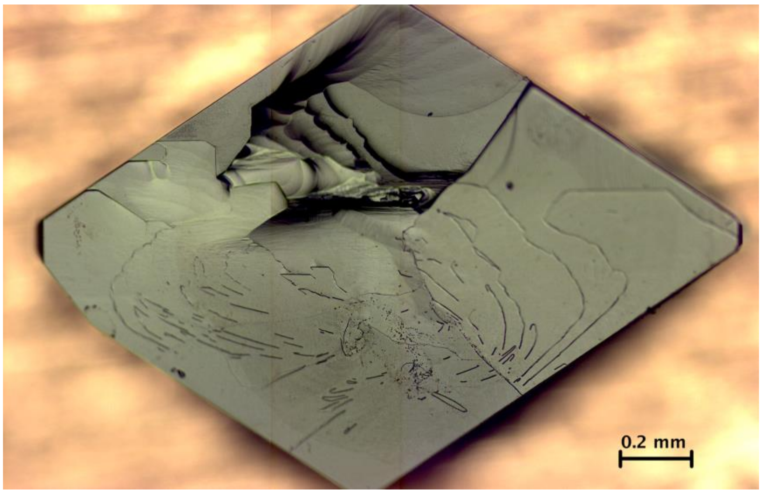

Figure 2.7. Photo of one example of the BEDT-TTF family – surface of a κ-$(BEDT\text{-}TTF)_2Cu[N(CN)_2]Br$ single crystal.

One of the most famous examples of this class is β-$(BEDT\text{-}TTF)_2I_3$, which was the first 2D superconductor at ambient pressure synthesized [27]. The same compound, but with α- stacking, is known to be metallic starting from room temperature down to 135 K where a metal-insulator transition occurs and it is accompanied by the formation of Wigner-crystal-like charge ordering that is driven by the electron-electron repulsion [4]. Currently the class of ET-based conductors has several hundred members.

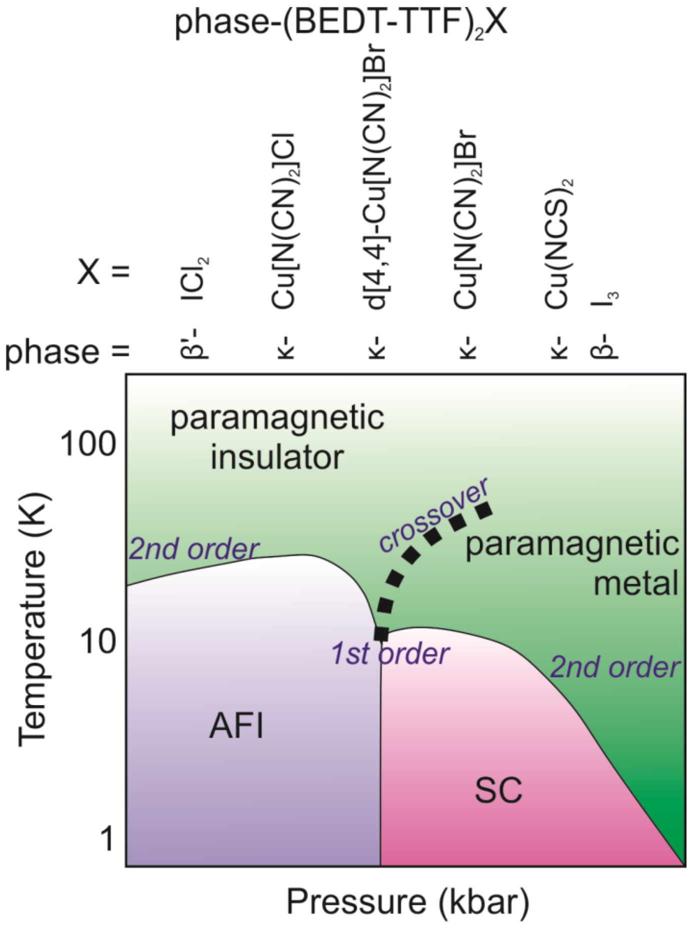

Figure 2.8. General phase diagram for the BEDT-TTF family of organic conductors (adopted from [28]).

The κ-phases of BEDT-TTF based compounds, in particular, κ-(BEDT-TTF)$_2$Cu[N(CN)$_2$]Br, or "κ-Br" in short (Fig. 2.7), are very exciting due to their relative position on the general phase diagram of the family and, therefore, draws interest from the fundamental point of view. In Fig. 2.8 it is shown, that the κ-Br compound, and especially its fully deuterated analog, is extremely close to the boundary between superconducting (SC) and antiferromagnetic insulator (AFI) ground states. The molecular structure of κ-phases is characterized by strong dimerization of the donor molecules in the crystal packing [25].

2.1.3. The (DOEO)-salts

In order to improve or change the electronic, transport, and magnetic characteristics of organic compounds in comparison to already existing ones, generally, one may change the structure of the donor or of the acceptor. The new molecule 1,4-(dioxandiil-2,3-dithio)ethylenedithiotetrathiafulvalene (DOEO) and the class of DOEO-based organic conductors is the result of the synthetic idea to increase the dimensionality of the donor. Thereby, chemical pressure is increased in comparison to the known structures by adding a dioxan ring to the existing BEDT-TTF donor molecule (compare Fig. 2.2 and Fig. 2.9 (a)). In this case the resulting donor structure has an additional fragment almost perpendicular to the ET-like skeleton of the molecule (Fig. 2.9 (b)).

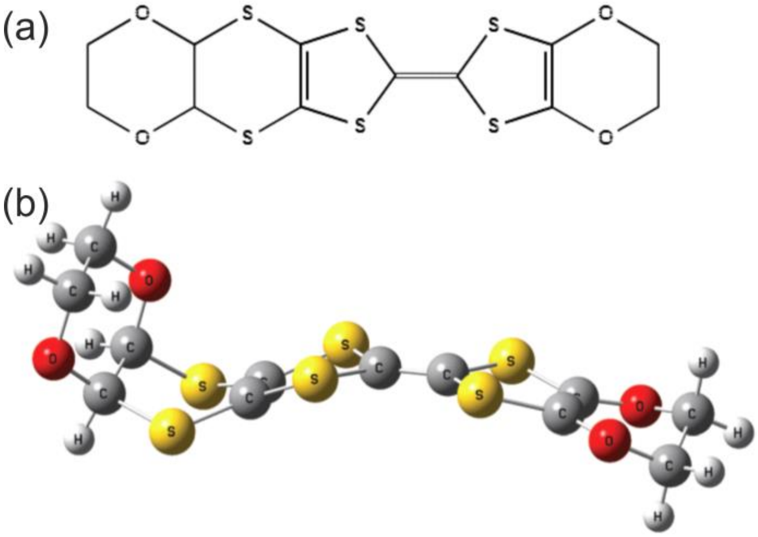

Figure 2.9. (a) Chemical structure of the DOEO molecule; (b) Spatial arrangement of atoms in the DOEO molecule.

The class of DOEO-based organic conductors is quite small. There are several reports about synthesis of stable metals, namely β-$(DOEO)_2BF_4$ [29], β-$(DOEO)_2PF_6$ [29], β''-$(DOEO)_2HSeO_4 \cdot H_2O$ [30], β''-$(DOEO)_2HSO_4 \cdot H_2O$ [31], β''-$(DOEO)_2NO_3 \cdot H_2O$ [31], as well as insulators β-$(DOEO)_2I_3$ [29], β-$(DOEO)_2ClO_4$ [29], β-$(DOEO)_2NO_3 \cdot H_2O$ [31] and also the compound β-$(DOEO)_4[HgBr_4] \cdot$TCE that has non-trivial transport temperature dependence with interplay of metallic and insulating transport properties [32]. Usually the $DOEO^{1/2+}$

radical cations[1] are weakly dimerized in a plane-to-plane or side-to-side manner. So, both of them could exist in parallel in one compound like in *β''*-$(DOEO)_2HSeO_4 \cdot H_2O$ [30]. Currently a generic phase diagram does not exist for this class of the organic compounds.

2.2. Physics of low-dimensional organic conductors

The structural particularities of low-dimensional charge transfer compounds influence the physical properties observed. Depending on the structural degrees of freedom and, therefore, instabilities in these salts, different ground states and phase transitions are observed.

2.2.1. Instabilities in low-dimensional systems

The major instability that exists for non-interacting fermions is associated with the Fermi surface nesting mechanism. This mechanism opens the gap, triggering the metal-insulator transition, or partial gap, causing a metal-semiconductor transition. Then the collective state appears that could be either a charge density wave (CDW), accompanied by a periodic lattice distortion (PLD), if a sizeable electron-phonon coupling is present, or a spin density wave (SDW) during presence of sizeable electron-electron repulsion [33]. There is also another scenario, when the Wigner lattice of localized charges ρ, accompanied usually by PLD, is stabilized by a strong Coulomb repulsion. The localization then could be either found on sites of the crystal lattice, and it is called, in this case, a charge ordering

---

[1] Formally, each molecule carriers half an elementary charge because the charge transfer is 1 electron per dimer.

(CO) state, or on the bond, being the Mott-dimer (MD). When the spin is also involved, the ground state could be antiferromagnetic (AF) or spin-Peierls (SP). The Fermi surface nesting mechanism triggers the previously mentioned instabilities mainly in 1D electronic systems. However, it could exist in a hidden form in both organic and inorganic compounds with higher dimensionality.

The $2k_F$ instability was first described by Peierls in 1955. In case of this instability, the 1D metal is unstable at low temperatures and establishes a PLD with new periodicity $(2k_F)^{-1}$ that perturbs the electronic states at $\pm k_F$ in the vicinity of the Fermi level E_F as it is shown in Fig. 2.10. Here ρ is the charge per repeat unit of the molecular chain. The PLD opens a gap in the band structure at the Fermi energy E_F. The PLD modulates also the electronic density and forms a CDW. The phase shift between PLD and CDW varies with the nature of the lattice modulation of the molecular conductor [33]. In case where in competition between inter- and intra-molecular components, the first one modulates the bond distances, a phase shift of $\pi/2$ is observed between CDW and PLD. Thus, the so-called bond order wave (BOW) appears. The PLD is usually detected in diffraction experiments by observing the satellite lines $\pm k_F$ in reciprocal space. Additionally, the CDW could be measured directly in a scanning microscope like it was done for the TTF-TCNQ salt in [34].

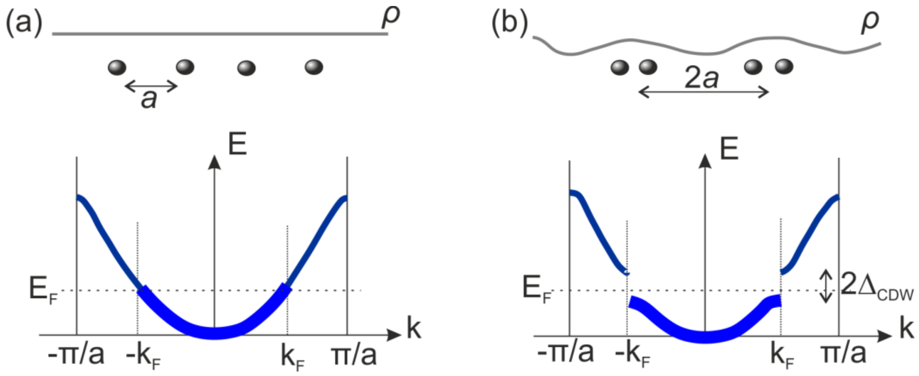

Figure 2.10. (a) Schematic representation of the conduction band in a metal. It is filled up to the Fermi level; (b) The same, but for an insulator, where a gap opens due to a modulation of the charge density.

Another type is the $4k_F$ instability, meaning the appearance of a modulated gap at twice the $2k_F$ wave vector. This instability is described as a precursor of the Peierls transition in the system of a spinless fermion gas [33]. In such systems the band of pseudo-fermions is filled within $\pm 2k_F$ due to the loss of the spin degree of freedom. Coulomb repulsion provides the foundation for spinless fermions in this case. Table 2-1 illustrates several examples of structural instabilities observed in organic low-dimensional conductors.

Table 2-1. Lattice instabilities revealed by X-ray diffuse scattering.

Compound	Instability	Where instability is located	References
TSF-TCNQ	$2k_F$	TSF stacks	[35]
HMTSF-TCNQ	$2k_F$	HMTSF stakes	[36]
TTF-TCNQ	$2k_F$	TCNQ	[37]
TTF-TCNQ	$4k_F$	TTF	[38]

2.2.2. Transport properties

Organic charge transfer compounds exhibit a wide range of transport properties from insulating to metallic and superconducting. Generally, the electric conductivity is described by the equation:

$$\sigma = ne\mu \tag{2.1}$$

where n is the charge carrier density (cm^{-3}), e is the charge of electron and μ is the carrier mobility ($cm^2V^{-1}s^{-1}$).

It is possible to control carrier density and mobility. For example, based on the band structure model for semiconductors and insulators,

$$n \propto exp\left(\frac{-\Delta_g}{2k_BT}\right) \tag{2.2}$$

where k_B is the Boltzmann constant, T is temperature and Δ_g is the energy gap.

For the organic molecular conductors or single organic components, where the electronic structure shows a closed shell, the energy gap could be described as:

$$\Delta_g = \Delta E - 2(t_1 + t_2) \tag{2.3}$$

where ΔE is the HOMO-LUMO gap, t_1 is the intermolecular (or inter-complex between DA pairs) transfer integral of the HOMOs and t_2 is the same for the LUMOs.

Therefore, it is illustrated, that by changing the values of $\Delta E, t_1$ and t_2 it is possible to tune the charge carrier density for organic compounds [15]. It is also possible to control the charge mobility. In the simplest example of 1D compounds, according to the tight binding approximation, μ could be represented as follows:

$$\mu = 2a^2 e\tau t cos(ka)/\hbar^2 \propto \tau t \tag{2.4}$$

where a is the interplanar distance, t is the transfer integral, τ is the relaxation time which depends on the scattering mechanism of the system. τ is inversely proportional to the product of density of states at the Fermi level $D(\Delta_g)$ and the square of the scattering potential V_s:

$$\tau \propto \frac{1}{D(\Delta_g)|V_s|^2} = \frac{2\pi t sin(ka)}{N|V_s|^2} \propto t \tag{2.5}$$

where N is the total number of electrons in the band [15].

Since $D(\Delta_g)$ is equal to $N/2\pi t sin(ka)$, the equation (2.5) is reasonable. Although many sources like phonons, molecular vibrations, impurities, Coulomb repulsion energy from the side, non-periodicity in the lattice, and others can contribute also to the relaxation time, τ could be proportional to the bandwidth $W = 4t$, where t is approximately proportional to the overlap integral S for 1D conductors [15]. From such considerations it becomes clear that during modeling and synthesis of novel organic compounds, it is possible to predict the transport properties from characteristics of pure donor and acceptor precursors.

Taking into account the simplified theory from [39], the boundary for ionicity in the charge transfer compound can be written as

$$I_D - E_A = M \tag{2.6}$$

where the donor’s ionization potential I_D and acceptor’s electron affinity E_A define the Madelung energy M in the crystal. In a real system, one should also consider additional effects and possible non-constant values for ionicity in dependence from M.

Depending on the relation between $I_D - E_A$ and M, organic conductors with a ratio of donor and acceptor molecules in the structure 1:1, meaning $D^{\rho+}A^{\rho-}$, could be classified into the following groups [40], [41]:

- Neutral insulators, where $I_D - E_A > M$ and charge is defined in region $0 \leq \rho \leq \rho_c$.
- Partially ionic conductors, where $I_D - E_A \approx M$. In this case the charge will be $\rho_c \leq \rho < 1$.
- Fully ionic insulators, where $I_D - E_A < M$. Here $\rho = 1$.

The threshold value of ρ_c decreases with increasing dimensionality of the system. Below the threshold value, the structure with alternating stacks is preferable rather than the segregated one, because then both the kinetic energy and the Madelung energy decrease with decreasing ρ, causing insulating properties [15].

2.2.3. Superconductivity

The metallic state is characterized generally by independently moving electrons in the bulk of the material. In contrast to this, in superconductors electrons form Cooper pairs. Then a magnetic field can destroy the superconductivity in the material by overcoming the pairing energy. Therefore, superconductors are characterized by critical field H_c and critical temperature T_c. The destroying magnetic field could be external, as well as internal. Even a small amount of paramagnetic impurities can suppress superconductivity [42], [43].

Superconductivity in 1D organic compounds is usually present at low temperatures (T_c is always below 2 K) and high pressure. The limit of critical temperature is independent on the anion symmetry. In a one-dimensional case, where the Fermi surface has also 1D character, fluctuations and anion disorder suppress superconductivity very efficiently [22], [44]. As a typical example of a 1D superconductor $(TMTTF)_2Br$ can be mentioned. In this case the superconductivity appears at T_c = 0.8 K under 25 kbar of external pressure [45]. Additionally, the cooling rate plays a role in stabilization of the superconducting phase. For instance, when a $(TMTSF)_2ClO_4$ crystal is cooled slower than 0.2 K/min, the SC could be observed at T_c = 1.2 K even at ambient pressure. However, when the cooling rate is faster, the sample becomes insulating at T_{MI} = 6.1 K due to frozen anion disorder [22], [46].

2D superconductors, having a 2D Fermi surface, provide indeed higher values of T_c. Among layered organic conductors the highest critical temperature observed at ambient pressure belongs to the κ-(BEDT-TTF)$_2$Cu[N(CN)$_2$]Br compound and has an onset at T_c = 11.6 K [47].

Superconductivity in all known materials could be classified into conventional and unconventional types. The conventional superconductivity was described by John Bardeen, Leon Cooper, and John Robert Schrieffer ("BCS") in 1957 [48]. The main idea of it is the consideration of the superconductivity phenomenon as a microscopic effect caused by a condensation of the Cooper pairs into a boson-like state [49]. Most of the known superconductors are of the conventional BCS class.

The unconventional superconductivity could not be explained by the BCS theory, it was found mainly in the high-temperature superconductors like Y-Ba-Cu-O [50], CeCu$_2$Si$_2$ [51], UBe$_{13}$ [52] and many others. The origin of high-temperature superconductivity is still under debates [53]. The most dominant opinion suggests electronic mechanisms (e.g. by antiferromagnetic correlations) instead of electron-phonon attraction mechanisms, as in BCS [54].

Experimental observations currently do not allow to define whether organic conductors belong to the conventional or an unconventional class of superconductivity[22],[55]. The confusion in this fundamental question appears because of the existence of the boundary between the superconducting and antiferromagnetic insulating phases (see Fig. 2.6 and 2.8). Additionally, it is possible to turn the ground state of one defined compound crossing the border. For example, the 1D compound (TMTSF)$_2$PF$_6$, having a SDW ground state at ambient pressure, becomes a superconductor at pressures above 50 kbar [56]. Analogously, the two-dimensional conductor κ-(BEDT-TTF)$_2$Cu[N(CN)$_2$]Cl is an antiferromagnetic insulator at ambient pressure and becomes a superconductor at T_c = 12.8 K under 0.3 kbar of external pressure [57].

2.3. Phase transitions in low-dimensional organic conductors

Phase diagrams of organic conductors, both one-dimensional and two-dimensional, are very rich due to instabilities determined by thermodynamics. The interplay between lattice, charge and spin degrees of freedom gives rise to different ground states in organic conductors. A defined ground state can be transformed in frames of a generic phase diagram, being suppressed by internal or external conditions. In this section the most important and frequent phase transitions, namely charge ordering (CO), Mott metal-insulator (MI), spin-Peierls (SP) and neutral-ionic (NI) transitions, will be described in depth.

2.3.1. Charge-ordering transition

A charge ordering transition is associated with charge disproportionation without significant structural change. However, tiny structural modifications were recently observed [58], [59]. It is considered that CO could be observed only in one-dimensional organic conductors (Fig. 2.6). In this scenario the CO is a realization of $4k_F$ instability. However, recently CO was also observed in two-dimensional compounds κ-(BEDT-TTF)$_2$Cu[N(CN)$_2$]Cl [10] and α-(BEDT-TTF)$_2$I$_3$ [60], where the transition has a ferroelectric character.

CO transition could be defined as a charge disproportionation into a well-defined superstructure. Electron-electron repulsion between charges is reduced due to strong long-range Coulomb repulsion V_{ij}. As a result, electrons take equidistant positions. To reduce the total electrostatic energy of the 1D organic system, localization of electrons on every $1/\rho$ site (meaning every ½ site for quarter-filled compounds) occurs. Such localization corresponds to the $4k_F = 1/\rho$ in chain reciprocal wave vector units [61]. Two different scenarios of localizations, stabilizing two ground states with different inversion symmetry, should be distinguished:

- Charge localization on bonds that stabilizes $4k_F$ BOW (bond ordering wave) or MD ground state;
- Charge localization on sites that stabilizes $4k_F$ CDW or CO ground state [3].

The extended Hubbard model [62] can describe the electronic side of charge ordering transition by extended Hubbard-Hamiltonian:

$$H = \sum_{i,j} t_{ij} c_{i\sigma}^{+} c_{j\sigma} + \sum_i U n_{i\uparrow} n_{i\downarrow} + \sum_{i,j} V_{ij} n_i n_j \tag{2.7}$$

where t is the hopping integral from site i to site j to describe the kinetic energy, $c_{i\sigma}^{+}$ is an operator creating an electron on site i with spin σ, $c_{j\sigma}$ is an annihilation operator, U denotes on-site Coulomb repulsion, V is the inter-site Coulomb repulsion defining the nearest neighbor interaction, and finally, n is the number operator for spins up and spins down.

Charge ordering requires stabilization of the convex repulsive potential V_{ij} [62]. Additionally, when finite U and t exist in the system, the system is metallic at $t > U$. For the quarter-filled systems the MI transition and CO ground state are predicted when long-range Coulomb repulsion is restricted to the first neighboring sites, meaning $|i - j| = 1$. When the second neighboring sites are taken into account, meaning $|i - j| = 2$, the new phase BOW or MD could be found [61].

2.3.2. Mott metal-insulator transition

In (BEDT-TTF)$_2$X and (TMTSF)$_2$X molecular conductors the conduction band is essentially quarter-filled. However, due to the tendency of donor molecules to dimerization, the effective conduction band becomes half-filled, and the interplay between kinetic energy and Coulomb repulsion becomes significant, causing the Mott transition between insulating and metallic states. In other words, it depends on the competition between localized and delocalized states of charge carriers. The metal-insulator transition belongs to the Mott type, when the low-temperature phase is predicted to be metallic, though experimentally it is insulating, like in case of the above mentioned materials [63]. From the phase diagram Fig. 2.8, it is visible that the compound of structure κ-(BEDT-TTF)$_2$Cu[N(CN)$_2$]Cl$_x$Br$_{1-x}$ is situated extremely close to the critical point and border near the Mott transition. Furthermore, superconductivity is enhanced near the Mott transition, making the investigation in this branch more attractive [2], [64], [65], [66].

When one considers an on-site Coulomb repulsion energy U and a bandwidth of upper-HOMO or lower LUMO W (depending on which band is split due to dimerization) and energy splitting ΔE_d, the dimer on-site Coulomb repulsion can be defined as

$$U_d = \Delta E_d + \frac{\left(U - \sqrt{U^2 + 4\Delta E_d^2}\right)}{2}. \tag{2.8}$$

Due to U >> ΔE_d, the equation (2.8) could be simplified as $U_d = \Delta E_d$. Therefore, the Mott criterion for the dimerized 2:1 or 1:2 salts could be formulated in the following way [15]:

$\Delta E_d > \mathrm{W}$ Mott insulator

$\Delta E_d < \mathrm{W}$ Metal

At critical values $\Delta E_d \approx W$, there is an instability and the system could turn from metal to insulator. For example, κ-(BEDT-TTF)$_2$Cu[N(CN)$_2$]Cl$_x$Br$_{1-x}$ compounds exhibit $W/\Delta E_d$≈1.1-1.2 showing strong electron correlation [15]. Due to the unstable metallic state, several ways of stabilizing the system were developed. To suppress the complete nesting of the Fermi surface, it is necessary to increase the dimensionality of the compound. Therefore, the strategy of chemical pressure / heavy atoms introduction into the system was applied and extended the class of low-dimensional organic conductors.

2.3.3. Peierls transition

According to the model, the Peierls transition occurs as an appearance of a new period in the structure at low temperatures due to decreasing electronic energy by coupling spins and, therefore, opening a gap at the Fermi energy (see Fig. 2.10). The transition is possible when the energy gain due to shifted spins is larger than the necessary elastic energy to get them shifted [67]. It is necessary to consider a 1D structure for the possible existence of a Peierls transition. When the dimensionality is larger, the Fermi surface has a certain curvature, however, the Brillouin surface discontinuity should be flat. Therefore, it is impossible to turn a 3D metal into an insulator using the Peierls model.

Spin-Peierls transitions could be easily detected using X-ray or neutron scattering by the appearance of super-lattice reflections of weak intensity at (1/2, 1/2, 1/2c*) below certain temperatures [3]. Additionally, it could be possible to directly see the reconstruction of the surface in STM [34].

2.3.4. Neutral-ionic transition

Along with the phase transitions discussed above, one more transition should be addressed. The neutral-ionic transition is a collective phenomenon that exists in one-dimensional organic charge transfer complexes where donors and acceptors are arranged in mixed stacks: …DADADADADA… [68]. At normal conditions these materials are found to be either ionic (with charge per molecule $\rho \approx 1$) or neutral ($\rho \approx 0$). But during a change of external conditions (temperature, pressure), certain neutral compounds become ionic [69]. The equation of charge redistribution could be written in the following form:

$$D^{\rho+}A^{\rho-} \leftrightarrow D^{+}A^{-} \qquad (2.9)$$

In an ideal case, the charge redistribution is decoupled from the lattice and does not change intermolecular distances. However, sometimes the interplay between the average ionicity and dimerization of the stack is observed (see Fig. 2.11). The most common example of a temperature-induced NI transition with discontinuous jump of ρ is the first-order transition in TTF-CA (where CA is tetrachloro-*p*-benzoquinone, see Fig. 2.2) at T_{NI} = 81 K [68].

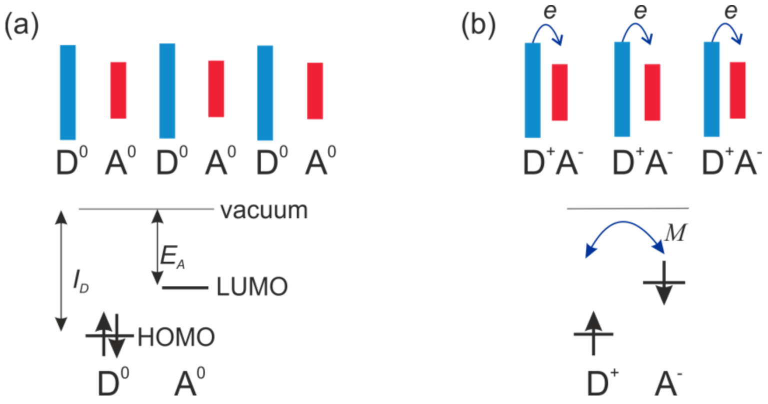

Figure 2.11. Schematic representation of the (a) neutral "band" insulator phase and (b) ionic "Mott" insulator spin-Peierls phase (adopted from [70]). I_D denotes the ionization potential, E_A is the electron affinity, M is the Madelung energy.

A NI transition could be detected as a transition from a band insulator to a Mott insulator caused by competition between Coulomb repulsion and difference in donor-acceptor sites [68].

3. Experimental and theoretical methods

In this chapter the experimental and theoretical techniques used for the present study are presented and discussed. First, SQUID magnetometry and ESR spectroscopy are described. Then a comparable analysis of different photoemission methods like UPS, XPS, HAXPES, as well as a discussion on the requirements is performed. At the end, NEXAFS and Infrared Spectroscopies are introduced. The overview of techniques consists of a broad introduction for each method and details of the experiments discussed in the present work. Last, some introduction on the theoretical approaches used is performed.

3.1. SQUID magnetometry

SQUID (superconducting quantum inference device) is the main type of instruments that are sensitive and precise enough to investigate the magnetic properties of organic conductors (Fig. 3.1). The principal working idea of SQUID is based on the quantization of the magnetic field in the superconducting detector with Josephson contacts [71], [72]. The resulting signal oscillates with quantized magnetic units $\Phi_0 = 2\pi\hbar/2e \approx 2.0678 \cdot 10^{-15}$ T·m^2, where $\hbar$ is Planck's constant and e is the electron charge due to interference of superconducting currents with a change of magnetic field through the SQUID sensor. The quantization of the signal flux originates from the fact that the macroscopic wave function

$$\Psi(\vec{r},t) = |\Psi(\vec{r},t)| exp[i\varphi(\vec{r},t)] \tag{3.1}$$

must be integer valued when it goes around the superconducting detector [71]. When no field/current is applied to the system, the phase $\varphi(\vec{r},t)$ has the value $2e$, that is constant for all Cooper pairs. When a field is applied, the phase around the loop-like detector changes by $2\pi n$, where n is the number of the enclosed flux quanta [73].

SQUID magnetometry allows to obtain such magnetic characteristics as coercivity, magnetic susceptibility, magnetic moment, Curie temperature, and to estimate the average spin value.

Figure 3.1. The experimental setup of SQUID magnetometer used in the present research.

In the present work, the magnetic characteristics of organic conductors were investigated using MPMS 5XL type SQUID magnetometers (Quantum Design) in the Institut für Anorganische Chemie (Mainz, Germany) and the Institute of Problems of Chemical Physics (Chernogolovka, Russian Academy of Science). For a calibration a pure palladium wire was used, which has a magnetic susceptibility of $5.3 \cdot 10^{-6}$ cm^3/g at 293.1 K. The cryostat of the SQUID magnetometer allows the instrument to cool down to 1.8 K and control the sample temperature with an error bar of less than 10^{-2} K. Present experiments were performed in the DC (direct current) mode. The diamagnetic contribution of the sample holder at room temperature was negligible in comparison to the true signal. The magnetic moments at each temperature $M(T)$ were referenced to the *dc* molar magnetic susceptibility $\chi = M/\nu H$, where H is the magnetic field and ν is the amount of material in mol.

3.2. Electron spin resonance

Electron spin resonance (ESR) or electron paramagnetic resonance (EPR) is a very powerful technique for the material characterization where unpaired spins are present. The ESR spectroscopy can indicate the localization of charge carriers via characteristic changes in the spectrum, in particular spectral shape and symmetry. It provides information on the surroundings of the localized paramagnetic centers. ESR is based on a selective absorption of microwave radiation with a certain frequency due to Zeeman splitting of unpaired spins in an applied magnetic field (Fig. 3.2) [74], [75]. ESR was not measured in the present Thesis, however our earlier study on $(DOEO)_4[HgBr_4]$ TCE crystals [76] is discussed in detail in Chapter 4.

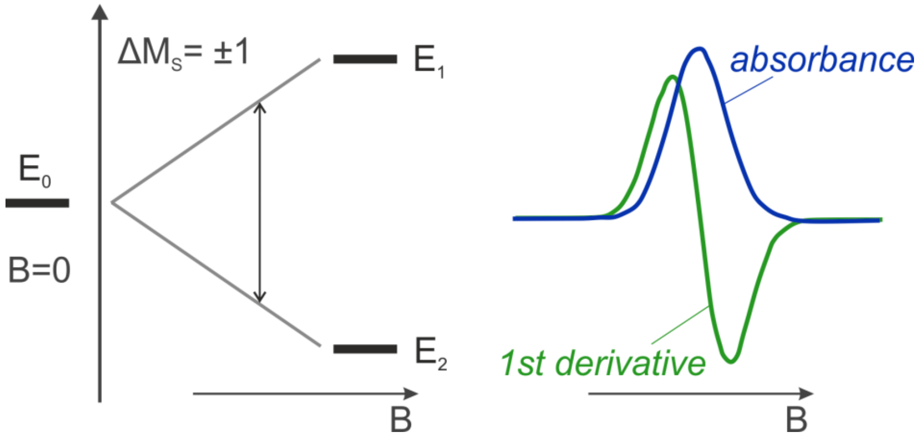

Figure 3.2. Schematic energy level diagram for an insulated electron ($S = 1/2$) in an applied magnetic field B (left panel) as well as the corresponding absorption spectrum and the first derivative ESR spectrum [74], [75], [77].

When talking about a free electron, its spin is $S = 1/2$. In presence of a magnetic field, the magnetic quantum number is introduced: $M_S = +1/2$ or $M_S = -1/2$ (the corresponding energy levels E_1 and E_2 are denoted in Fig. 3.2). The most important consequence of the electron spin is the associated magnetic moment μ_e that is proportional to the spin angular momentum [74], [75]:

$$\mu_e = -g_e \mu_B S \tag{3.2}$$

where μ_B is the Bohr magneton, g_e is the electron g-factor, which is 2.0023 for a free electron.

If the unpaired electron is placed into a magnetic field, the spin will be represented as discrete states, due to the spin multiplicity rule. In this case one would observe a Zeeman splitting as a result of interaction between spin and applied magnetic field. In classical terms, it could be described as:

$$E = -\mu \boldsymbol{B} \tag{3.3}$$

For a quantum mechanical system one must replace μ by the corresponding operator, giving the following simple spin Hamiltonian for a free electron in a magnetic field **[74]**, [75], [77]:

$$H = g_e \mu_B S \boldsymbol{B} \tag{3.4}$$

To simplify, one can define the field along the z direction, then the scalar product will be:

$$H = g_e \mu_B S_z \boldsymbol{B} \tag{3.5}$$

The S_z value here can be replaced by M_S, giving

$$E = g_e \mu_B M_S \boldsymbol{B} \tag{3.6}$$

Since $M_S = \pm 1/2$ only two energy states are available, which are degenerate in the absence of a magnetic field, but as B increases this degeneracy is lifted linearly [77] as illustrated in Figure 3.2. The separation of the two levels can be matched to a quantum of radiation through the Bohr frequency condition:

$$\Delta E = hv = E_1 - E_2 = g \mu_B B \tag{3.7}$$

The existence of two Zeeman levels, and the possibility of inducing transitions from the lower energy level to the higher one is the very basis of EPR spectroscopy [74], [75], [77].

In case of more complicated systems with interactions between electrons and nucleus, additional lines in the ESR spectrum are observed.

3.3. Photoelectron spectroscopy

Photoelectron spectroscopy (PES) is a widely used technique for determining the electronic structure of materials. The common PES experiment configuration is illustrated schematically in Fig. 3.3. Being in ultra-high vacuum (UHV) conditions, a sample is irradiated by the monochromatized light with photon energy $h\nu$ that could be obtained from a simple laboratory source or a synchrotron radiation facility. Photoelectrons escaping the sample due to the photoelectric effect are then discriminated by their energy and detected by an energy analyzer. Depending on the excitation source, ultraviolet photoelectron spectroscopy (UPS), X-ray photoelectron spectroscopy (XPS), or hard X-ray photoelectron spectroscopy (HAXPES) could be used. If the photoelectrons are investigated not only with respect to the kinetic energy but also to the emission angle, angular-resolved photoemission (ARPES) ca be recorded.

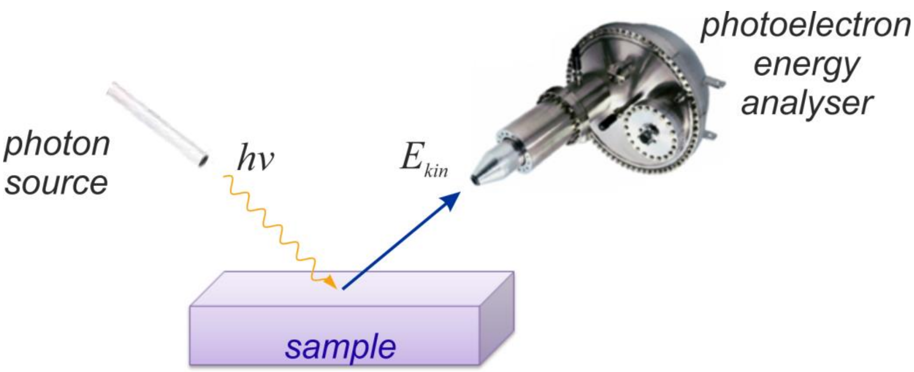

Figure 3.3. Schematic representation of a PES experiment. The investigated material is irradiated by the photon beam with excitation energy $h\nu$ and the escaping photoelectrons are detected by an energy analyzer.

A schematic illustration of the PES principle is shown in Fig. 3.4. This diagram corresponds to UPS from a gold sample, where E_F is the highest occupied level that is separated by the work function Φ_s of the material from the vacuum level E_{vac}. Below E_F, depending on the binding energy E_B, the valence states are distributed. When the radiation is absorbed by the sample, the photoelectrons are lifted above the vacuum level. In the simplest way such a PES experiment could be described with the following equation:

$$E_{kin} = h\nu - \Phi_s - |E_B| \tag{3.8}$$

where E_{kin} is the kinetic energy of the emitted electron, E_B is the binding energy, $h\nu$ is the excitation energy and Φ_s is the work function of the sample [78], [79].

In a more complex manner, more relevant to experimental work, this energy conservation equation could be presented in the following form:

$$h\nu = E_B^{vac} + E_{kin}^{i} + V_{charge} + V_{bias} = E_B^{F} + \Phi_{spectr} + E_{kin}^{f} + V_{charge} + V_{bias} \tag{3.9}$$

where E_B^{vac} is the binding energy of the electron relative to the vacuum level, E_{kin}^{i} is the kinetic energy of the emitted electron when it leaves the sample surface, E_{kin}^{f} is the kinetic energy of the emitted electron as it is measured by the spectrometer, E_B^{F} is the binding energy of the electron relative to the Fermi level, Φ_{spectr} is the spectrometer work function, V_{charge} is the charging potential on the sample due to a possible not fully compensated current of emitted electron and secondary electrons, and V_{bias} is the bias potential between sample and spectrometer, which commonly is scanned [80].

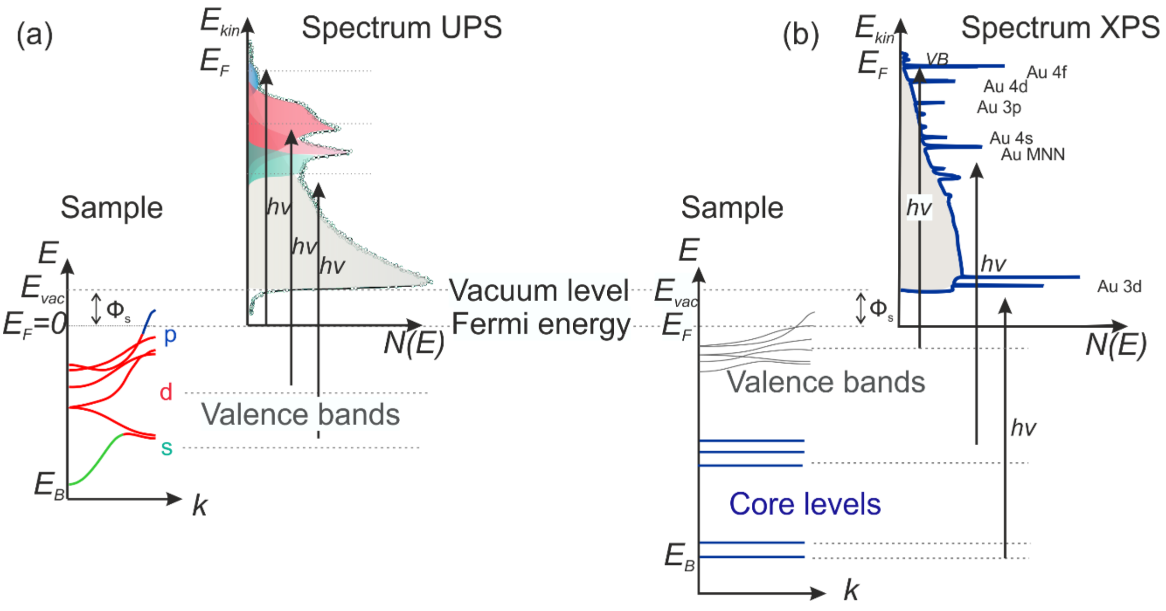

Figure 3.4. Schematic representation of the photoemission process of ultraviolet photoemission spectroscopy (a) and X-ray photoemission spectroscopy (b) and relation between energy bands and core levels in a gold sample and the corresponding experimental photoemission spectrum taken for a fresh Au film.

Charging as discussed in equation (3.9) often occurs during measurements on insulating materials. Therefore, it also can occur when investigating organic samples.

Depending on the excitation energy and photon flux, the estimated amount of charging is different. In UPS the excitation photon energy is 21.2 eV, thus, only the valence bands contribute to photoemission and the charging effect can be restricted to the surface due to the small UPS probing depth. In XPS a typical excitation energy used is 1254 eV – then many core levels can contribute to the signal and significant surface charging can occur which penetrates into several layers. The inhomogeneous charge distribution in the beam spot normally broadens the XPS signals and shifts the whole spectrum to lower kinetic energies. In XPS, the charging effect is observed within about 1 nm from the surface. However, in HAXPES a typical excitation energy used is 6 keV and the large mean free path of several nm can lead to inhomogeneous, layer-wise charging as discussed in [12]. The present results (in the forthcoming sections) indeed show charging contributions both in the XPS and HAXPES spectra that could not be avoided. The measurements were reproduced on several samples from different batches and spectra were taken both down to and warming up from low temperatures. The trend for all samples was the same. An effective way to check for the charging is to reduce the photon intensity, which leads to a lower charging level, since the emitted current is reduced.

For the HAXPES data evaluation procedure, the Unifit 2013 software was always used. This program allows fitting of the spectra at different temperatures with constant parameters while changing only the energy position of the signal. This gives valid values of energy redistribution between partial spectra. Therefore, the HAXPES intensity data could be analyzed even from a charging sample as long as there are no temporal shifts during the measurement.

On the one hand, charging is a complication that may even hide the true energy shifts, but on the other hand, it can also be an indicator of phase transitions. Due to the different transport properties of all existing phases in a compound, the degree of charging and the shift value correspondingly is different and therefore it is possible to detect the temperature of the transition by analysis of the shift value. In particular, layer-wise charging provides access to changes in the interlayer conductivity as it will be discussed in the Chapter 4.

3.3.1. Inelastic mean free path

Due to the fact that equations (3.8) and (3.9) include the work function of the sample or of the spectrometer, it is necessary to keep the work functions independent on the measurement time. Since for a freshly prepared sample surface the work function could be easily affected by contaminations, UHV conditions (base pressure $p < 10^{-9}$ mbar) are required.

Additionally, the probing depth of the photoemission process in solids is important for the relative contribution of the surface. The probing depth depends mainly on the inelastic mean free path (IMFP) of the photoelectrons (Fig. 3.5) and elastic electron scattering as well as the formation of secondary electrons, forming the background of photoemission spectra (gray areas in both spectra in Fig. 3.4). The calculated points for the IMFP suggest the quantitative and qualitative values for probing depth, and thus the surface sensitivity for different photoemission methods.

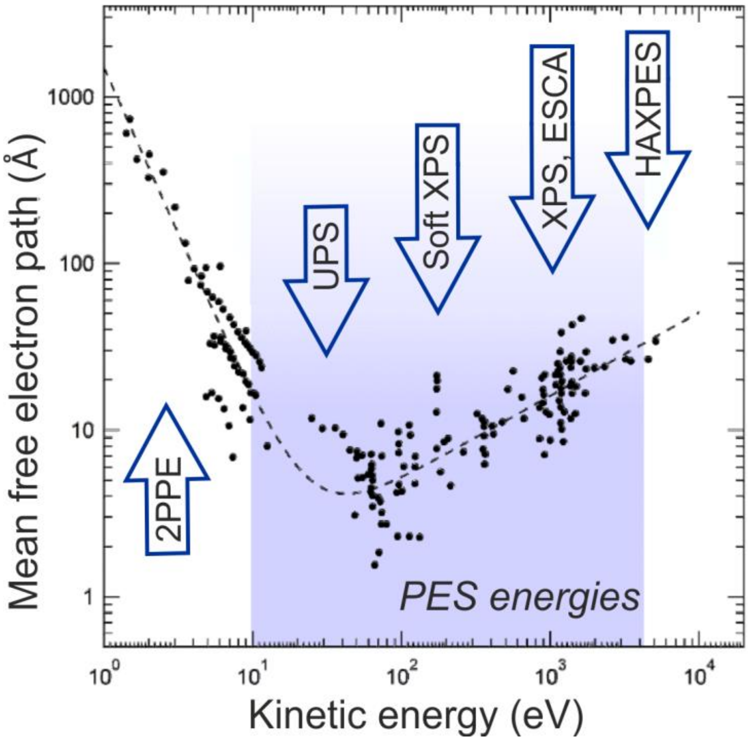

Figure 3.4. Inelastic mean free electron path calculated for 41 elements plotted as a function of kinetic energy. Here the kinetic energy refers to the Fermi level (adopted from [81]).

Following this comparison, it is always necessary to prepare the investigated surface properly before the experiment. The only exception is HAXPES, thus this is favorable to study organic samples that cannot be cleaned in UHV. Moreover, different PES techniques with various excitation energies complement each other and therefore allow to explore the information from both surface and bulk and to discuss the effects due to the chemical compositional difference between them.

3.3.2. Ultraviolet photoelectron spectroscopy

The UPS method implies an excitation source providing photons with $h\nu$ = 21.22 eV in case of He I or 40.81 eV in case of He II radiation when a helium discharge lamp is used. It is also possible to use other rare gases like neon, for example.

The photoelectron spectrum contains a series of signals each corresponding to one valence-region molecular orbital energy level (see Fig. 3.4). A useful quantity for the characterization of solids (in particular donor-acceptor complexes) by UPS is the determination of the work function of the material. The change of the work function is a very important criterion for the fabrication of mixed donor-acceptor thin molecular films in UHV conditions. The low-energy cut-off of the UPS or XPS spectrum establishes the kinetic energy zero, and $h\nu$ is the distance between the initial state (core level or valence band) and the final state, visible in the spectrum (see Fig. 3.4 (b)). The high-energy cut-off visible for metals is caused by the excitation from occupied bands near the Fermi level of the sample. The difference between the cut-off positions, i.e. the width of the spectrum, ΔE can easily be extracted from the spectrum. In practice the sample work function is determined by the equation

$$\Phi_s = h\nu - \Delta E \tag{3.10}$$

A more complicated situation occurs with a semiconducting or insulating sample, where the initial states near the Fermi level and the high-energy cut-off is invisible due to vanishing density of states. In this case, the reference of a clean metal surface (Au in the present work) is used under the same experimental conditions and being in contact with the investigated sample. Identical biasing is required in this case [79].

3.3.3. X-ray photoelectron spectroscopy

The XPS technique uses higher excitation energies in comparison to UPS. Mg*K*α (1253.6 eV) or Al*K*α (1486.6 eV) X-ray anodes are usual lab sources. X-rays are emitted when the electrons from upper levels (*L, M*) of Mg or Al fill up vacancies in the lower levels (*K*). This occurs when the high voltage at the anode of the X-ray tube accelerates an electron from the cathode (thermal emitter) that then collides with the anode material (Mg or Al) and brings enough energy to excite the electrons from its *K*-shell. Monochromatized synchrotron radiation is also widely used as a tunable source in the soft (ca. 300 – 1000 eV) and tender X-ray range (ca. 1000 – 3000 eV).

XPS is very sensitive to the chemical composition and environment of the elements in a material in a probing depth which is typically about 1 nm. In XPS spectra, each element gives rise to a characteristic, well-known set of peaks in the photoelectron spectrum at kinetic energies determined by the photon energy and the respective binding energies. The presence of peaks at particular energies therefore indicates the presence of a specific element in the sample under study. Furthermore, the intensity of the peaks is related to the concentration of the element within the analyzed region. Thus, the technique provides a non-destructive quantitative analysis of the surface composition. Arising from the fact that the transfer of charge from the valence orbitals, typically involved in chemical bonding, is reflected in the measured binding energies of the core levels of the atoms, it is possible to distinguish the signals originating from atoms in different chemical environments. Data for elements and numerous compounds are tabulated.

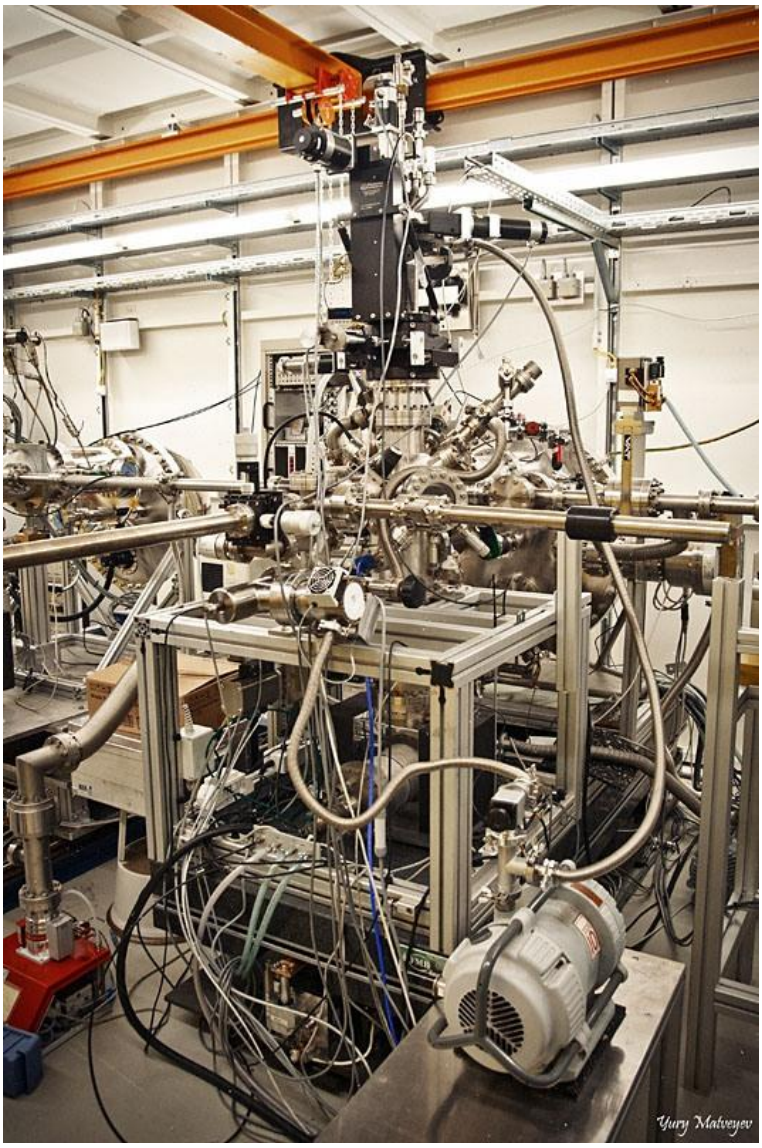

Figure 3.6. Photo of the experimental HAXPES setup at Petra III, DESY (Hamburg), used for the present studies. Photo courtesy Yury Matveyev.

3.3.4. Hard X-ray photoelectron spectroscopy

The hard X-ray variant of XPS (HAXPES) provides the same information but for a substantially larger probing depth of 8-10 nm. HAXPES thus makes it possible to investigate the electronic structure in the bulk of the material. Furthermore, the comparison of bulk and surface photoelectron spectra gives information on the surface termination. A combined study using soft and hard X-ray photons on the same sample allows us to discuss the electronic structure taking into account different structural aspects at the surface. This technique was applied to the organic conductor $(DOEO)_4[HgBr_4]\cdot TCE$.

The HAXPES measurements were carried out at the P09 HAXPES end station of PETRA III (Hamburg) at a photon energy of 6000.5 eV (Fig. 3.6) [82], [83]. For maximum sensitivity and minimum radiation damage, the energy analyzer (type SPECS Phoibos 225 HV) was combined with a delay-line detector (type Surface Concept). For the present measurements the overall energy resolution (electrons and photons) was 440 meV. The beam was focused down to a 0.2 mm × 0.4 mm spot size. The spectra were recorded in normal emission geometry at nearly grazing photon incidence (≈ 2°).

3.4. Near-edge X-ray absorption fine structure spectroscopy

Near-edge X-ray absorption fine structure (NEXAFS) spectroscopy probes absorption of synchrotron radiation by excitation of core electrons into unoccupied electronic states above the Fermi level and further filling of the core hole by the emission of a fluorescent photon or by an Auger process [84], [85], as it is shown schematically in Fig. 3.7. Then both processes could be detected and evaluated using a fluorescence detector and energy analyzer, respectively. However, much more intensity could be expected for the Auger electron yield in comparison to fluorescence yield for edges of atoms with low atomic numbers.

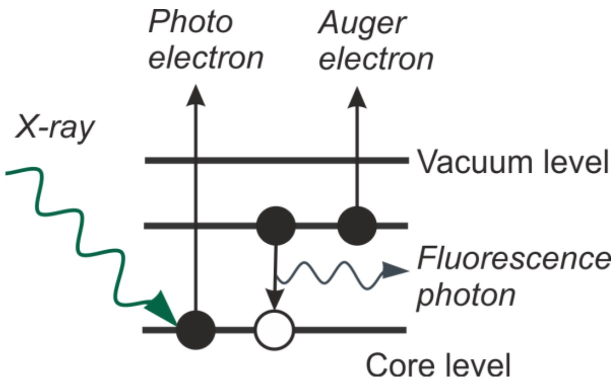

Figure 3.7. Schematic energy diagram of the NEXAFS process as a sequence of photo absorption process, filling of the core hole connected with emission of a fluorescence photon or an Auger electron (adopted from [85]).

The effective penetration depth, where one can get NEXAFS information from, is usually around 5 nm for metals and slightly more for insulators. Synchrotron radiation, with energies typically between 200 and 800 eV, penetrates material several microns deep and generates electrons in the bulk. Then a cascade of electrons appears due to inelastic scattering processes. But in order to escape the material surface, electrons should have enough energy to overcome the work function of the investigating material. Therefore, the effective mean free path and hence the probing depth is much smaller than it could be expected from the X-ray penetration depth. The surface barrier acts as high-pass filter and the long-travelling slow electrons from the cascade cannot escape.

The nature of NEXAFS is illustrated schematically in Fig. 3.8. In the resonant excitation, a transition from the initial state to an unoccupied molecular orbital around the ionization threshold occurs and has a step-like or peak shape. Depending on the orbital symmetry, unoccupied states of π^* and σ^* types exist and they show up separately in energy lines in the NEXAFS spectrum. The π^* electronic state is often located below the ionization potential because of electron-hole Coulomb interaction [85].

This method is very powerful and was used in numerous studies, mainly to investigate the electronic structure and the unoccupied density of electronic states and its development during formation of a compound or crossing a phase transition temperature [86]. Furthermore, NEXAFS could be used for investigation of the molecular orientation in bulk crystals by a change in angular dependence of absorption spectra [87]. In this case, the polarization of synchrotron radiation will cause different intensities depending on the spatial arrangement of molecular orbitals. Additionally, when a new charge transfer compound is formed, the NEXAFS spectra will look differently in comparison to pure donor and acceptor, making it possible to use this method as a test for the novel compounds formation [88], [89].

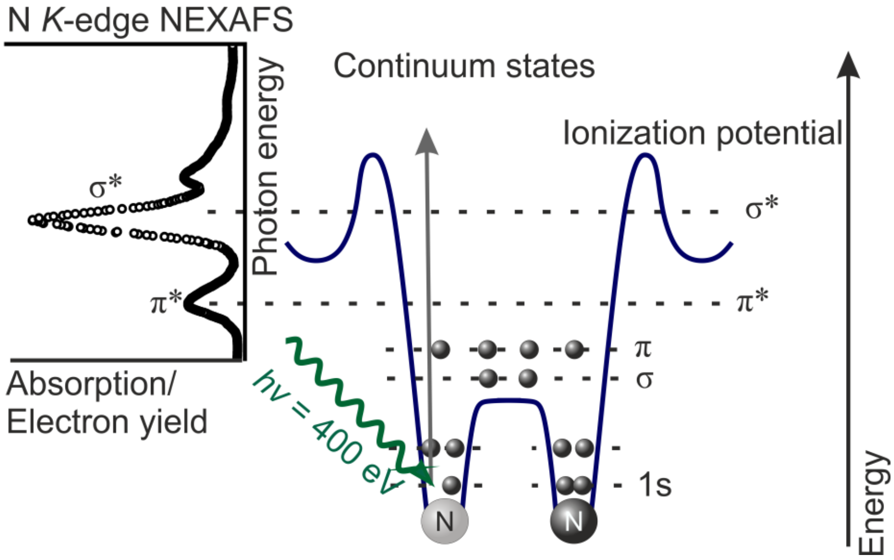

Figure 3.8. Transition scheme for nitrogen *K*-edge NEXAFS (right) and resulting spectrum for TCNQ powder measured at ANKA, Karlsruhe (left).

For the NEXAFS measurements soft X-rays from the WERA beamline at ANKA, Karlsruhe (Germany), at an energy resolution of 150 meV and I1011 beamline at MAX II, Lund (Sweden), at an energy resolution down to 28 meV were used. The information depth is usually about 5 nm in such experiments. This probing depth corresponds to approximately 15 molecular layers, which is sufficient for yielding information on the bulk of the crystallites. The use of this technique allows for the measurement of macroscopic crystals, powders and thin molecular films that have been transported through air without additional preparation or cleaving.

Several important considerations should be taken into account during analysis of the NEXAFS data. All are caused by the fundamental principles of the experimental technique and will be mentioned briefly below.

Measured NEXAFS signals from the sample depend on the intensity of the incident X-rays, therefore the raw spectra should be normalized to the intensity of the photon beam [84]. In the present work the correction approach was used where the raw signal from the sample was always divided by the electron yield signal from a fresh gold grid monitor (placed in the synchrotron beam) as a reference measured in parallel with the sample [90]. For that reason, the freshly coated gold grid was prepared in advance before every measurement series and the detection technique for the sample and the grid was used identical. As a result, the artifacts due to variations of the ring current or synchrotron ring instabilities are completely excluded from the analyzed NEXAFS spectra of the sample.

Prior the analysis of the partial spectra of the NEXAFS signal, the step-like features referred to as continuum steps should be taken into account. Such steps are the results of the excitation of the core electron to a continuum of final states [84]. Step-like features in the near-edge spectrum exist in both gas phase and solid materials. The lowest unoccupied states in solid insulators, for example, are situated above the band gap; when the transition to the conduction band minimum occurs, a continuum step will appear in the spectrum [91]. In more complicated examples, like molecules on surfaces or donor-acceptor pairs, the step-like feature could be a signature of the transition to the metallic states above the Fermi level. Figure 3.9 shows a fluorine near-edge spectrum of the charge transfer compound DTBDT-F_4TCNQ where the continuum step is situated around $h\nu = 686.5$ eV (see arrow). The step could be different for changed conditions of the experiment, however, for measurements of the angular dependence of the NEXAFS signal at a certain temperature it can be assumed to be constant [84].

The quantitate analysis of the peaks and steps of the spectra based on deconvolution is a common way to discuss the structure of the unoccupied electronic states in the studied material [84], [88], [92], [93]. Depending on the conditions of the experiment, the following types of the line shapes could be discussed:

(i) Lorentzian shape of the spectral line is usually present in the case when the instrumental resolution is negligibly small in comparison to the intrinsic life-time related peak width;

(ii) Gaussian line is usually observed in experiments where the instrumental resolution (mainly monochromator resolution) is large and dominates the line width;

(iii) Voigt line is the profile represented by the convolution of a Lorentzian and a Gaussian.

In the present work the software package Unifit2013 was used to determine the step-like base like and perform the deconvolution of the NEXAFS spectra to partial spectral lines.

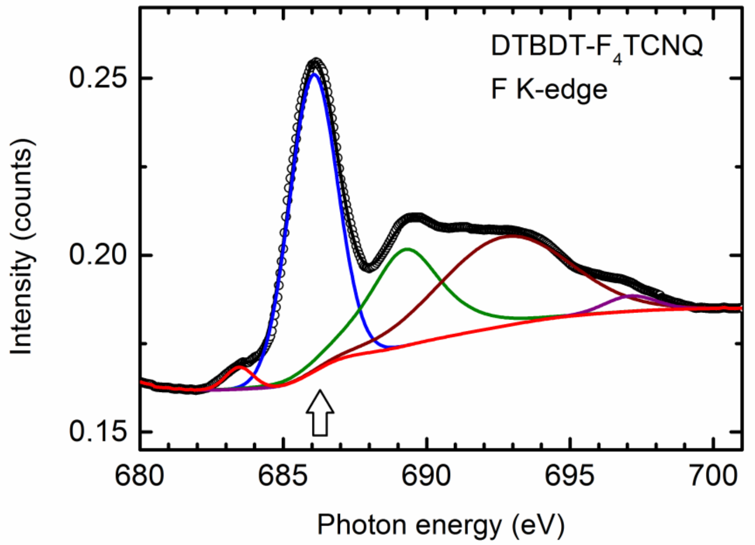

Figure 3.9. Fluorine K-edge NEXAFS spectrum of the charge transfer crystals DTBDT-F_4TCNQ measured at room temperature. Circles denote experimental data; thin curves show partial spectra as obtained from the multipeak fit routine. The background is shown as a step-function (the step is denoted by the arrow).

The comparison of experimental spectra with theoretically predicted orbital positions makes it possible to align measured partial spectra to calculated unoccupied electron orbitals of the LUMO (lowest unoccupied molecular orbital) and possibly higher-lying ones and discuss their spectral weight change with varying temperature. Currently the classical approach of a theoretical treatment of molecular conductors investigated by NEXAFS is sudden state approximation [87], [88], [94] which assumes that the time of the interaction of the X-ray photon with the electronic subsystem is much shorter than the typical time scale for spatial rearrangement of the electronic density. However, the present work reveals that the consideration of the final state effects beyond the ground state approximation play an important role and cannot be neglected as in the classical way of analysis. The new approach considers the screening effects of the core-hole Coulomb correlation and therefore it assumes that the life time of the excitation is longer than the electronic time scale. More examples and discussion on that are represented in the experimental Chapters 5 and 6.

3.5. Infrared spectroscopy

Infrared spectroscopy (IR) is a very convenient technique for the estimation of the amount of charge transfer in novel organic conductors [89]. Usually the C≡N stretching modes are analyzed and the frequency shift of a characteristic line can be used directly to determine the charge transfer amount that is transferred from the acceptor to the donor molecule using simple equations from [95].

An IR spectrum typically represents absorption of infrared radiation by the material during exposure (Fig. 3.10). If the dipole moment of the molecule changes during the absorption process, the IR spectrum will have molecular vibration lines of certain intensity [96], [97]. The energy positions of IR lines in the spectrum correspond to characteristic molecular vibration frequencies. From these lines it is possible to gain information on functional groups in the compound. The energy is quantized; therefore, an IR spectrum is usually represented as consisting of sharp well-resolved lines.

Mainly molecular vibrations of stretching (change of length) and bending type (change of angle) are involved in the IR absorption process.

In the present work infrared spectroscopy was measured on polycrystalline samples. Spectra were obtained using a Nicolet 730 FT-IR spectrometer between 4000 and 500 cm^{-1} at room temperature. Resolution of the measurements was better than 1 cm^{-1}. The spectrometer was kindly provided by Max-Planck Institute for Polymer Research.

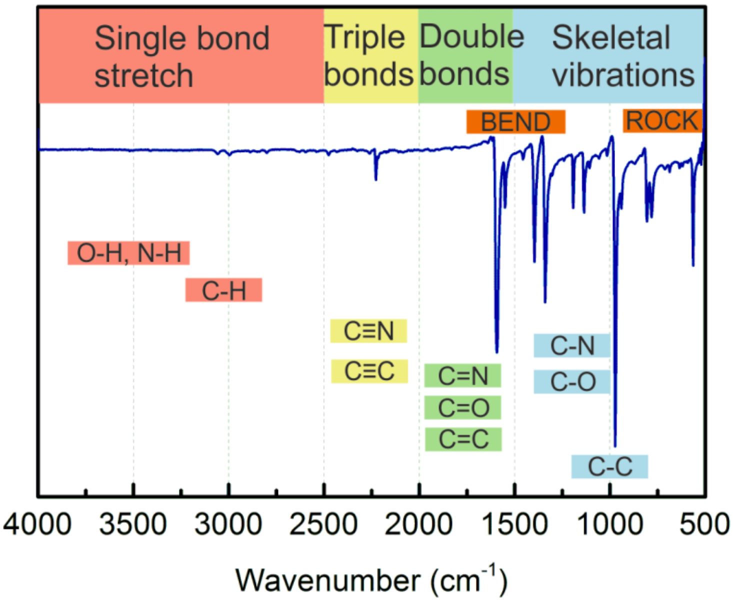

Figure 3.10. General schematic representation of the infrared vibrational spectra assignment on the example of the DTBDT-TCNQ compound (for details see Chapter 6). The spectrum was measured using the IR-spectrometer at Max Planck Institute for Polymer Research.

3.6. Theoretical calculations

Experiments on the electronic structure analysis are usually accompanied by theoretical calculations in order to have a realistic reference in the discussion. In the present work, two theoretical groups supported the NEXAFS experiments: Prof. Dr. Enric Canadell (Ballaterra, Spain) together with Prof. Dr. Jean-Paul Pouget (Orsay, France) performed calculations in the framework of the sudden state approximation and the group of Prof. Dr. Roser Valentí (Frankfurt am Main, Germany) calculated unoccupied states with the so-called *Z*+1/2 model that goes beyond the classical sudden state approximation. The present chapter gives a short overview on these two approaches used for discussions of NEXAFS experiments.

The first theoretical model is quite old and common and could be called even classical since many experimental NEXAFS works are supported by it [86], [88], [89], [98]. These calculations were carried out by the density functional theory (DFT) [99] using a numerical atomic orbital approach [100], which has been developed and designed for efficient calculations in large systems and implemented in the SIESTA code [100], [101]. The theoretical groups have used the generalized gradient approximation for the exchange correlation energy and, in particular, the functional of Perdew, Burke, and Ernzerhof [102]. Only the valence electrons are considered in the calculation, with the core being replaced by norm-conserving scalar relativistic pseudopotentials [103] factorized in the Kleinman-Bylander form [104]. The nonlinear core valence exchange-correlation scheme [105] is used for all elements with the exception of the hydrogen atom. Figure 3.11 shows an example of such a theoretical approach for the NEXAFS analysis of the TCNQ acceptor molecule. One can note that there is some discrepancy between theory and experiment, although it is possible to draw conclusions on the experimental data.

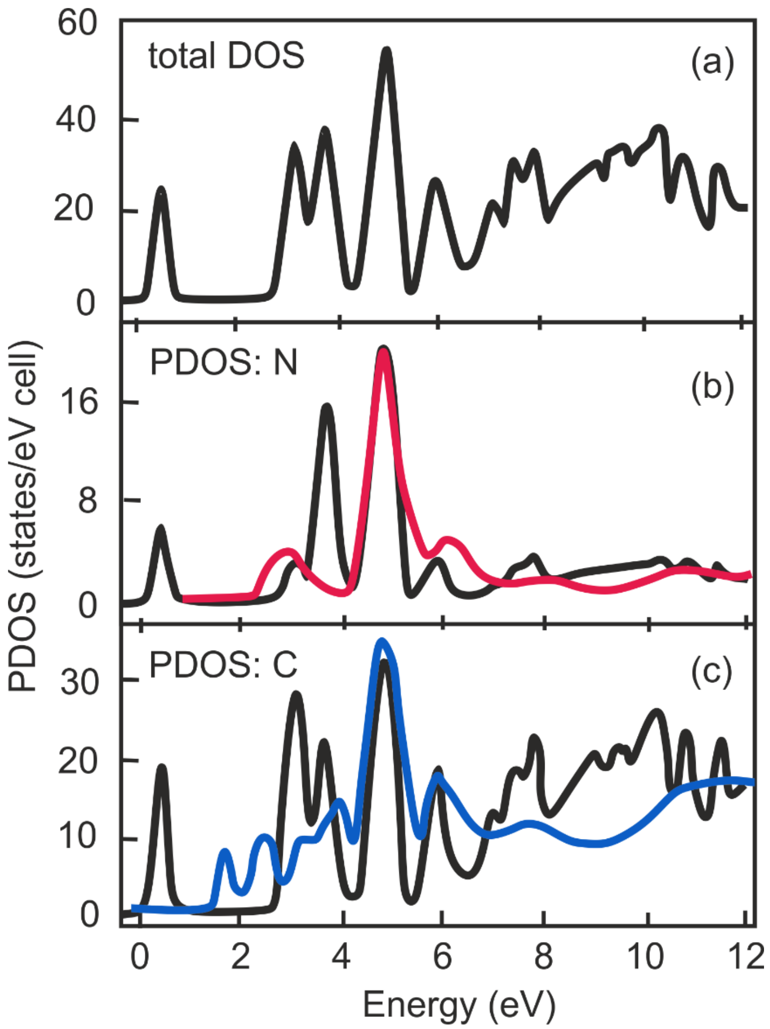

Figure 3.11. Total density of states (DOS) calculated for neutral TCNQ (a) and partial DOS (PDOS) for the nitrogen (b) and carbon (c) atoms (black lines). The experimental N1s (red line) and C1s (blue line) NEXAFS spectra of TCNQ are superposed to the PDOS of nitrogen and carbon, respectively (b, c) [94]. The energy is given relative to the LUMO minimum.

The second theoretical approach supports a model that goes further than the previous one. This method is used in the discussion of the electronic structure of novel charge transfer crystals DTBDT-TCNQ and DTBDT-F_4TCNQ (see Chapter 6).

In NEXAFS the final state has a hole in the core state and an additional electron in the conduction band. In order to provide a detailed interpretation of the NEXAFS measurements the group of Prof. Dr. Roser Valentí (Frankfurt am Main, Germany) have calculated NEXAFS spectra in the framework of DFT with four different methods: (i) The so-called *sudden state approximation* or ground state approximation which assumes that the time of the interaction of the X-ray photon with the electronic subsystem is much shorter than the typical timescale for spatial rearrangement of the electronic density. Therefore, the spectra can be calculated in terms of the ground-state (partial N or F) DOS. (ii) A method which improves upon the previous plain DFT density of states is the calculation of the excitation spectrum through *time-dependent DFT* (TDDFT) [106], [107]. These calculations were performed using the ORCA package [108]. (iii) A third approach which considers the screening of the electron-hole Coulomb correlation on a static level as well as the rearrangement of electronic density, is the *core-hole (supercell) approximation*. The idea of this approach is to remove one core electron (or a fraction of it) on one atom in the supercell and add it in the conduction band. These calculations were performed with the Wien2k package [109]. Here there are the key ingredients of the NEXAFS process but they are computer intensive, therefore (iv) the so-called *Z+1 approximation* was also tested. This method consists on replacing one N atom (for nitrogen K-edge NEXAFS) or one F atom (for fluorine K-edge NEXAFS) with atomic number Z by the neighboring atom with atomic number $Z+1$. This assumes that the lifetime of the excitation is much longer than the electronic timescale. A compromise between the two end cases (Z versus $Z+1$) can be obtained by considering a fractional $Z+1/2$. $Z+1$ and $Z+1/2$ calculations were performed with the FPLO package [110].

First the four methods were tested for the pure acceptors TCNQ (Fig. 3.12) and F_4TCNQ (Figs. 3.13 and 3.14). Since the spectra obtained in the FLAPW basis are generated via a product of the partial density of states, the corresponding matrix elements and transition probabilities, which cannot be directly compared to experiment in absolute value, the resulting spectra are shown in arbitrary units.

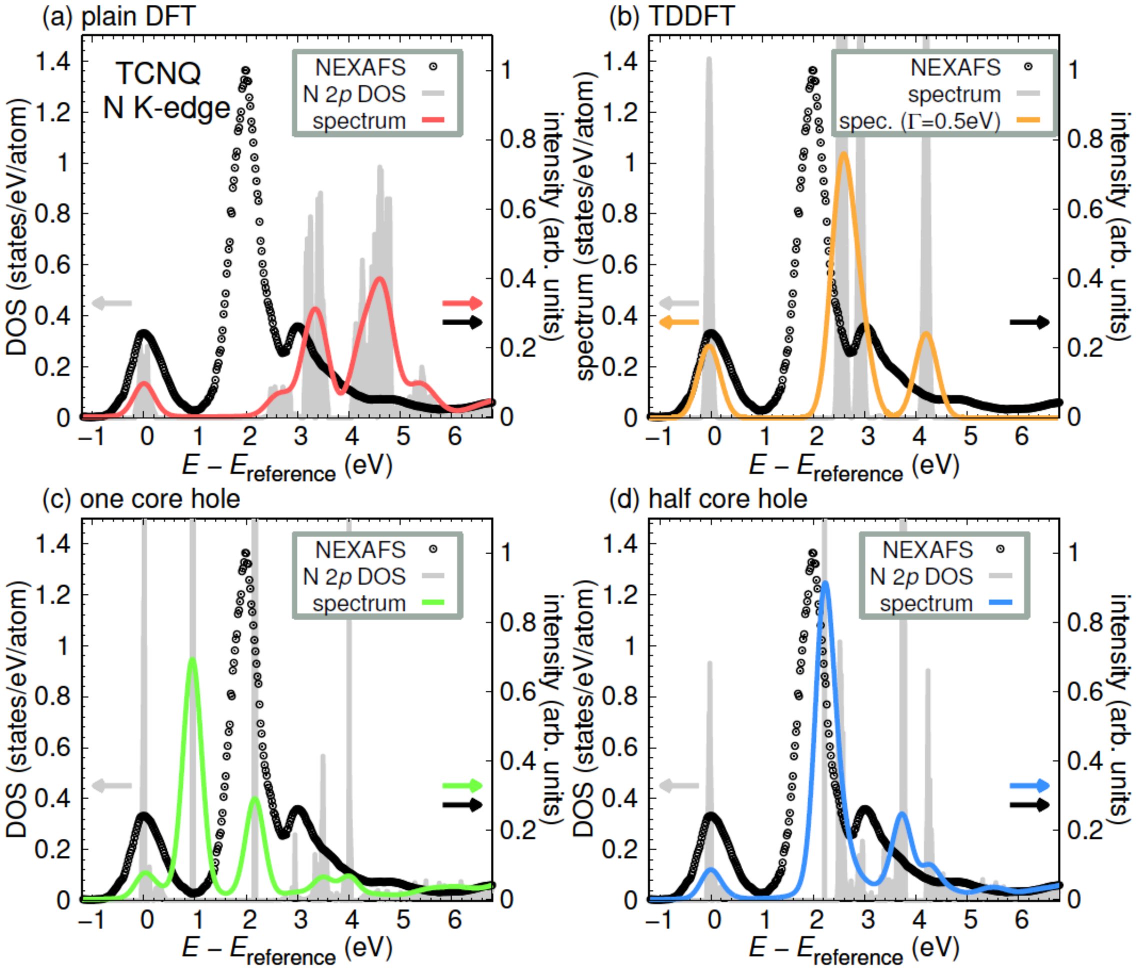

Figure 3.12. Nitrogen K-edge spectra for TCNQ calculated with various methods described in the text compared to experimental NEXAFS (circles), scaled to 1 at maximum intensity. The spectra (colored curves) in (a), (c), (d) were multiplied by the same factor to make them comparable. The spectrum in (b) was obtained from the DOS by convolution with an assumed half width of $\Gamma = 0.5$ eV. The energy scale is explained in the text.

A closer look at Figs. 3.12 and 3.13 shows that the sudden state approximation or plain DFT (case (i)) provides a very poor description of nitrogen K-edge NEXAFS for TCNQ. Neither the N 2p DOS on an atom in the molecule (shaded region in Fig. 3.12 (a)) nor its convoluted form (red line) reproduce the measured NEXAFS spectra. Previous works [86], [88] used this approach to identify the origin of the peaks observed in NEXAFS. However, in order to reach a reasonable agreement between theory and experiment, assumptions on energy shifts and on the absence of certain peaks in NEXAFS were necessary.

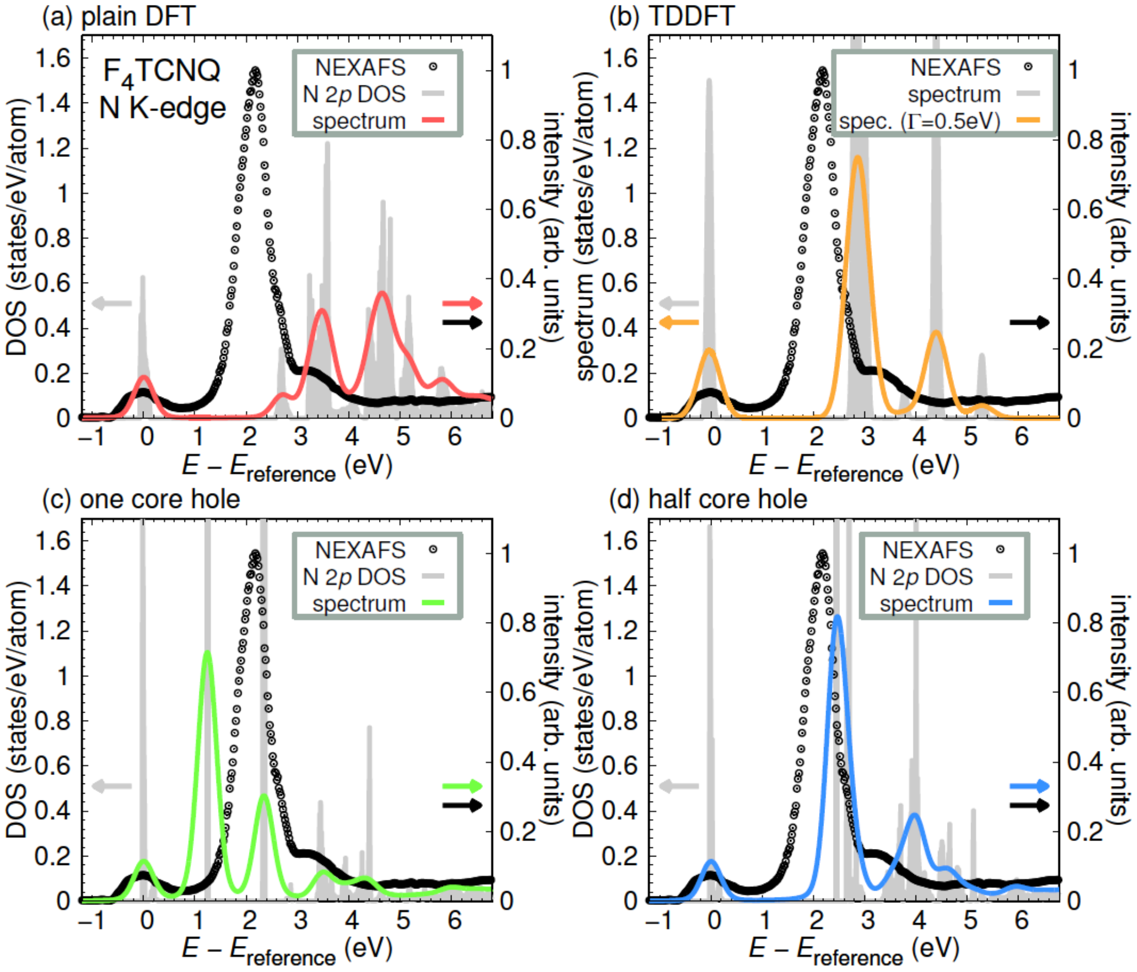

Figure 3.13. Same as Fig. 3.12 but for F_4TCNQ.

An improvement upon simple partial N 2p DOS was obtained by calculating the excitation spectrum of the system via TDDFT (Fig. 3.12 (b), case (ii)). The dominating peak of the theoretical spectrum (orange curve) is now only 0.55 eV above the experimental peak B and the spectral weights of the peaks agree reasonably well. Including the effect of the screening of one full core hole and corresponding rearrangement of the electronic density (Fig. 3.12 (c)) (case (iii)) produced the desired four main peaks observed in the NEXAFS spectrum but their position was not yet well accounted. However, when the strength of screening in the calculation was reduced by considering only half a core hole (Fig. 3.12 (d)), an excellent agreement with experiment was observed without further adjustment of parameters. A similar approach has proven successful for atomic calculations where the Slater integrals are reduced with respect to the Hartree-Fock values [111]. This

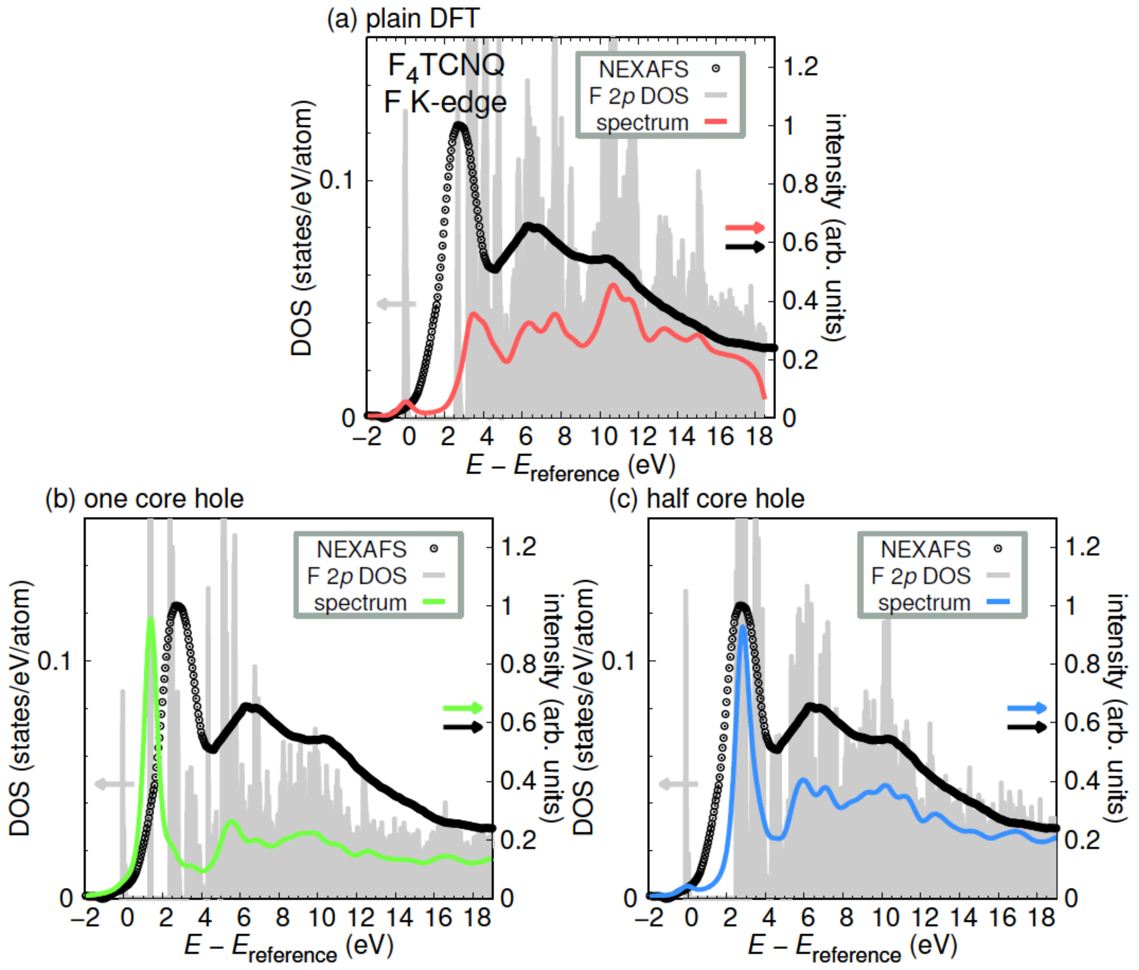

Figure 3.14. Fluorine K-edge NEXAFS spectra for F_4TCNQ calculated with various methods described in the text and compared to experimental data (circles) scaled to 1 at maximum intensity. The spectra (colored curves) were multiplied by the same factor to make them comparable. Experimental and theoretical spectra are aligned by choosing an appropriate reference energy $E_{\mathrm{refererence}}$ = 683.5 eV.

agreement was also observed in all other test cases considered (nitrogen and fluorine K-edge NEXAFS for F_4TCNQ) as shown in Figs. 3.13 and 3.14. This suggested to consider this approach as the method of choice. These calculations are, however, computer intensive and the theoreticians performed, as a last test, calculations with the much faster Z+1/2 approximation (case (iv)). This approximation gave for the systems studied here very similar results to the half core-hole approach (compare Fig. 3.12 (d) and 6.7 (a)). Hence all computations hereafter were performed using the Z+1/2 method. The experimental and theoretical spectra were aligned by choosing an appropriate reference energy $E_{reference}$. In the case of the experimental spectra, this is the maximum of the first observed peak, which means that $E_{reference} \approx 396.2$ eV in the case of nitrogen K shell spectra. Note that the precise value of this energy was dependent on the day to day calibration of the photon beam energy, varying by not more than 0.5 eV. For the theoretical spectra, $E_{reference}$ corresponds to the energy of the lowest unoccupied peak in the density of states, corresponding to the LUMO level. More details and the discussion in comparison to the NEXAFS experiments are given in Chapter 6.

4. Magnetic and electronic properties in the organic conductor $(DOEO)_4[HgBr_4]\cdot TCE$

4.1. $(DOEO)_4[HgBr_4]\cdot TCE$: state of the art

This part of the work is devoted to the asymmetrical DOEO molecule (1,4-(dioxandiil-2,3-dithio)ethylenedithiotetrathiafulvalene) packed in two dimensional layers and quasi-two dimensional organic conductor crystals $(DOEO)_4[HgBr_4]\cdot TCE$ (where TCE is 1,1,2-trichloroethane) (Fig. 4.1). More details about the synthesis of this material is given in [32]. The molecular structure of DOEO has a base skeleton similar to BEDT-TTF but the non-coplanar dioxane fragment makes adjustments to the packing layers of cation-radicals and therefore shows some notable differences to the well-known κ-BEDT-TTF family members. The metal anion ($HgBr_4^{2-}$) has a closed shell configuration and carries no spin.

The optical and conductive properties of the charge transfer salt $(DOEO)_4[HgBr_4]\cdot TCE$ were described in detail in [32], [112], [113]. The room temperature *dc* conductivity of crystals measured along the *a*-direction within the *ab* plane is $R_{RT} = 5\ \Omega^{-1}\mathrm{cm}^{-1}$ (Fig. 4.2). Resistivity perpendicular to the conductive plane is four orders of magnitude smaller. Upon cooling the resistivity R increases until a maximum around $T = 120$ K, and then decreases until $T = 70$ K where the resistivity shows a minimum. With further cooling, R again increases in the temperature range of 50 - 4.2 K. In [113], [112] it was reported that the possible reason of the non-monotonous temperature dependence of the $(DOEO)_4[HgBr_4]\cdot TCE$ resistivity could be the charge carrier localization due to the disorder in the anion and cationic subsystems.

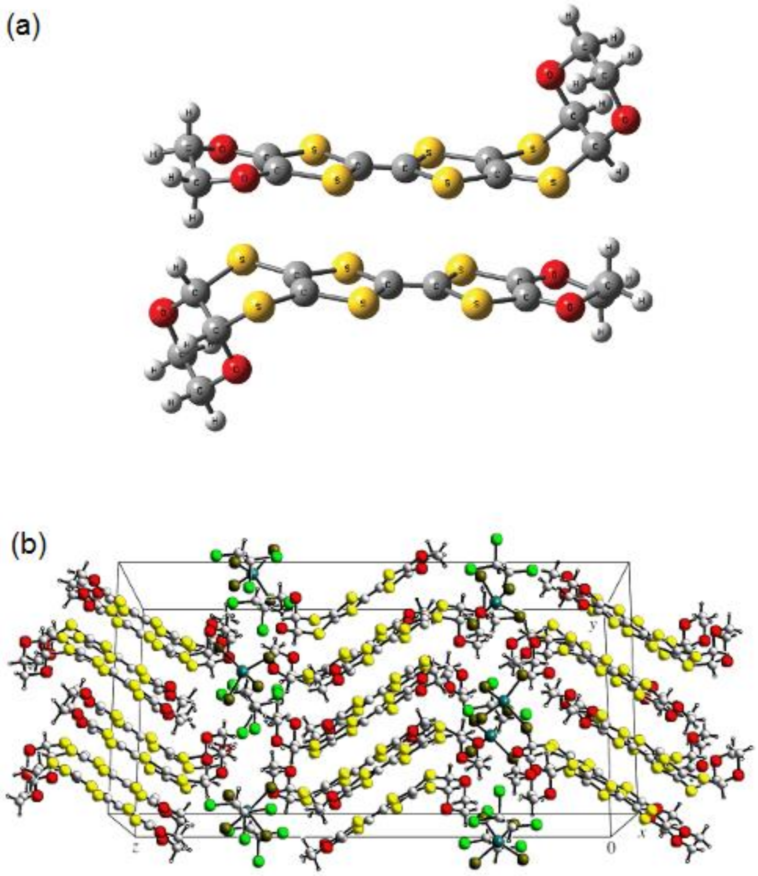

Figure 4.1. Structures of the molecular dimer DOEO (a) and a $(DOEO)_4[HgBr_4]\cdot TCE$ crystal (b), revealed in [32], [112], [113], [114].

Raman scattering investigations showed that the crystals are quasi-one-dimensional conductors down to 140 K, while below this temperature the conductivity behavior becomes similar to the behavior typical for quasi-two-dimensional compounds [113]. The highest occupied molecular orbital (HOMO) of the DOEO molecule of π character constitutes the 2D valence band. An energy gap forms by two coupled DOEO molecules in the HOMO band. Therefore, the HOMO band is expected to be nominally quarter-filled.

According to X-ray diffraction data at room temperature [32], the following types of structural disorder were observed: the cationic subsystem of ethylene groups in DOEO can occupy two nonequivalent positions, solvent molecules and anions are also partially disordered. At 30 K a partial ordering of each of these subsystems was found. Electron spin resonance revealed two types of localized spins (Fig. 4.3) with different local magnetic fields below 70 K. These measurements were performed in frames of my Diploma Thesis [115] and published in [116], [117].

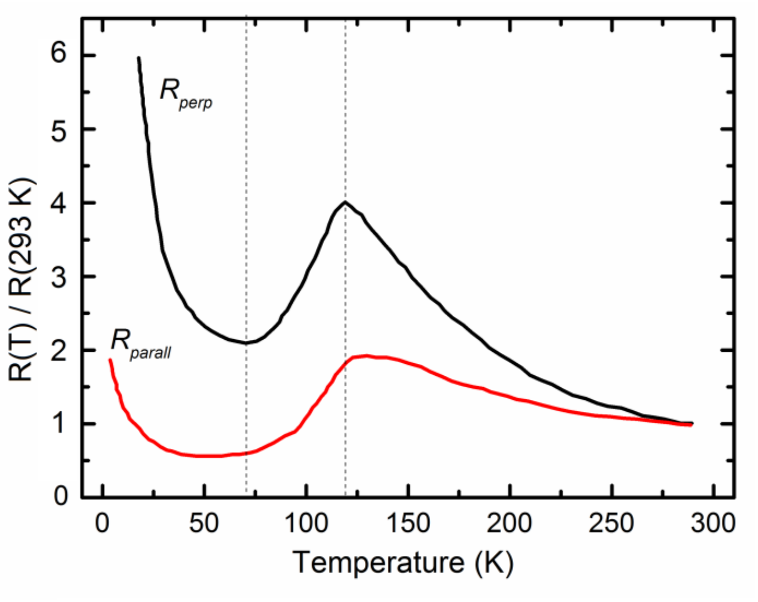

Figure 4.2. Temperature dependence of electrical resistivity in the DOEO plane (R_{parall}) and in the direction perpendicular to this plane (R_{perp}). (from [32])

For the novel charge-transfer salt $(DOEO)_4[HgBr_4]\cdot TCE$ there were no existing systematic characterizations of any phase transitions, and it was unknown if this new compound fits the conceptual phase diagram of the BEDT-TTF-family. The combination of several physical properties including electrical conductivity, static and dynamic magnetic susceptibility allowed us to propose a phase model for $(DOEO)_4[HgBr_4]\cdot TCE$ as a representative of a new class of DOEO-based charge transfer salts with asymmetric organic cations.

4.2. Sample preparation and experimental details

The $(DOEO)_4[HgBr_4]\cdot TCE$ single crystals were prepared with the electrocrystallization method in constant current mode as previously reported [32]. Their crystallographic structure was described in detail in [32]. The temperature dependence of the magnetic moment M of the samples was measured in the 2-300 K range at the constant field H = 0.1 T using SQUID magnetometer (type MPMS 5XL, Quantum Design). The diamagnetic contribution of the sample holder at T = 300 K was less than 1% of the signal.

The magnetic moments at each temperature $M(T)$ were referenced to the *dc* molar magnetic susceptibility $\chi_{exp} = M/\nu H$ (Fig. 4.4).

The high frequency spin dynamics measurements were explained in details in [116]. Here these results will not be discussed in detail, but the temperature dependence of ESR parameters will be used for the discussion. The electron transport properties are described in [32] and are used in the present work for comparison.

The XPS analysis[2] utilized Mg K_α radiation ($h\nu = 1253.6$ eV), while hard X-rays were used at the P09 HAXPES end station of the storage PETRA III (Hamburg) at a photon energy of 6000.5 eV [82], [83], thus providing two different scenarios of the probing depth. The XPS and HAXPES measurements were performed using two hemispherical analyzers (type SPECS Phoibos 150 and Phoibos 225 HV) for the standard and high-energy range, respectively. The full width at half maximum (FWHM) resolution was about 0.9 eV and 0.4 eV for XPS and HAXPES, respectively. All spectra were acquired at normal emission. Due to the large inelastic mean free path of the fast electrons the probing depth in HAXPES was about 8 - 10 nm and thus surface contaminations or the termination of the surface in the compounds play only a minor role. Due to this large probing depth, several layers of DOEO molecules contributed to the photoelectron signal in the HAXPES measurements. So the interlayer conductivity might become visible in this spectral range. The combination of core-level and valence photoemission spectroscopy was generally necessary for providing a full picture of the electronic structure. Comparison of XPS and HAXPES spectra thus allowed us to draw conclusions about the surface termination of the as-grown crystals.

---

[2] The XPS data were acquired and discussed in collaboration with the group of Prof. Dr. Roman Morgunov (Institute of Problems of Chemical Physics, Russian Academy of Science, Chernogolovka).

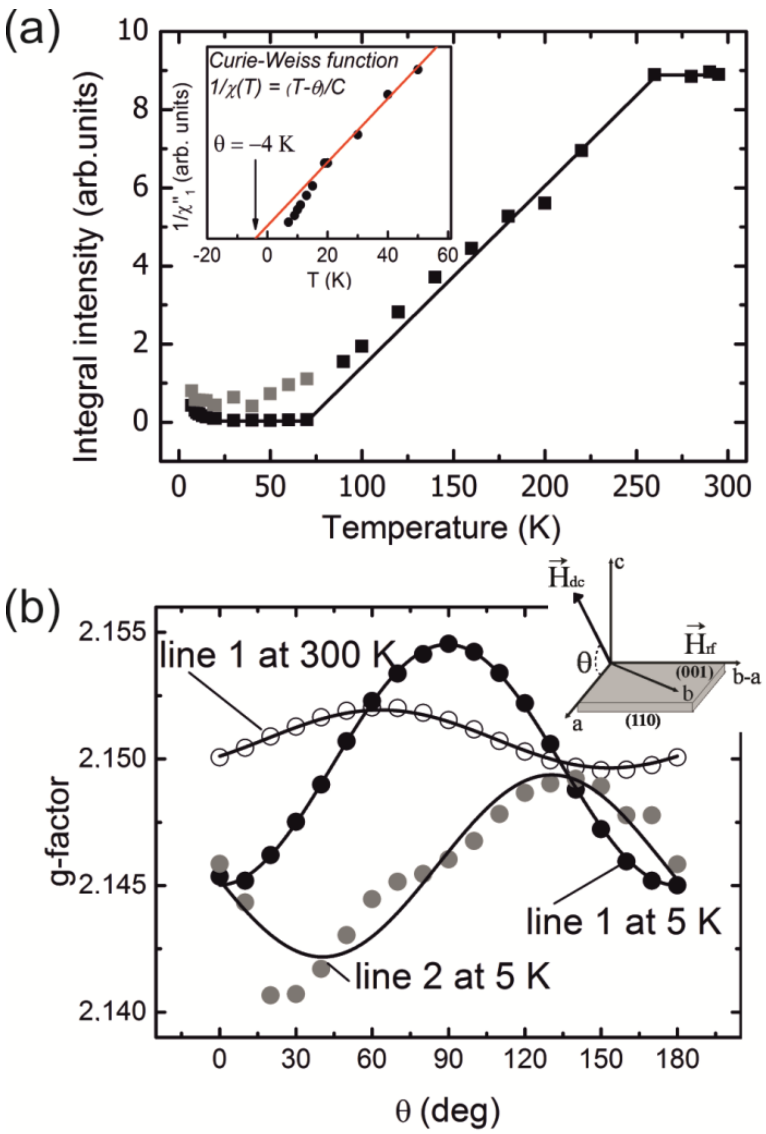

Figure 4.3. Temperature dependence of the ESR integral intensity of two different lines (black and gray symbols, (a)), The inset shows $1/\chi''$ versus T with a linear fit (red line) [116]. (b) The "out-of-plane" angular dependence of *g*-factors of a $(DOEO)_4[HgBr_4]$·TCE crystal obtained from the ESR spectra at $T = 5$ K for line *1* (black symbols) and line *2* (grey symbols). Open symbols give the angular dependence of line *1* at $T = 300$ K. The inset shows the orientation of the microwave and static magnetic field of the spectrometer with respect to the crystal, as well as the direction of sample rotation. The solid lines are approximations of the angular dependences by the spin Hamiltonian corresponding to axial symmetry [116].

4.3. Magnetic properties

Magnetic properties of the novel materials are usually investigated by SQUID magnetometry. Due to this technique being very sensitive and because it records all the possible contributions, it is useful to compare the *dc* magnetic susceptibility with *ac* characteristics obtained by electron spin resonance (ESR).

The ESR spectrum of a $(DOEO)_4[HgBr_4]\cdot TCE$ crystal from [116] contains a line of Lorentzian shape in the 4 – 300 K temperature range. At higher temperatures, 70 – 300 K, this line possesses an axial angular dependence inherent to delocalized charge carriers in the organic conductors (Fig. 4.3). Below T = 70 K the ESR spectrum is split into two anisotropic lines *1* and *2*. The narrow line *1* (linewidth ~ 0.5 - 4 mT) which was also observed at high temperatures lies on the low-field wing of the wide line *2* (linewidth ~ 2 - 8 mT). The decomposition of the spectra recorded in different orientations into two Lorentz lines results in angular dependencies of the *g*-factors of lines *1* and *2* (Fig. 4.3). Obvious differences of the angular dependences at 300 K and 5 K, as well as pronounced differences between angular dependences of lines *1* and *2,* indicate the presence of two distinct paramagnetic centers corresponding to different crystal fields. A sharp increase of the sample resistivity below 70 K was observed in [32], [112], [113], [114] and confirmed in special measurements for the crystal subjected to ESR studies.

As the SQUID technique detects the sum of all magnetic moments, the contribution of magnetic impurities was subtracted during our measurements. These can be dislocations in the crystall and defects in the molecular packing in the $(DOEO)_4[HgBr_4]\cdot TCE$ crystal. The fit of the local impurity magnetization was described by the Curie temperature dependence $\chi_{imp}(T) = C/T$, assuming that the impurity spins are uncoupled. A second, temperature-independent contribution to the experimental susceptibility is given by the diamagnetic component χ_{dia}, which is mainly caused by the *p*-states of the aromatic rings. χ_{dia} was estimated according to [118] from the molecular weight resulting in the constant value $\chi_{dia} = -1\cdot10^{-3}$ emu·mol^{-1}Oe^{-1}, i.e. the dotted line at the bottom of Fig. 4.4. The $\chi_{imp}(T)$ and $\chi_{dia}(T)$ were subtracted from the experimentally determined susceptibility (see Fig. 4.4), $\chi_s = \chi_{exp} - \chi_{dia} - \chi_{imp}$.

At 300 K the magnetic susceptibility assumes a value of $\chi_s = 2.68 \cdot 10^{-3}$ emu·mol^{-1}· Oe^{-1} and it increases with decreasing temperature for 280 K < T < 300 K. This suggests a Curie-Weiss-like behavior. Assuming a spin $S = 1/2$ per DOEO dimer, and taking into account the unit cell volume and the number of dimers in one unit cell, the expected saturation value of the magnetic moment per unit cell is $\mu_{u.c.} = N_s g S \mu_B / V_{u.c}$.= $1.1 \cdot 10^4$ emu·mol^{-1}, with the number of spins per unit cell $N_s = 8$, the gyromagnetic factor g, the Bohr magneton μ_B and the unit cell volume $V_{u.c.}$ Then, the approximation of uncoupled spins $S = 1/2$ gives a susceptibility of $\chi_{theor} = \mu_{u.c.}\mu_B/(k_B T) = 2.5 \cdot 10^{-3}$ emu·mol^{-1}·Oe^{-1} at T = 300 K, where k_B is the Boltzmann constant.

The experimental value is slightly larger than the theoretically predicted one. This may be attributed to the presence of a small orbital moment in addition to the spin moment. An orbital moment must be present because of the observed anisotropy of the g-factor [116]. The good agreement subsequently confirms the extraction of χ_s from χ_{exp}. For 120 K < T < 280 K χ_s shows an almost constant behavior with a small decrease with decreasing temperature. This is in contrast to the expectation for localized and uncoupled spins. No antiferromagnetic coupling can be expected at this high temperature. Instead we tentatively assume that the constant susceptibility reflects the Pauli-susceptibility for itinerant electron states being proportional to the density of states at the Fermi level. Although the charge-carrier density is constant and the scattering rate is expected to increase with temperature, the resistivity decreases in this region. Obviously, the charge transport cannot be explained by a simple model.

The region 70 K < T < 120 K is governed by a stronger increase of the susceptibility, indicating a stronger increase of the density of states with increasing temperature. This might be explained by an Anderson-Hubbard scenario, where electron correlation suppresses the charge carrier density [119] forming a soft gap that is partly filled with increasing temperature. Because in this temperature region the resistivity increase is considerably larger than the increase of the charge density, the charge transport properties are dominated by the scattering rate like in a normal metal.

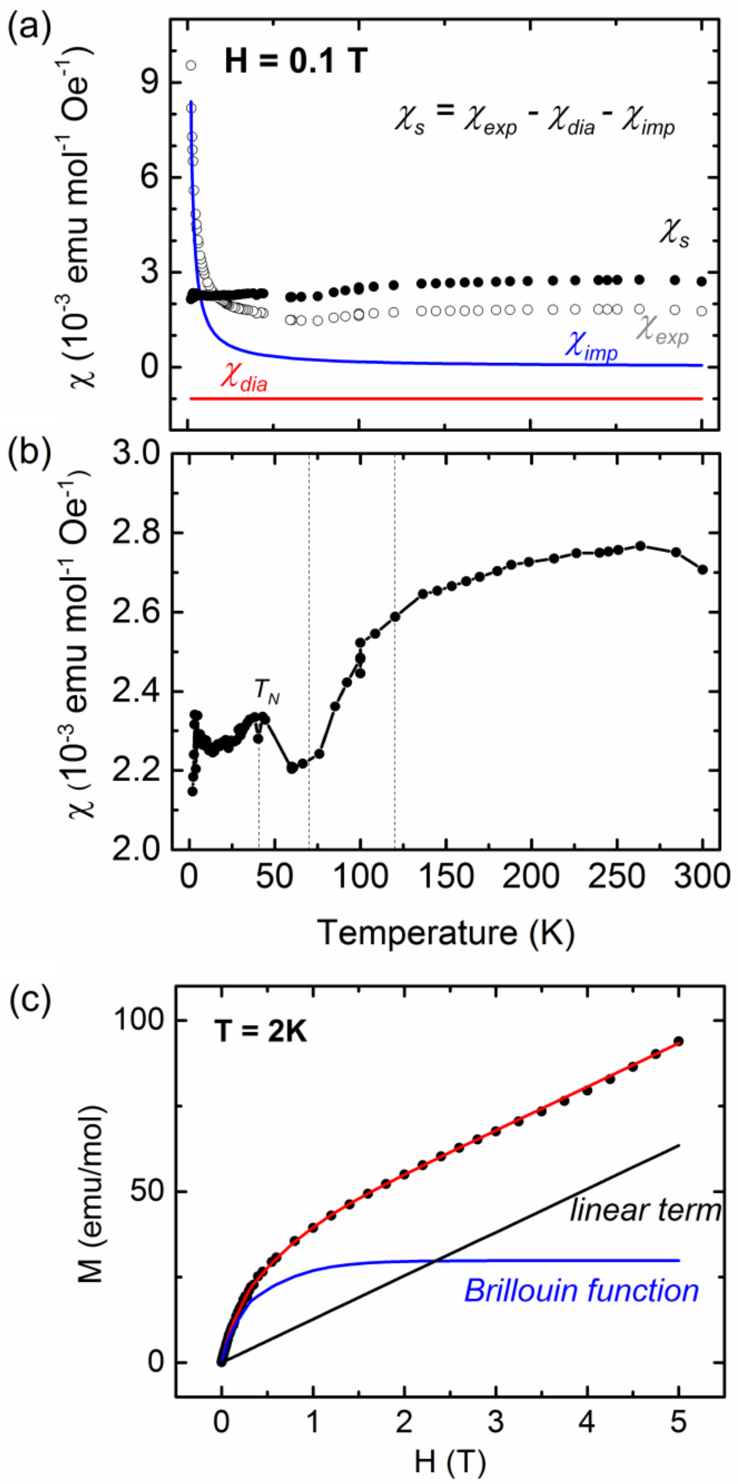

Figure 4.4. Temperature dependence of the *dc* magnetic susceptibility χ of a (DOEO)$_4$[HgBr$_4$]·TCE crystal as determined by SQUID in a constant magnetic field 0.1 T (a). The experimental data of the measured magnetic susceptibility (open circles) are decomposed into the diamagnetic component of the sample (red line), Curie-Weiss component (blue line) and the true (DOEO)$_4$[HgBr$_4$]·TCE component after subtraction of these contributions (full circles). The latter curve is shown on an enlarged scale in (b). (c) Field dependence of the magnetic moment of a (DOEO)$_4$[HgBr$_4$]·TCE crystal at $T = 2$ K from the SQUID data (dots). The red solid line shows the fit of the magnetic moment with a sum of a Brillouin function (blue curve) and a linear term (black line).

Both in the metal and in the semiconducting phase the ESR signal increases monotonously. As ESR detects localized electrons (or holes) and not itinerant electrons [117] this behavior could be explained by an increasing electron localization due to scattering in parallel to the increasing density of itinerant states.

Below 70 K the susceptibility reveals a nonmonotonous behavior with a maximum at 40 K. Such a maximum can be explained by an antiferromagnetic interaction between localized spins with an ordering temperature T_N close to the maximum. Further evidence for antiferromagnetic interaction is given by the ESR data revealing a linear increase of $1/\chi$ and a negative axial section $T = \theta = -4$ K. The increase of resistivity in this temperature region with decreasing temperature indicates a thermally activated transport requiring an energy gap in the density of states. This behavior would be compatible with the Anderson-Hubbard scenario mentioned above, but it is of course no proof. Although the increase of resistivity with decreasing temperature is comparatively small, this phase could be named insulating.

The main question to be answered by magnetometry concerns the nature of the low temperature magnetic state of the localized carriers in the crystals. Measurements of the magnetic field dependence of the magnetization were performed to clarify this problem (Fig. 4.4 c). The Figure shows the field dependence of the $(DOEO)_4[HgBr_4]$·TCE molar magnetic moment. The experimental data was approximated using a sum of a linear function and a Brillouin function for the spin S [120]:

$$B_S(x) = \frac{2S+1}{2S} coth\left(\frac{2S+1}{2S}x\right) - \frac{1}{2S} coth\left(\frac{x}{2S}\right), \tag{4.1}$$

where

$$x = \frac{S g_M \mu_B H}{k_B T}, \tag{4.2}$$

It is assumed that the Brillouin function is associated with a small amount of impurities (i.e. unpaired and uncoupled spins) in the sample. The fit to the experimental data indicates a spin of S=10 corresponding to paramagnetic metallic nanoparticles. The linear term corresponds to the true susceptibility signal from the unpaired electrons within the crystal. The impurity component is very large at low fields and low temperatures compared to the linear component. Considering the absolute value of the total magnetic moment one obtains a different result. For the total magnetic moment, one must consider the saturated moment in infinitely large external magnetic fields. In this case the linear term becomes much larger (more than 95 %) than the impurity contribution. When subtracting the impurity contribution, the magnetic susceptibility is almost constant, indicating the dominant temperature-independent Pauli paramagnetism due to delocalized electrons. The small deviation from the constant susceptibility above 50 K nicely fits to the temperature dependence of the number of localized electrons discussed above that provoke a Langevin-paramagnetism with spin S=1/2. A small maximum near 40 K might indicate the onset of antiferromagnetic order.

The crystal structure and low concentration of holes (one hole per molecular dimer [32], [112], [113], [114]) explain the small value for the observed long range intermolecular exchange interaction because intermolecular distances exceed ~ 10 Å. The occurrence of antiferromagnetic long and short range order may explain the existence of a second ESR line *2* as an antiferromagnetic resonance. As an independent confirmation of this aspect, one may see the different temperature dependence of the integral intensity of line *2* [116].

4.4. Electronic properties

Since the electronic structure defines the physical properties of the crystals, $(DOEO)_4[HgBr_4]\cdot TCE$ crystals were investigated using photoemission.

XPS and HAXPES spectra of $(DOEO)_4[HgBr_4]\cdot TCE$ crystals were taken in the temperature range 45 K – 300 K. The survey XPS spectrum of the DOEO salt taken at room temperature shows all the elements present in the material (Fig. 4.5 a). The spectrum contains the carbon, oxygen, and sulfur signals corresponding to the conductive DOEO stack layers as well as mercury and bromine present in the anion sublattice and chlorine from the TCE solvent.

A HAXPES survey spectrum of the shallow core levels, recorded at room temperature, is shown in Fig. 4.6 a. Like in the XPS case, the spectrum contains the signals of all DOEO components, however, with substantially different intensity ratios. This reflects the difference in the partial photoemission cross sections. Chlorine of the solvent molecules, embedded in the anionic layer, is also observed. At room temperature the signals are well resolved and non-split.

For further evaluation the Hg 4f and S 2p XPS lines are discussed as signatures of anion and cation, respectively (Fig. 4.5 b, c). In the case of HAXPES the Hg 4d, S 2s and Cl 2p signals are used as a probe for the anion, the DOEO molecule and the solvent component, respectively (Fig. 4.6 b, c). All evaluated lines are well suitable for the quantitate discussion, because their intensities are large and the component structure is very pronounced. The decrease of HAXPES photoemission cross section with increasing kinetic energy is less pronounced for s-states than for higher angular momentum states. Hence it was possible to study the S 2s level at a good intensity.

When comparing the relative intensities of the anionic components mercury and bromine, their intensities in the HAXPES survey spectrum are much higher than those for the surface-sensitive XPS in comparison to signals of C 1s and O 1s that have the largest intensities in the spectra (see Figs. 4.5 a and 4.6 a). The S/Hg and S/Br XPS ratios calculated using the experimental data and cross section constants from [118] are higher than expected from the composition, suggesting that the surface of the as-grown crystals is mainly terminated by the layer of DOEO molecules. HAXPES, with its large probing depth, provides spectroscopic access to the buried anionic layers. This general finding of termination of the surface by a DOEO layer is in agreement with results from scanning tunneling spectroscopy (STS) on the related compound $(BEDT\text{-}TTF)_2Cu[N(CN)_2]Br$, where tunneling spectra of as-grown crystals provided direct evidence of the states in the cationic layers in the superconducting phase [119].

Due to non-monotonic behavior of transport [32] and spin properties [116], it is interesting to follow the development of the photoemission spectra with cooling. At 200 K the Hg 4f XPS spectrum (Fig. 4.5 b) displays the Hg 4 $f_{7/2}$ and 4 $f_{5/2}$ spin-orbit doublet, appearing at 100.5 and 104.5 eV respectively. The additional third peak appearing in the Hg 4f region, located at 102.2 eV, can be associated with Si oxides, whose presence is likely due to surface contaminants. The HAXPES line shown in Fig. 4.6 b, presenting the same element of the anion, is Hg 4d. It also shows a fine-structure doublet of Hg $4d_{3/2}$ and

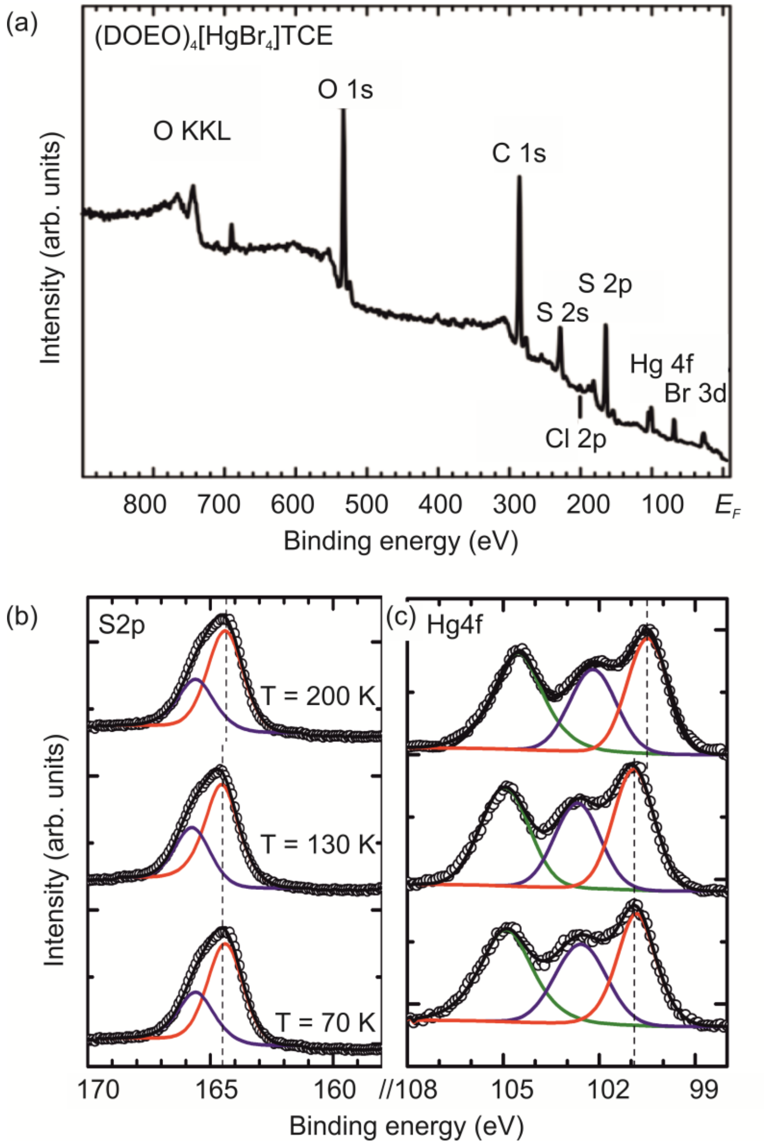

Figure 4.5 (a) Survey of XPS spectrum on the surface of the $(DOEO)_4[HgBr_4]$·TCE crystal taken at room temperature, (b) example of the temperature behavior of Hg 4f core-level XPS spectra at T = 200 (top), 130 (center) and 70 K (bottom), (c) example of the S 2p core-level spectrum decomposition at T = 200 (top), 130 (center) and 70 K (bottom). Circles show the experimental results, solid lines represent the deconvolution of the spectra by a least squares fit. In both cases the sum spectrum of the deconvoluted peaks agrees perfectly with experiment.

Hg $4d_{5/2}$. In the HAXPES spectra of Hg, a further splitting at room temperature is not observed because the surface contribution is very small in comparison to the bulk contribution of several anionic layers. Furthermore, a signal from Si (at about 102 eV binding energy) is invisible in the bulk, proving the appearance of this line in XPS due to surface features. The HAXPES spectrum of Cl 2p, which is also a fingerprint of the anionic layer (where also the TCE solvent molecules are located), at 200 K consists of a single line. Normally, the Cl 2p has two contributions located at about 200 and 202 eV binding energy due to the spin-orbit splitting. In the present experiment it is impossible resolve this difference. A main contribution to peak broadening is associated with the rich phonon spectra of the $(DOEO)_4[HgBr_4]\cdot TCE$, in addition to lifetime broadening effects.

The S 2p XPS level (see Fig. 4.5 b) at 200 K is the convolution of a spin-orbit split doublet in which the binding energies of the S $2p_{3/2}$ and the S $2p_{1/2}$ core levels are 164.2 and 165.3 eV, respectively, and of another doublet, characterized by a significantly lower intensity, with binding energies of 165.4 and 166.5 eV for the $2p_{3/2}$ and $2p_{1/2}$ components, respectively. The presence of two S 2p doublets can be associated either with photoemission from nonequivalent S sites in the DOEO molecule, or with the presence of DOEO molecules with different charge states as it is proposed in Fig. 4.7. The in-plane conductivity in $(DOEO)_4[HgBr_4]\cdot TCE$ is about four orders of magnitude higher than in perpendicular to the DOEO layer direction [32] causing the layered charge distribution at the sub-surface region. Due to dependence of core-level positions on the electrostatic environment of the emitter atom, a series of relatively core-level signals appears at entering the charge localization low-temperature regime. Similar observations are reported in the literature for the photoemission from organic salts (see e.g. [121] and references therein).

The S 2s HAXPES line at 200 K (Fig. 4.6 c) exhibits a low-energy satellite signal, shifted by about 4eV. This satellite becomes stronger at 130 K, although the Hg 4d and Cl 2p lines do not show an indication of charging. We thus believe that the S 2s satellite (at about 232 eV binding energy in Fig. 4.6 c) indicates a true chemical shift. When cooling the crystals down to 130 K and therefore crossing the transition temperature to the metallic regime, a shift of 0.4 eV in both Hg 4f and S 2p XPS lines is observed. Similarly, there is a shift of about 1.5 eV to lower kinetic energies in all HAXPES spectra. The first sign of electron density redistribution between the S 2s component lines in the bulk becomes visible.

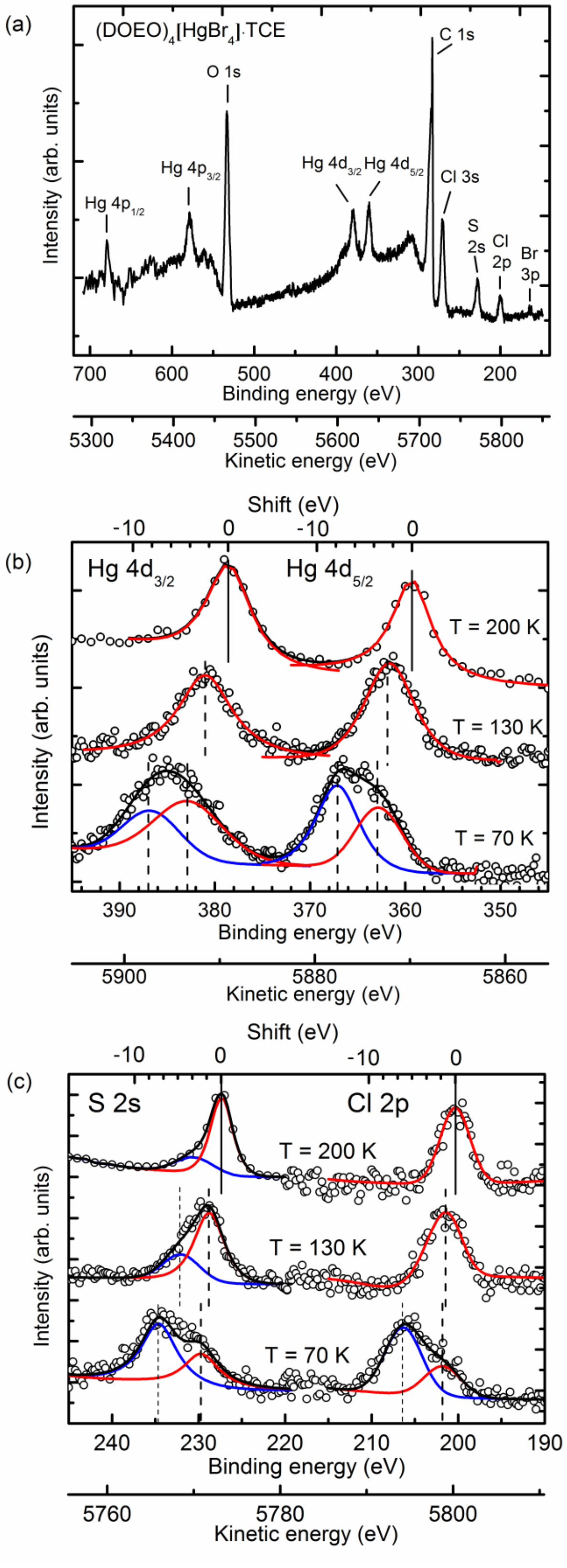

Figure 4.6. (a) Survey HAXPES core-level spectrum of $(DOEO)_4[HgBr_4]\cdot TCE$ taken at room temperature; (b) Mercury 4d (c) sulfur 2s and chlorine 2p HAXPES core-level spectra for three temperatures of $(DOEO)_4[HgBr_4]\cdot TCE$: $T = 200$ (top), 130 (center) and 70 K (bottom). Circles show the experimental results, solid lines represent the deconvolution of the spectra by a least squares fit. Vertical lines show the center positions of the deconvoluted peaks.

Upon further cooling to 70 K, Hg 4f and S 2p surface signals do not change. In contrast, additional split lines in Cl 2p, Hg 4d3/2 and Hg 4d5/2 from the bulk of the crystals appear and the spectra are shifted further by 2.2 eV in the same direction to lower kinetic energies. The low-energy satellite of the S 2s HAXPES signal becomes more significant in comparison to the higher temperatures (Fig. 4.6 c).

As a result, the observed shift of the XPS surface lines with cooling to 130 K is associated with surface charging of the crystal. The additional low-energy component of the S 2s HAXPES signal from the bulk is a true chemical shift. Upon further cooling to 70 K, the system becomes insulating and layer-wise charging is observed in the bulk, similar to the finding for $(TMTTF)_2SbF_6$ discussed in [12]. Therefore, using both XPS and HAXPES it is possible to follow and discuss not only surface vs. bulk differences, but also observe the interlayer conductivity change in layered organic compounds.

4.5. Correlation between transport, magnetic and electronic properties

The hypothesis about a transition from 1D electrical conductivity (at high temperatures) to 2D conductivity (below 140 K) proposed in [113] gives stimulus to study the temperature dependence of the electrical anisotropy. In order to quantify the electrical anisotropy, the ratio $R_{\perp}/R_{\parallel}$ of the “out-of-plane” $R_{\perp}$ and “in plane” $R_{\parallel}$ resistivity could be introduced using experimental data from [32].

Two facts become obvious from the comparison of temperature dependences of $R_{\perp}/R_{\parallel}$ and the XPS shift, both plotted in Fig. 4.8. Cooling of the crystal continuously increases the ratio $R_{\perp}/R_{\parallel}$ of the electrical conductivity towards two-dimensional behavior. This continuous “transition” of the electrical dimensionality is accompanied by the localization of holes that, in turn, leads to dielectric polarization of the sample. The additional evidence of localization (besides the resistance behavior itself [32], [112], [113], [114]) is a significant shift of the XPS signals towards lower kinetic energies, progressively

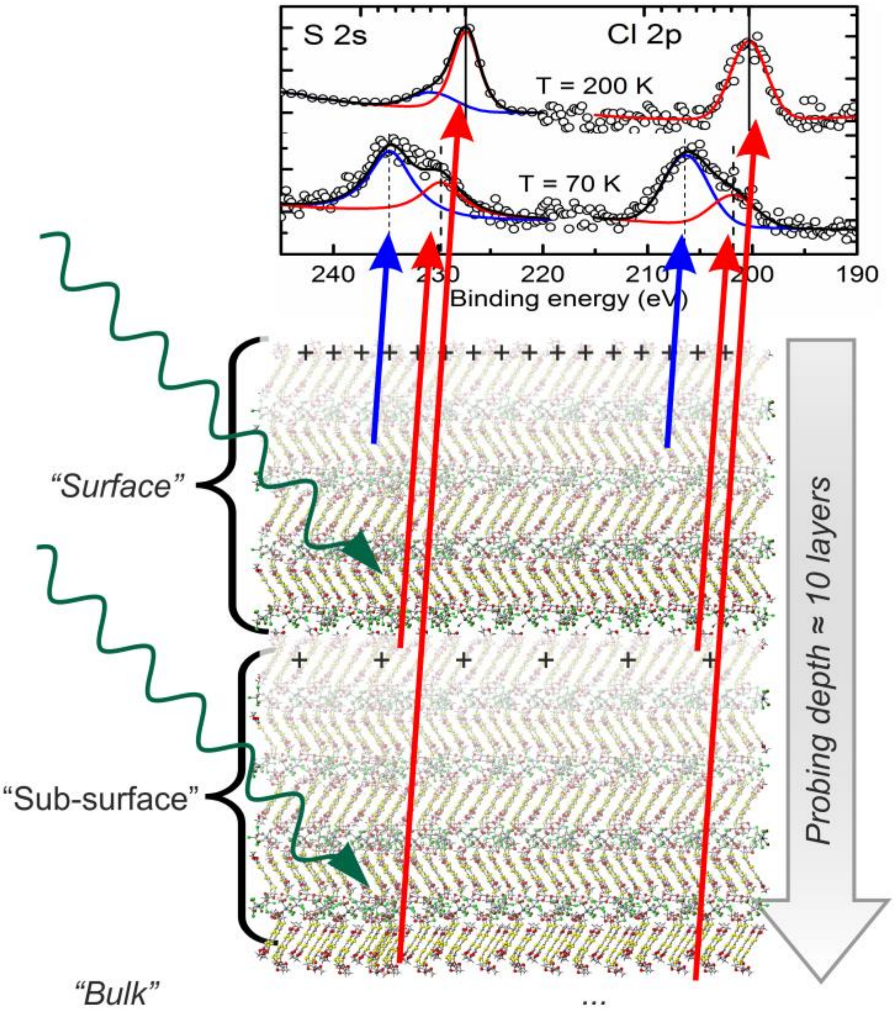

Figure 4.7. Schematic representation of the proposed model for the charge redistribution in $(DOEO)_4[HgBr_4]{\cdot}TCE$ causing the shifts in the HAXPES spectra (see text).

down to 140 K. The temperature dependence of the electrical anisotropy parameter $R_\perp/R_\parallel$ (triangles in Fig. 4.8) thus correlates with the temperature dependence of the level shifts in the XPS spectra (circles). In the DOEO layer, the conductivity originates from the transfer of holes between dimers through short contacts between “tail-to-head” molecules whose ends contain sulphur atoms. Furthermore, the intensity ratio of the HAXPES signals (i.e. the ratio of the area of the shifted line and the total area of shifted and non-shifted line, squares) also follows this trend. The net charge accumulated in the near-surface region in the steady-state equilibrium during irradiation with the hard X-rays is an indirect measure of the interlayer conductivity.

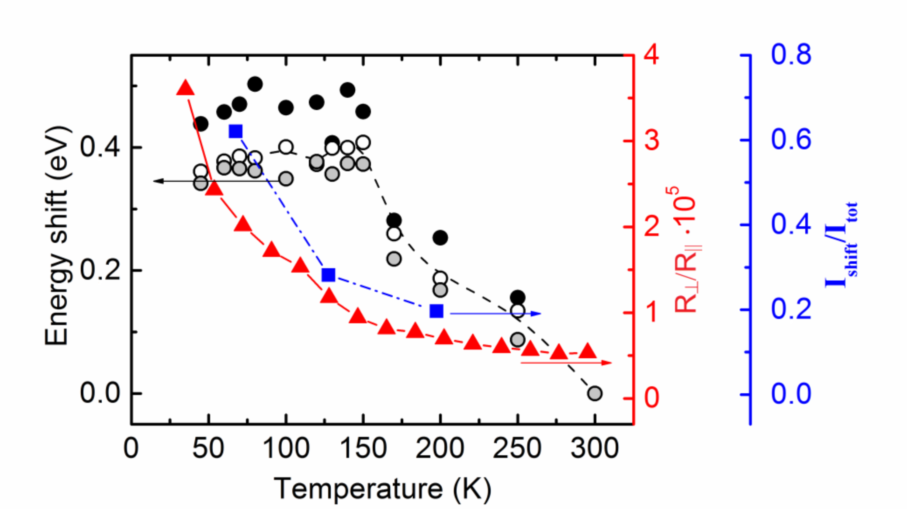

Figure 4.8. The temperature dependence of the shift of core levels of Hg (black circles), S (gray circles) and Br (white circles) in a (DOEO)$_4$[HgBr$_4$]TCE crystal, relative peak intensity of S 2s (blue squares, see Fig. 4.6 b) and electrical anisotropy parameter (see text) $R_\perp/R_\parallel$ (red triangles and read ordinate). Full, dashed, and dash-dot lines are to guide the eye, denoting the anisotropy parameter, the relative shift of the Hg and S core level positions (averaged), and the intensity ratio of the shifted S 2s HAXPES signal, respectively.

At low temperature an antiferromagnetic phase of localized holes coexists with paramagnetic individual localized holes in (DOEO)$_4$[HgBr$_4$]·TCE. The symmetry of the antiferromagnetic phase was found to be different in comparison with the symmetry of the ESR spectra of free charge carriers.

In the temperature region of 120-160 K the XPS spectra reveal characteristic level shifts of the order of 400 meV and the HAXPES spectra exhibit strongly shifted signals due to the buildup of non-equilibrium charge distribution in the near surface region. The XPS shifts reflect the surface charge within the first 1 nm, i.e. within the first DOEO layer. In contrast, the HAXPES shifts arise from a probing depth of about 8-10 nm, i.e. 5-7 DOEO layers. The intralayer conductivity is much higher than the interlayer conductivity. Hence, electrostatic decoupling of adjacent layers occurs as discussed in [12], leading to several separated signals. The temperature dependences of the continuous XPS level shift and the intensity ratio of the shifted signal versus the unshifted signals in HAXPES spectra are in accordance with the conductivity anisotropy parameter $R_{\perp}/R_{\parallel}$.

The comparison of XPS and HAXPES spectra provides information regarding the surface termination. XPS (probing depth about 1 nm) sees the surface and topmost DOEO layer, whereas HAXPES gives spectroscopic access to several buried cationic and anionic layers. The comparison indicates that the surface of the as-grown crystals is mainly terminated by a layer of DOEO molecules.

Continuous localization of holes results in non-monotonous variations of the resistivity and magnetization of the samples, corresponding to a competition between free charge carriers, individual localized holes, and condensed droplets containing large amounts of spins. The obtained data can be used to explain extraordinary electrical and magnetic properties of the $(DOEO)_4[HgBr_4]\cdot TCE$ crystals. Appearance of an antiferromagnetic phase below 60 K in a non-magnetic compound not containing metal atoms is evidence of the strong electron-electron correlation in this two-dimensional system.

4.6. Summary

The occurrence of characteristic changes in the temperature dependence of three different experimental properties: resistivity [32] (Fig. 4.2), integral intensity of the ESR signal [116] (Fig. 4.3 a), and magnetic susceptibility measured by SQUID magnetometry (Fig. 4.4 b), coincide at the critical temperatures T_1 = 70 K and T_2 = 120 K.

The temperature T_1 separates insulating from metallic behavior. The onset of insulating behavior at low temperatures has been observed for related charge-transfer salts such as (BEDT-TTF)(TCNQ) [122] and κ-(BEDT-TTF)$_2$Cu[N(CN)$_2$]Cl [2]. In contrast to the typical metal-insulator transition, only a relatively small increase of the resistivity observed below T_1. Similarly smaller changes of the resistivity have been observed if κ-(BEDT-TTF)$_2$Cu[N(CN)$_2$]Cl is tuned towards metallic behavior by a partial substitution of Cl by Br [123]. Therefore, the observed behavior of (DOEO)$_4$[HgBr$_4$]·TCE might indicate that the specimen is close to the border between the metallic and insulating ground state.

At the second transition temperature, T_2 separates true metallic-like behavior from semiconducting behavior. This is very similar to the case of κ-(BEDT-TTF)$_2$Cu[N(CN)$_2$]Br$_x$Cl$_{1-x}$ and explained by an onset of hopping conductivity [123].

In summary, a transition from insulating behavior (with a small or vanishing gap) to a metal and finally to a semiconductor is observed with increasing temperature. The proposed phase changes at the critical temperatures T_1 and T_2 observed for the charge-transfer salt (DOEO)$_4$[HgBr$_4$]·TCE is compatible with the conceptual phase diagram for the BEDT-TTF-family [64], considering (DOEO)$_4$[HgBr$_4$]·TCE to be very close to the boundary between insulating and metallic behavior.

5. Peierls transition and pre-transitional charge-density wave fluctuations in TTF-TCNQ

5.1. TTF-TCNQ: state of the art

The charge transfer salt TTF-TCNQ, where TCNQ is 7,7,8,8-tetracyano-*p*-quinodimethane and TTF is tetrathiafulvalene, was one of the first organic conductors synthesized (Fig. 2.2) [124]. The structure of TTF-TCNQ consists of segregated stacks of donor TTF and acceptor TCNQ molecules tilted with respect to the *b* axis and in opposite direction along the *a* axis [14]. The metallic properties of TTF-TCNQ exist due to a charge transfer of π electrons from the HOMO of the TTF to the LUMO of the TCNQ which overlap at the Fermi level. For a 1D electronic structure a value for the charge transfer is $\rho = 2\text{x}2k_F$, where k_F expressed in b^* units is the common Fermi wave vector of the 1D HOMO and LUMO bands). It was shown by structural measurements of the $2k_F$ Peierls critical wave vector that ρ increases from 0.55 at room temperature to 0.59 at low temperature [38], [125]. The 1D electronic structure and the k_F Fermi wave vector of TTF-TCNQ were more recently probed by photoemission [126], [127].

TTF-TCNQ exhibits a rich phase diagram, consisting of the establishment of successive $2k_F$ Peierls transitions at critical temperatures of 54, 49 and 38 K (see Fig. 5.1, 5.2; for reviews see [1], [124], [128], [129]). The 54 K Peierls transition opens a gap in the LUMO band structure due to the setting of a $2k_F$ charge density wave (CDW) modulation on the TCNQ stack along *b*. The TTF stacks begin to be CDW modulated below 49 K, which opens a gap in the HOMO band structure. Between 49 and 38 K the development of the TTF modulation reacts on the TCNQ CDW sub-lattice by inducing a progressive transverse sliding of the common modulation in the direction of *a*, along which stacks of donor and acceptor molecules alternate. At the first order 38 K phase transition, the *a** component of the CDW modulation wave vector locks to a commensurate value and the charge transfer ρ jumps from 0.586 to 0.590 [124]. The low temperature CDW modulated structure of TTF-TCNQ has been refined by diffraction [130] while the CDW modulation has been directly observed by STM [34].

Above 54 K the metallic phase of TTF-TCNQ is particularly interesting since the $2k_F$ CDWs develop pre-transitional 1D structural fluctuations on a large temperature range below 150 K [38], [125]. These fluctuations of individual TCNQ stacks consist in rigid translation of the TCNQ molecules, which leads to a $2k_F$ Kohn anomaly in the dispersion of the transverse acoustic branch polarized along *c** [131], together with an out-of-plane intramolecular deformation of the TCNQ [132]. These 1D $2k_F$ fluctuations couple 3D below 60 K, a few degrees above the 54 K Peierls transition [125]. The 1D pre-transitional fluctuations located on the TTF stacks are dominated by the formation of a $4k_F$ CDW instability [37], [38], [125] which, at twice the $2k_F$ wave vector, is the fingerprint of important electron-electron repulsions on the donor stack [33].

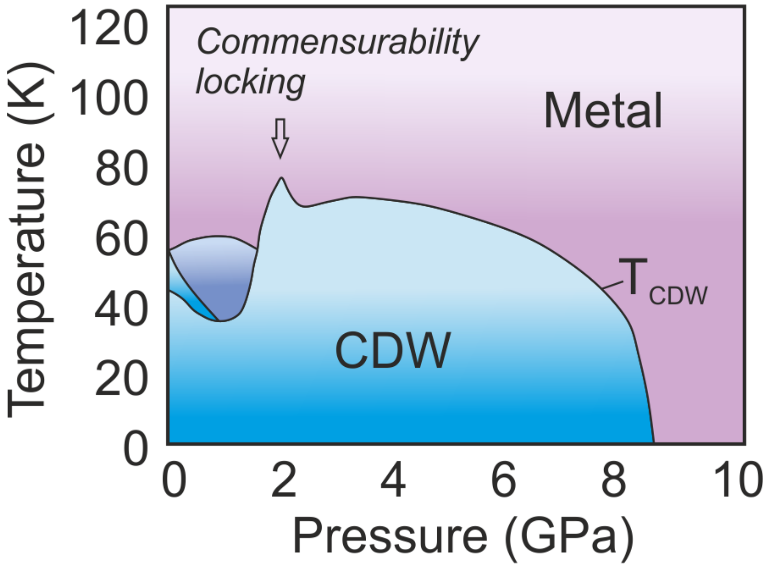

Figure 5.1. The pressure-temperature phase diagram of the TTF-TCNQ adopted from [133], [24]. Blue regions denote three different charge density wave (CDW) phases.

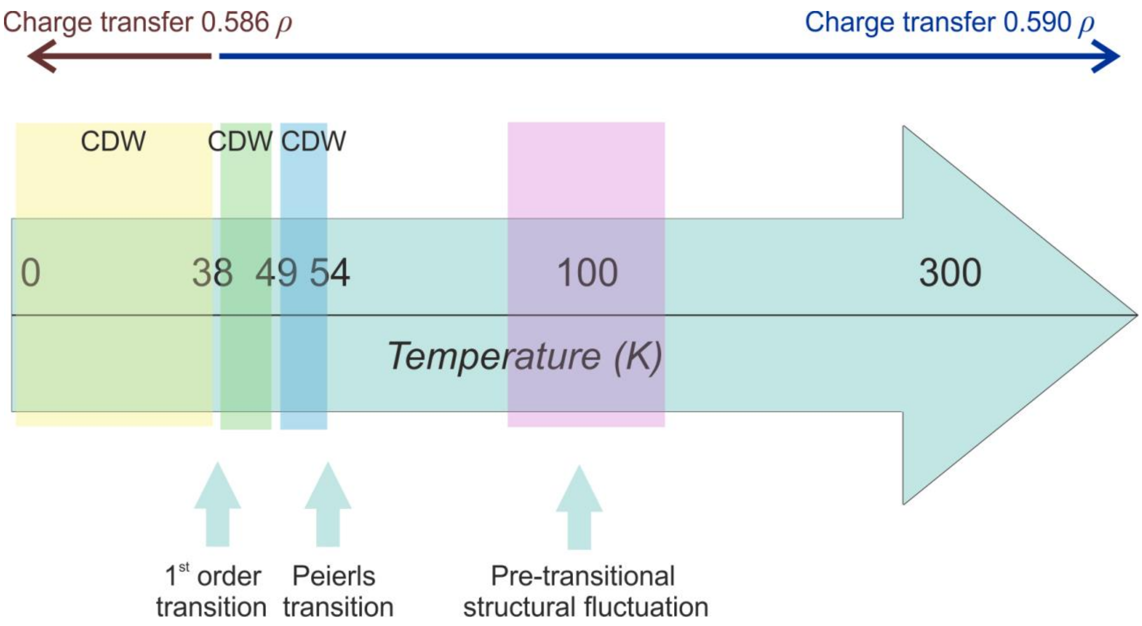

Figure 5.2. Schematic representation of the temperature dependence of phase transitions occurring in TTF-TCNQ at ambient pressure (after [33], [37], [125], [1], [128], [129], [130]).

Despite extensive work on structural and physical properties of TTF-TCNQ [124], [1], [128], [129] there are relatively few studies including ARPES [127], XPS [134], NEXAFS [87] and XANES [88], [94] spectrocopies. This is mainly due to the difficulty obtaining reliable data because of experimental problems with the surface preparation [135]. In this respect, the direct method to experimentally investigate the charge distribution and, specifically, the unoccupied electronic states, is NEXAFS [84]. NEXAFS is a powerful technique for the study of organic systems not only by its direct access to the unoccupied density of states but also by its ability to create relatively low radiation damage. Typically, all measurements are carried out in the soft X-ray regime below 2 keV. Several NEXAFS studies on TTF-TCNQ crystals [87] and thin films [88], [94] were performed and a first-principles analysis was carried out [88]. The N *K*-edge was chosen with the purpose to detect the redistribution of charge on the acceptor molecule because the four nitrogen atoms per chemical unit are located in the TCNQ molecule. It is generally accepted [88] that the N *K*-edge spectrum of TTF-TCNQ consists of 5 distinguishable peaks which belong to transitions in the aromatic ring and cyano groups of TCNQ. Regardless of this assertion, the peak which refers to the $\sigma^*(\pi(a_g, b_{3u}))$ transition in the cyano groups is missing in all experimental NEXAFS studies presented so far [87], [88], [94]. It could be concluded that up to now NEXAFS limitations in the study of the real electronic structure of TTF-TCNQ or of its modification at the low temperature phase transitions might be due to the quality of the single crystals or due to some experimental limitations.

5.2. Sample preparation

TTF-TCNQ single crystals were of the same batches as those used in the structural studies of Refs. [125], [130], [37]. High quality, untwinned crystals of typical size 3 x 0.8 x 0.3 mm^3 (along the *b* (1D), *a* and *c** directions, respectively) were used. Two single crystals of different branches have been measured and identical results have been obtained for all the measurements. The samples were carefully handled at ambient pressure. NEXAFS measurements were performed at the synchrotron light source ANKA (Karlsruhe, Germany) at the WERA end station. The resolution in the present measurements was better than 200 meV FWHM. The electron emission yield originates from a subsequent Auger process that neutralizes the core hole and leads to the emission of Auger electrons and, in turn, slow secondary electrons. The probing depth in the present experiments corresponds to approximately 10-15 molecular layers, which is sufficient for yielding information on the bulk of TTF-TCNQ crystals as well. The beam size was 0.8 mm x 0.2 mm. Spectra were recorded by a software developed at the WERA end station. The minimum temperature which can be achieved is about 20 K. The current investigation involved NEXAFS measurements performed at room temperature with further cooling down to 50 K. Radiation damage was excluded because all spectra were re-measured several times at different positions on the sample and showed identical results.

The monochromatized synchrotron radiation used has a high degree of linear polarization, and the polarization vector effectively lies within the sample surface. The nitrogen 2p orbitals relevant for the absorption process in N *K*-edge NEXAFS are present in different orientations already within the TCNQ molecule. Furthermore, the TCNQ building blocks are tilted within the TTF-TCNQ stacks that form the single crystal. So, no significant photon-polarization dependence could be expected in the spectra.

5.3. Temperature-dependent near-edge X-ray adsorption fine structure investigation

After the publication of the contents of this chapter in [86] the evaluation of the novel charge-transfer systems DTBDT - TCNQ and DTBDT-F_4TCNQ was performed using a different theoretical approach. These new results suggest a new interpretation of the NEXAFS signals of TCNQ, see Chapter 6. However, the present results for the spin-Peierls transition investigation are consistent within the used peak assignment and previously published works [87], [88], [94]. Therefore, this chapter uses the peak assignment originating from the theory of our coauthors J. P. Pouget and E. Canadell (presented in detail e.g. in [88]). The new calculation approach proposed in the context of the DTBDT-TCNQ system originates from the calculation with our colleagues in Frankfurt, R. Valentí et al.

The validity of the signal assignment for all TCNQ compounds cannot be finally proven in this Thesis. Therefore, a change to the new assignment without further experimental systematic work too speculative. Hence, the present chapter on TTF-TCNQ uses the same assignment as the published paper [86].

NEXAFS data obtained in the previous studies [87], [88], [94] show four distinguishable peaks for the nitrogen *K*-edge of TTF-TCNQ single crystals above the LUMO band after the fitting routine. Nitrogen atoms are present in the cyano groups of the TCNQ acceptor molecule only and hence their edge structure is a fingerprint of the acceptor.

In Fig. 5.3 and 5.4 NEXAFS measurements of the TTF-TCNQ compound are shown. The spectral features (peaks **1**-**5**, where peak **2** is visible for the first time) were quantitatively analyzed by a multipeak fit routine with a mixed Gaussian/Lorentzian function. The spectra were taken as function of temperature. The purpose of the measurements at different temperatures was to compare the TCNQ contribution to the electronic structure of TTF-TCNQ and to detect a possible spectroscopic signature of the 54 K phase transition which is related to the Peierls transition on the TCNQ stack. The partial spectra yielded by the fit are represented as thin lines and circles denote the measured data. In all spectra the sum of fit curves perfectly reproduces the experimental results. The designation of the partial peaks was used in the following order in comparison to theoretically predicted N *K*-edge spectra from [88] (see also Fig. 5.3)[3]. Signal **1** is a π*-type resonance and originates from the lowest empty a_u and b_{1u} orbitals. These orbitals are concentrated on the aromatic ring of the TCNQ molecule. Transitions which belong to signal **1** are denoted as $N_{1s} \rightarrow a_u,b_{1u}$ (π*-ring). Signal **2** originates from unoccupied orbitals located in the cyano groups: $N_{1s} \rightarrow a_g,b_{3u}$ (σ*(π) cyano). It is an antibonding orbital which is symmetrical with respect to the molecular plane and lower in energy than (π*(π)) [the labelling follows that used in previous works [87], [88], [94]: the first label indicates if the empty antibonding orbital is symmetric (σ*) or antisymmetric (π*) with respect to the molecular plane; the second label indicates whatever is the symmetry if such molecular orbital is made of locally π-type orbitals of the cyano groups]. Signal **3** is a resonance of σ*-type and is based on b_{1g} and b_{2u} orbitals. Signal **3** associates with $N_{1s} \rightarrow b_{1g},b_{2u}$ (σ*(π) cyano) transitions. Signal **4** originates from the b_{3g} and a_u orbitals and is indicated as **4**: $N_{1s} \rightarrow b_{3g},a_u$ (π* cyano). Signal **5** corresponds to the highest π*-type orbital of benzene (b_{2g}) that is delocalized over the whole TCNQ molecule, $N_{1s} \rightarrow b_{2g}$ (π* ring). The first peak appears at 2.8 eV above the LUMO level, signal **2** is found at 3.5 eV, signals **3** and **4** are situated between 4.5 and 4.8 eV, and finally peak **5** is at 5.6 eV. These energy separations are in excellent accord with the DFT values for the energies of the corresponding pairs of orbitals with respect to the energy of the LUMO in isolated TCNQ: 2.55/2.65 eV for a_u/b_{1u}, 3.51-3.63 eV for a_g/b_{3u}, 4.55-4.66 eV for b_{3g}/a_u, 4.77-4.86 eV for b_{1g}/b_{2u} and 5.46 eV for b_{2g} [88]. The two pairs a_g/b_{3u} and b_{3g}/a_u are very near in energy for the isolated molecule. In the present measurements the two pairs of levels are still found at very similar energies although the order seems to be reversed with respect to the isolated molecule. In summary, the unoccupied states involved in the weaker transitions **1** and **5** are essentially delocalized on the benzene ring, whereas states involved in transitions **2**, **3**, and **4** derive from the cyano groups (**2** and **3** from the σ*(π) orbitals and **4** from the π* orbitals).

---

[3] The DFT calculations were performed by Prof. Dr. Enric Canadell (ICMAB-CSIC, Spain). It should be noted that later calculations by Prof. Dr. Roser Valentí (University of Frankfurt (M)) yielded another approach and peak assignment, see Chapters 5.3 and 6.

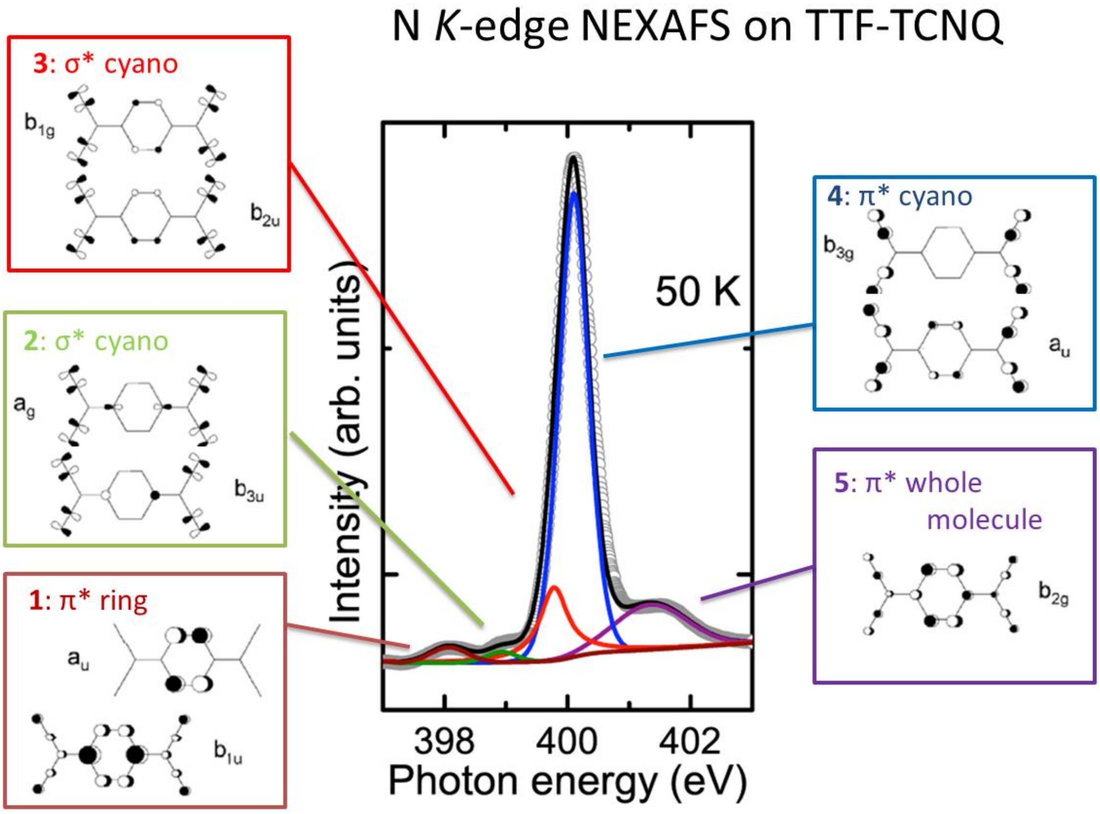

Figure 5.3. Nitrogen *K*-edge NEXAFS spectrum of TTF-TCNQ at 50 K and assignment of the experimentally-observed signals with calculated orbitals (schematic) adopting the peak assignment of [88].

So far no study has been able to detect the presence of the $\sigma^*(\pi(a_g,b_{3u}))$ transition located at the CN-groups that is shown as signal **2** in Figs. 5.3 and 5.4. This was attributed to the better quality of the crystals used in the present study. The contribution of the unoccupied orbital $\sigma^*(\pi(a_g,b_{3u}))$ of the cyano groups (signal **2** in Fig. 5.3 and 5.4) is clearly visible in our experiment for the first time. That allows us to discuss in detail the nature of the TCNQ empty orbitals of TTF-TCNQ and their behavior along the Peierls transition.

The system, being an electronically low-dimensional molecular solid, does not show the same degree of broadening effects as, for instance, the oxygen *K*-edge does in an oxide. The presence of the core hole will sharpen up the spectral form again, as screening is probably not very strong, and will shift excitation energies to a certain extent, as shown and discussed in [88].

The intensity variations for signals **1**, **2**, **3**, and **4** were quantified from N *K*-edge spectra. The temperature dependence of the intensity variation is shown in Fig. 5.5. The intensities are determined as areas under the corresponding fitted peaks in the spectra shown in Fig. 5.5, normalized to the area under signal **5** which showed no significant changes with varying temperature and thus was assumed to stay constant in intensity. In order to compare the changes in the relative intensities on the same scale, all four curves are scaled to the value of 1 at 100 K. The intensity of signals **2**, **3**, and **4** varies sizably with temperature in contrast to the intensity of signal **1**.

When cooling TTF-TCNQ from 100 K down to 80 K, there are significant changes in intensities of all three orbitals of the cyano groups: $\sigma^*(\pi(a_g,\ b_{3u}))$, $\pi^*(\pi(b_{3g},a_u))$ and $\sigma^*(\pi(b_{1g},b_{2u}))$. This is a clear signature of changes in the electronic structure that mast likely are caused by local fluctuating pre-transitional structural distortions on the TCNQ stacks, which, in particular, involve an out-of-plane intramolecular deformation of TCNQ [132]. Upon further cooling of the crystals to below 60 K, one observes an increase of the $\pi^*(\pi(b_{3g},a_u))$ intensity value of the cyano groups. This is a fingerprint of the onset of the upper Peierls transition which develops a true Peierls gap on the TCNQ stacks. At this transition the electronic and structural CDW modulations of the TCNQ stack are frozen and different unoccupied states should appear above the Peierls gap. Such a redistribution of the unoccupied electronic states could be caused by a substantial displacement of the quinoid ring with respect to the cyano groups in a direction perpendicular to the TCNQ plane, which leads to a “boat-like” deformation of the acceptors, as experimentally found by Bouveret and Megtert [130].

Since the transferred electrons fill the LUMO of TCNQ, which is a π-type orbital strongly based on the central six-member ring, it can be expected that when an electron is excited from a core level to one of the low-lying levels of TCNQ, it will feel this extra charge which slightly increases when the temperature decreases, and will tend to localize around the cyano groups. This would lead to an increase of the resonance peak intensity associated with signals **2**, **3**, and **4**. However, this is not the case as shown in Fig. 5.5, as intensities of peaks **3** and **4** increase, the intensity of signal **2** decreases. In addition, the charge-transfer increase when the temperature decreases is not dramatic. Clearly, the two distinctive features of Fig. 5.5: (i) opposite variations of the resonance peak intensities with temperature, and (ii) clear intensity jump of signal **4** around the upper Peierls transition, cannot be explained on the basis of the variation of a charge transfer alone.

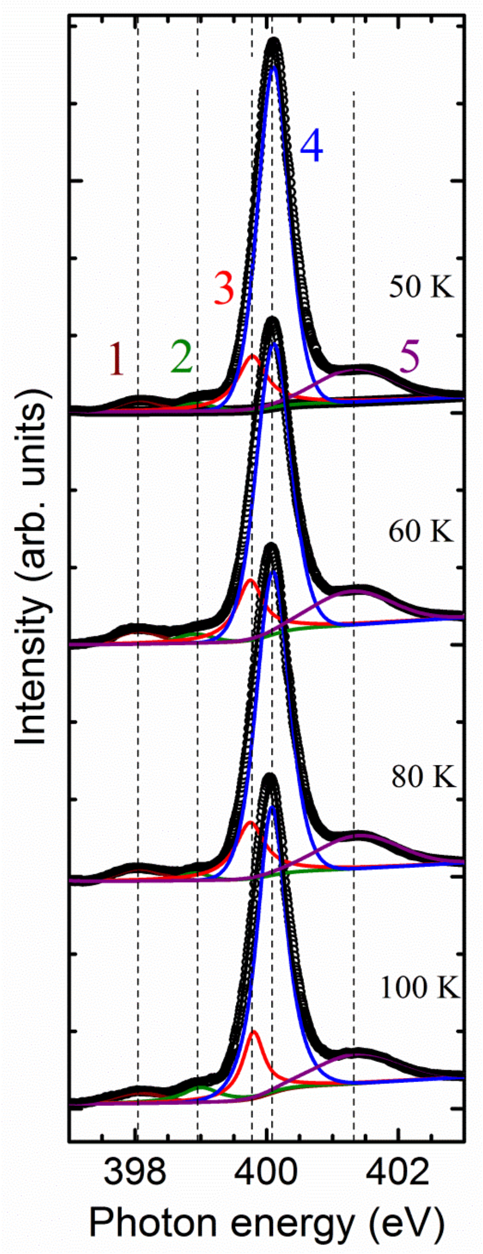

Figure 5.4. Nitrogen *K*-edge NEXAFS spectra of the TTF-TCNQ crystal at different temperatures. Spectra are scaled to have equal areas under peak 5. Circles denote the experimental data and thin curves mark the partial spectra obtained by a multipeak deconvolution of the experimental spectra. The vertical dashed lines mark the positions of the peak maxima.

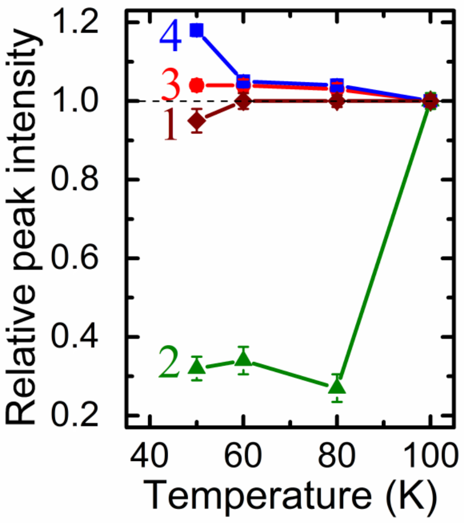

Figure 5.5. Temperature dependence of the NEXAFS resonance peak intensities in the nitrogen K-edge spectra of TTF-TCNQ. Intensities are taken from integrals of the fitted partial spectra in Fig. 5.5 and are first normalized to the area of peak 5. These relative peak intensities are then scaled to 1 at 100 K for sake of direct comparison of the trends. The error bars or size of the symbols denote the error in the determination of the integrals.

5.4. Pyramidalization of TCNQ

The results in Fig. 5.5 can be understood on the basis of (i) the nature of the molecular orbitals implicated in each peak (see Fig. 5.3), and (ii) the nature of the intramolecular deformation of the TCNQ molecule when the modulation develops [130]. The more important feature of such a deformation is an important pyramidalization at C_α (see Figs. 5.6 and 5.3 for labelling). The three pairs of empty molecular orbitals associated with peaks **2**, **3** and **4** are essentially π–type cyano levels (both in-plane and out-of-plane) which slightly delocalize towards the central six-member ring in the planar geometry of TCNQ. When the pyramidalization of C_α occurs, such delocalization is strongly hindered and the molecular orbitals tend to concentrate on the cyano groups. Thus increases the intensity of the resonance peak because the overlap integral with the localized N 1s initial state orbital of the NEXAFS transition increases. However, one should expect a different behavior for the three pairs of orbitals responsible for peaks **2**, **3** and **4** because of their different symmetry properties. The pair $\sigma^*(\pi(a_g,b_{3u}))$ is symmetric with respect to a plane going along the long axis of the molecule and perpendicular to the molecular plane, whereas the pairs $\pi^*(\pi(b_{3g},a_u))$ and $\sigma^*(\pi(b_{1g},b_{2u}))$ are antisymmetric. The latter two differ in the symmetry with respect to the molecular plane: whereas $\sigma^*(\pi(b_{1g},b_{2u}))$ is symmetric, $\pi^*(\pi(b_{3g},a_u))$ is antisymmetric. The type of orbitals of the C_α-C_β connecting group between the cyano substituents and the central part of the ring that can mix into the three pairs of orbitals are: none into $\pi^*(\pi(b_{3g},a_u))$, carbon p_y into $\sigma^*(\pi(b_{1g},b_{2u}))$ and both carbon s and p_x into $\sigma^*(\pi(a_g,b_{3u}))$. This means that the interaction between the two subsystems is through π-type interactions for pairs $\pi^*(\pi(b_{3g},a_u))$ and $\sigma^*(\pi(b_{1g},b_{2u}))$ but through σ-type interactions for pair $\sigma^*(\pi(a_g,b_{3u}))$. In other words, the interaction is stronger and more robust towards geometrical changes such as pyramidalization in C_α for the pair $\sigma^*(\pi(a_g,b_{3u}))$.

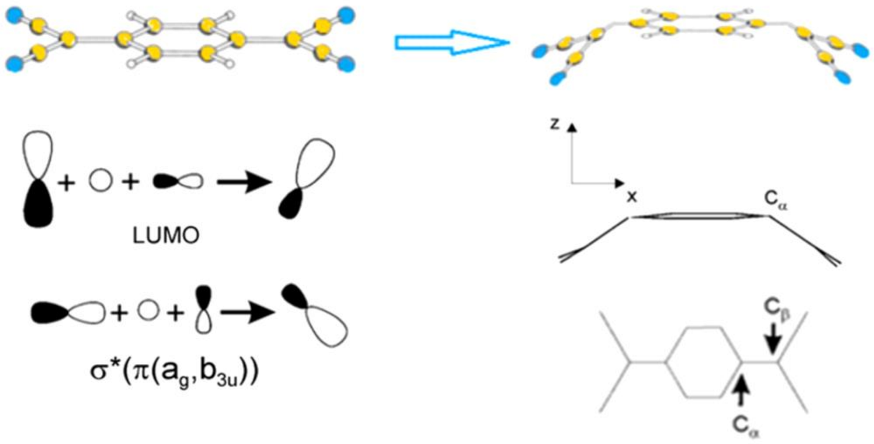

Figure 5.6. Schematic illustration of the pyramidalization-induced orbital mixing at C_α for the LUMO and the $\sigma^*(\pi(a_g,b_{3u}))$ pair in TCNQ molecule.

The delocalization towards the central part in the case of both $\pi^*(\pi(b_{3g},a_u))$ and $\sigma^*(\pi(b_{1g},b_{2u}))$ pairs is of π–type and consequently depends on the degree of pyramidalization in C_α in a more complicated. However, since the cyano orbitals of $\sigma^*(\pi(b_{1g},b_{2u}))$ lie on the original molecular plane (i.e. they belong to the σ electronic skeleton of the molecule) whereas for those of $\pi^*(\pi(b_{3g},a_u))$ the original molecular plane is a nodal plane, the effect of the pyramidalization should be stronger for the last pair. So, for both $\pi^*(\pi(b_{3g},a_u))$ and $\sigma^*(\pi(b_{1g},b_{2u}))$ pairs one should expect a decrease in the delocalization from the cyano orbitals and thus an increase in the participation of the nitrogen orbitals. Consequently, the resonance peak intensity associated with signals **3** and **4** should increase when the temperature decreases. This is in agreement with the data in Fig. 5.5. The situation is different for the pair $\sigma^*(\pi(a_g,b_{3u}))$. The key difference with

$\sigma^*(\pi(b_{1g},b_{2u}))$ is that by being symmetric with respect to the vertical plane along the long molecular axis, it allows the participation of both the C_α *s* and p_x orbitals. When the pyramidalization in C_α occurs, these two orbitals mix with the C_α p_z orbital (see Fig. 5.6), which initially was of different symmetry. The weight of the C_α contributions in these molecular orbitals increases at the expense of those of the cyano groups. In other words, these empty orbitals, which are symmetric with respect to the vertical plane along the long molecular axis, provide a channel for the delocalization of σ charge towards the central part of the molecule when pyramidalization occurs. Physically, such a shift is the answer of the system to the electron reorganization occurring in the LUMO which redirects part of the σ electron density around C_α outside the molecular plane (see Fig. 5.6). As follows, the pyramidalization leads to a decrease in the participation of the cyano and thus the nitrogen orbitals, and consequently leads to a loss of resonance peak intensity associated with signal **2.** The opposite effect of the pyramidalization on the two pairs $\sigma^*(\pi(b_{1g},b_{2u}))$ and $\sigma^*(\pi(a_g,b_{3u}))$ cannot be explained in terms of changes in the electron transfer. Since the $\sigma^*(\pi(a_g,b_{3u}))$ pair is symmetric with respect to the vertical plane along the long molecular axis, the mixing induced by the pyramidalization is more effective and so, the variation in peak intensity of **2** is larger than of signal **3** which is associated with antisymmetric orbitals.

5.5. Signature of the Peierls transition

The second distinctive feature of Fig. 5.5 is the sudden increase in the peak intensity of signal **4** around the upper Peierls transition. So far the origin of this transition has been discussed on the basis of the $2k_F$ wave vector instability of the partially filled TCNQ LUMO band, however, a local description relying on the chemical bonding is still lacking. The LUMO is a π-type orbital with a strong participation of the p_z orbital of C_α. Consequently, when pyramidalization at C_α occurs, the *s* and p_x orbitals of the carbon atom mix as sketched in Fig. 5.6 and the p_z contribution becomes a “pseudo-sp^3 hybrid” well directed to interact with a similar orbital of the nearest TCNQ. However, the charge transfer per TCNQ (≈ 0.59), is far from the two electrons required to establish a full C-C σ bond. Therefore, in order to minimize the elastic energy cost, the system chooses to modulate the TCNQ internal distortion so that the maximum stabilization occurs when the pyramidalization in adjacent TCNQs along the stacks develops in opposite directions [130] and decreases otherwise. In short, the stack distortion can be described as a series of C_{α} --- C_{α} interactions modulated along *b*. It is then understandable that when the 1D CDW fluctuations associated with such a bond modulation become 3D ordered below 60 K, the peak intensity of signal **4**, which is associated with a pair of π-type orbitals (as is the LUMO), exhibits a sudden increase denoting an almost complete localization of this pair of orbitals in the cyano groups.

5.6. Summary

In conclusion, the structure of unoccupied electronic states of TTF-TCNQ single crystals was experimentally determined using NEXAFS and compared to DFT calculations. The experimental spectra of the nitrogen *K*-edge fine structures at different temperatures contain all the orbitals predicted by theory. The orbitals located in the cyano groups $\sigma^*(\pi(a_g,b_{3u}))$ were clearly observed for the first time in the present experiment. Both the influence of the charge transfer and the structural deformation of TCNQ can explain the evolution with temperature of two of the three pairs of empty orbitals probed. However, only the structural effects provide a simple explanation for the opposite behavior of the two pairs of orbitals associated with the σ skeleton of the TCNQ molecule. The evolution of all these orbitals and more particularly, that of the $\pi^*(\pi(b_{3g},a_u))$ pair, provide a clear fingerprint of the upper Peierls transition of TTF-TCNQ.

Concluding, the discussion presented here and published in [86] is consistent and explains the structure-induced changes at the Peierls transition in a convincing way. However, this argument does not falsify the new assignment proposed in the context of the DTBDT complex. More systematics is needed to shed more light into the question of the orbital assignment of the TCNQ NEXAFS signals.

6. Microscopic origin of the charge transfer in crystals based on thiophene derivatives

6.1. Thiophene based materials: state of the art

Novel charge-transfer (CT) compounds based on low-dimensional organic materials with π-conjugated rings decorated with different ligands offer a huge potential for variability and unconventional behavior in materials research. The design of new organic molecules and their combinations provide compounds with unusual properties like superconductivity, magnetism, spin density waves or charge density waves [136]. Many of the organic conductors and superconductors are based on the bis(ethylenedithio)tetrathiafulvalene (BEDT-TTF) donor and various acceptors. Furthermore, polycyano derivatives have mainly been used as acceptors like tetracyanoquinodimethane (TCNQ) [25], [136]. A few examples of CT complexes have been intensively investigated in the past focusing mainly on the electronic structure [16], [137], [138], [139]. Such systems are very promising in potential applications in organic electronics and solar cell systems [140]. For instance, P-type organic semiconductors are indispensable for diodes and complementary circuits with a high operation speed and low power consumption and which are widely represented by oligo- and poly-thiophenes [141]. The interest on such building blocks for complex electronic systems is due to the high polarizability of the sulfur atoms in thiophenes leading to a stabilization of the whole molecular system and excellent charge carrier transport [142]. Furthermore, a possible tuning of electronic properties can be achieved by varying the structural particularities. CT complexes based on thiophenes are also interesting from the fundamental research perspective as model systems with new electronic states in comparison to pure donor and acceptor phases.

Recently, a new class of donors represented by derivatives of the compound dithieno[2,3-d;2’,3’-d’]benzo[1,2- b;4,5-b’]dithiophene, abbreviated as DTBDT (Fig. 6.1) was synthesized [143]. Based on this precursor with alkyl groups, thin films of the CT mixture DTBDT-F_4TCNQ have been obtained by molecular beam epitaxy in ultrahigh vacuum and characterized by scanning tunneling microscopy [144].

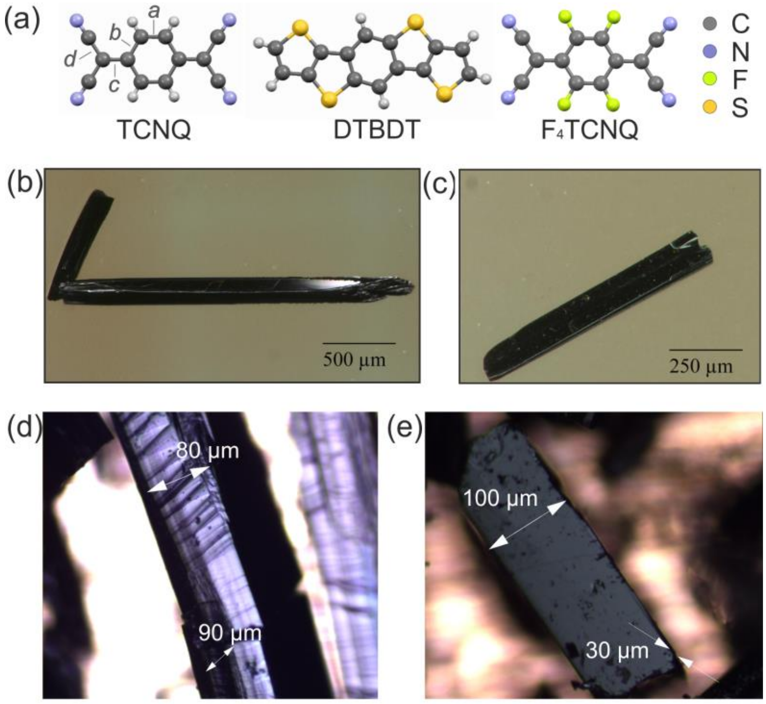

Figure 6.1. (a) Molecular structures of the thiophene based donor DTBDT and acceptors TCNQ and F_4TCNQ. Bond lengths a, b, c, and d are shown for the TCNQ molecule that directly correlate with the charge transfer in the complex (see text); (b) needle-shaped crystals of DTBDT-TCNQ and (c) DTBDT-F_4TCNQ, grown by gas-phase crystallization; orientation of (d) DTBDT-TCNQ and (e) DTBDT-F_4TCNQ crystals with marked dimensions during NEXAFS measurements.

As it has been shown in a few studies on organic complexes [86], [87], [89], [145], [146], [147] NEXAFS spectroscopy [84] is a powerful method for investigating the orbital-resolved charge transfer process. Furthermore, this method is not surface-sensitive and not destructive. The rather large probing depth of 3-5 nm and instrumental resolution around 30 meV allows to follow the change in occupancy of molecular orbitals and therefore facilitates a very precise analysis of the electronic structure in an orbital selective manner [89]. However, currently all NEXAFS data on organic compounds have been analyzed in terms of plain DFT calculations, neglecting the effects of the core hole, that up to now could only be considered in a single particle model. Triggered by the experimental results on thiophene based complexes, our collaborators from the theory group of Prof. Dr. Roser Valentí (University of Frankfurt (M)) have tried several theoretical models to find the best one to describe experimental NEXAFS data.

The NEXAFS results shown in the following were obtained for gas-phase crystallized molecular crystals of the CT phases of donor DTBDT in combination with two acceptors of different strength: TCNQ and F_4TCNQ (see Fig. 6.1). The discussion of charge transfer complex formation is based on a quantitative comparison of the measurements and DFT [148], [99] calculations. Since NEXAFS measurements give direct access to the unoccupied electronic states of the material, it is possible to compare and discuss even subtle changes and differences in the electronic structure during the charge transfer complex formation.

6.2. Sample preparation and experimental details

The DTBDT donor molecules were synthesized[4] as described in [143]. Acceptor molecules TCNQ and F_4TCNQ were commercially available (Fisher Scientific, TCI).

Single crystals of the CT compounds were grown by physical vapor transport[5] [149], [150]. The starting materials, 6 mg of DTBDT and 8 mg of TCNQ or F_4TCNQ, were ground together and transferred into a glass ampoule, which was cleaned by ethanol and acetone and baked in a box furnace for at least 24 hours to remove water. The glass ampoule was evacuated ($p \approx 10^{-3}$ mbar), sealed and placed into a horizontal oven with a temperature gradient. The source material was positioned at the hottest zone at around 225° C. Dark, needle-shaped CT crystals form at 190-200° C. The growth procedure lasted ≈50 hours and the ampoule was removed from the hot oven after the starting material

---

[4] In the research group of Prof. Dr. Martin Baumgarten (Max-Planck Institute for Polymer Research, Mainz).

[5] Charge transfer crystals of DTBDT-TCNQ and DTBDT-F_4TCNQ were grown by Antonia Morherr in the group of Prof. Dr. Cornelius Krellner (University of Frankfurt am Main).

was completely sublimated. The ampoule was opened and the dark needles were collected from the walls. The structure of the single crystals was determined by X-ray diffraction[6]. Results of the crystal structure of DTBDT-TCNQ and DTBDT-F_4TCNQ are presented in Fig. 6.2 and in Table 6.1.

Infrared spectroscopy was carried out on polycrystalline samples of DTBDT-TCNQ and DTBDT-F_4TCNQ and compared to spectra recorded from powders of pure acceptors TCNQ and F_4TCNQ, respectively. Spectra were obtained using a Nicolet 730 FT-IR spectrometer between 4000 and 500 cm^{-1} at room temperature[7]. Resolution of the measurements was 1 cm^{-1}.

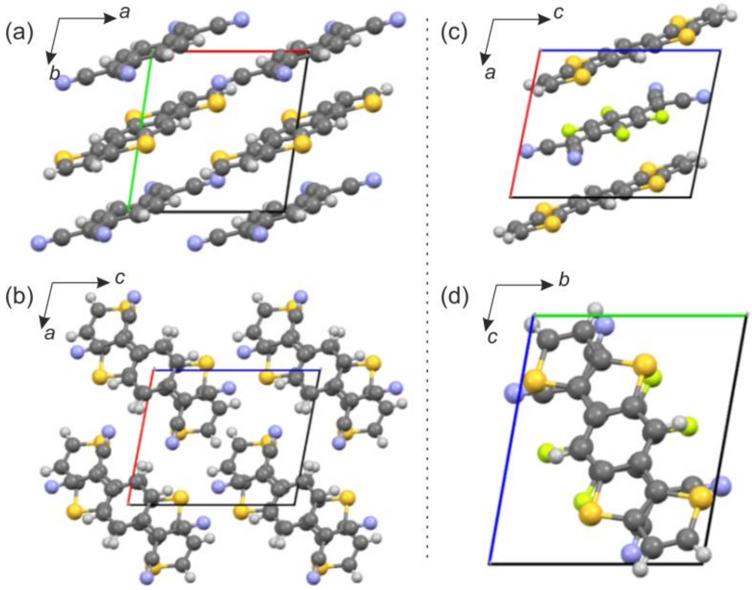

Figure 6.2. Overview of the crystal structures of DTBDT-TCNQ (left) and DTBDT-F_4TCNQ (right). DTBDT-TCNQ: (a) mixed stack in b direction; (b) view along the b axis. DTBDT-F_4TCNQ: (c) mixed stack in a-direction; (d) view along the a-axis.

The current-voltage (I-V) measurements of DBTDT-TCNQ and DTBDT-F_4TCNQ were performed with a Keithley 6517A electrometer using a two-point contact method[8]. The contacts were prepared with graphite paste. A four-point measurement was not necessary, because the contact resistance was negligible in comparison to the high resistivity of the crystals. The distance between the two contacts was 870 µm for DTBDT-

---

[6] Structural analysis was performed by Dr. Michael Bolte (University of Frankfurt am Main).

[7] The IR spectrometer for the study was kindly provided by Max-Planck Institute for Polymer Research, Mainz.

[8] Transport measurements were performed by Antonia Morherr in the group of Prof. Dr. Cornellius Krellner (University of Frankfurt am Main) and are shown here to make a complete picture of properties of the novel materials.

TCNQ and 370 µm for DTBDT-F_4TCNQ (width of both crystals was 190 µm, and thickness 80 µm for DTBDT-TCNQ and 55 µm for DTBDT-F_4TCNQ). With this setup, it was possible to measure currents down to 0.1 nA at an applied voltage of up to 500 V. Temperature dependent measurements were performed in a Leybold cryogenerator RD 891 with a LTC 60 temperature controller. The current was measured at 100 V for different temperatures down to 200 K. Below this temperature the current was less than 0.1 nA and run into the background noise.

Single crystals of DTBDT-TCNQ and DTBDT-F_4TCNQ were oriented with a Bruker D-8 diffractometer. DTBDT-TCNQ was contacted in the (011)-plane and DTBDT-F_4TCNQ in the (010)-plane. Room temperature I-V curves of both crystals showed a typical Ohmic behavior with resistances of 4.3 GΩ (DTBDT-TCNQ) and 0.9GΩ (DTBDT-F_4TCNQ). Given crystal dimensions resulted in a resistivity of 75000 Ωm for DTBDT-TCNQ and 11000 Ωm for DTBDT-F_4TCNQ.

Table 6.1. Crystallographic data for DTBDT-TCNQ and DTBDT-F_4TCNQ crystals.

Crystal data	DTBDT-TCNQ	DTBDT-F_4TCNQ
Chemical formula	$C_{26}H_{10}N_4S_4$	$C_{26}H_6F_4N_4S_4$
Formula weight	506.66	578.59
Crystal system	Triclinic	Triclinic
Space group	P -1	P -1
Unit cell dimensions	a=7.5227(3) Å	a=7.7585(15) Å
	b=7.8873(3) Å	b=7.8305(13) Å
	c=9.2504(5) Å	c=9.4063(18) Å
	α=101.503(3)°	α=99.027(14)°
	β=99.140(2)°	β=100.553(15)°
	γ=96.410(3)°	γ=94.654(15)°
Volume	525.15(4) Å^3	551.27(2) Å^3
Z	1	1
Crystal size (mm)	0.080 x 0.110 x 0.420	0.410 x 0.080 x 0.040

The NEXAFS measurements were performed at the soft X-ray beamline I1011 at MAX II, Lund (Sweden), at an energy resolution of 120 meV and 200 meV for N 1s and F 1s, respectively , where the drain current from the sample was recorded. The total electron yield originated from a subsequent Auger process that neutralizes the core hole and led to the emission of Auger electrons which in a secondary process were transformed into slow secondary electrons. The information depth was about 5 nm, corresponding to approximately 15 molecular layers, which was sufficient for yielding information on the bulk of the crystallites. Because the charge transfer process mainly alters the unoccupied states of the acceptor, the nitrogen and fluorine K-edge spectra were investigated which are specific to the acceptor orbitals. Spectra from the mixed phase crystals with DTBDT donor molecules were compared to spectra of the pure acceptor moieties. All measurements were performed for powders of the pure acceptor and donor molecules and for a large number of mixed-phase crystals glued to a copper sample holder at room temperature in random orientation.

Based on the experimentally determined crystal structures of TCNQ [151], F_4TCNQ [152], DTBDT-TCNQ and DTBDT-F_4TCNQ, ab-initio calculations were performed[9] using a number of quantum chemistry and density functional theory codes. Molecular calculations were performed with ORCA [153] using the B3LYP hybrid exchange correlation functional with Becke with 20% Hartree-Fock exchange. For the analysis of the NEXAFS spectra of TCNQ and F_4TCNQ, the full-potential linearized augmented plane-wave basis (FLAPW) was used as implemented in the Wien2k package [109]. NEXAFS spectra were calculated using the XSPEC program [154], [155] integrated into Wien2k using integer and fractional core holes [156]. The generalized gradient approximation in the Perdew, Burke, Ernzerhof (PBE) form [102] was used. Finally, calculations for all compounds discussed in this work were performed using the full potential local orbital (FPLO) basis set [110] and the PBE exchange-correlation functional [102]. The self-consistent charge density allowed extracting the charge transfer as determined from the excess charge on TCNQ or F_4TCNQ. A k-mesh of at least 10 x 10 x 10 points was used to converge the electronic structures of all compounds. Convergence of half core hole spectra was checked using 24 x 24 x 24 k meshes.

---

[9] Theoretical calculations were performed in the research group of Prof. Dr. Roser Valentí (University of Frankfurt am Main).

6.3. Charge transfer in DTBDT-TCNQ and DTBDT-F$_4$TCNQ

One of the most important characteristics of CT complexes is the amount of charge transfer. In the following the charge transfer deduced from the structural arrangement of donor and acceptor molecules is compared with theoretical calculation and experimental vibration spectra.

As it was shown in [157], the increasing charge in the TCNQ molecule causes a shortening of the bond length, the authors attribute this to an aromatization of the molecular structure. The same approach has been shown to be applicable for the F$_4$TCNQ structure due to similar bond length change with increasing charge transfer amount [149], [158]. Accordingly, the CT can be calculated by the following equation:

$$\rho = \frac{\alpha_{CT}-\alpha_0}{\alpha_1-\alpha_0}, \qquad (6.1)$$

where the parameter $\alpha = c/(b+d)$ denotes the relative bond length, calculated from the molecular structure as shown in Fig. 6.1. The indices CT, 0 and 1 indicate the charge transfer complex, the neutral acceptor molecule and the acceptor anion (where ρ=1), respectively. The determination of CT with equation (6.1) was performed using values of bond lengths for complexes from the present structural investigation, α_0(TCNQ) from [151], α_1(TCNQ) from [159], α_0(F$_4$TCNQ) from [152] and α_1(F$_4$TCNQ) from [160]. The estimated values were found to be 0.04 *e* for DTBDT-TCNQ and 0.14 *e* for DTBDT-F$_4$TCNQ.

Infrared spectroscopy is a very convenient experimental technique for the estimation of the charge transfer due to the linear dependence between the frequency shift of the C≡N stretching mode and the transferred charge. The charge transfer was calculated using the following equation [161]:

$$\rho = \frac{2(\omega_0-\omega_{CT})}{\omega_0\cdot\left(1-\frac{\omega_1^2}{\omega_0^2}\right)}, \qquad (6.2)$$

where ω_0, ω_1 and ω_{CT} denote the frequency of the C≡N stretching mode for neutral acceptor, anion (where ρ=1) and the charge transfer salt, respectively. This equation has been previously applied to both TCNQ and F_4TCNQ acceptors, and other molecules [162], [149], [163] that will serve for comparison cases.

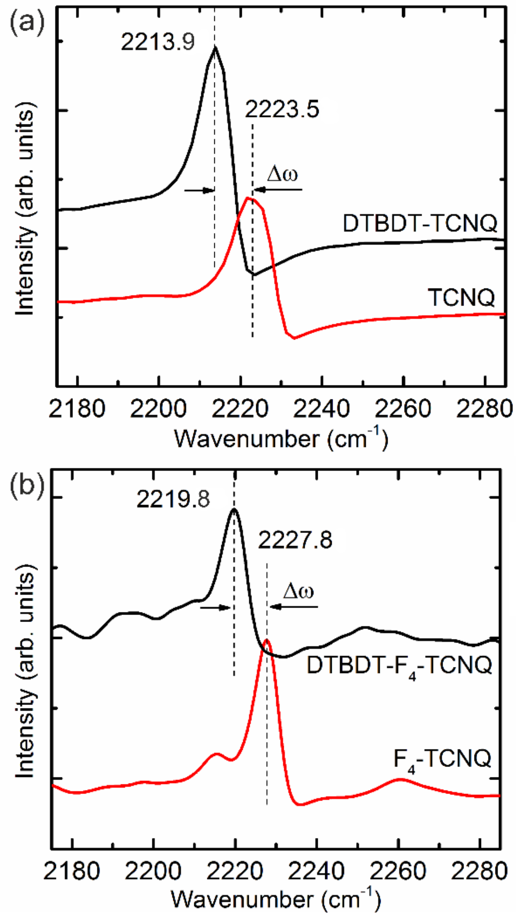

Figure 6.3. (a) IR spectra of the C≡N stretching vibration in TCNQ powder and crystals of the CT complex DTBDT-TCNQ; (b) same for F_4TCNQ and DTBDT-F_4TCNQ. Error of frequency determination: 0.4 cm^{-1}.

IR spectra of the C≡N stretching vibration were measured at room temperature for pure acceptor powders TCNQ and F_4TCNQ and for crystals of the mixed phases DTBDT-TCNQ and DTBDT-F_4TCNQ. In the mixed crystals of DTBDT-TCNQ (Fig. 6.3 (a)) the vibration frequency was red-shifted to ω_{CT} =2213.9 cm^{-1}, when ω_0 = 2223.5 cm^{-1} and ω_1 = 2183 cm^{-1} from [164]. Due to the asymmetric line shape, the estimated error of the frequency values to be 0.4 cm^{-1}. This is indicative of a CT on the order of 0.24±0.01 *e*, determined from equation (6.2). For the DTBDT-F_4TCNQ crystals the vibration frequencies were: ω_{CT} = 2219.8 cm^{-1}, ω_0 = 2227.8 cm^{-1} and ω_1 = 2190 cm^{-1} according to [165]. In this case the CT amount was calculated to be 0.21±0.01 *e* (Fig. 6.3, b). The charge transfer is usually proportional to the electron affinity E_A of the acceptor molecule (see eq. 2.6). Therefore, following this simple argument, one would expect a larger charge transfer in the case of the F_4TCNQ (E_A ≈5.2 eV) compared to the TCNQ (E_A ≈4.8 eV) based compound. In contrast, the IR-spectroscopy suggested the opposite effect, the charge transfer in DTBDT-F_4TCNQ is slightly smaller than in DTBDT-TCNQ. The same inverse dependence of the acceptor electron affinity and the charge transfer was observed by Rudloff et al. [139] on the systems TMP-TCNQ and TMP-F_4TCNQ.

The current-voltage characteristic and the temperature dependence of the current at 100 V are plotted for both crystals in Figs. 6.4 and 6.5. The conductivity decreases exponentially with decreasing temperature, shown by the Arrhenius plot for DTBDT-TCNQ (Fig. 6.4) and DTBDT-F_4TCNQ (Fig. 6.5). A fit of the eq. (6.3) to the data in the high-temperature regime gives a transport gap for DTBDT-TCNQ of 0.51±0.01 eV and for DTBDT-F_4TCNQ of 0.36±0.01 eV.

$$\sigma = Aexp(-\frac{\Delta E_{tr}}{k_B T}) \tag{6.3}$$

In Table 6.2 the experimental values of the charge transfer obtained from infrared spectroscopy and conductivity measurements are compared with theoretical values obtained from DFT [148], [99] electronic structure calculations by employing the FPLO [110] basis and the GGA exchange correlation functional [102]. The charge transfer ρ is obtained in terms of the calculated charges on the atoms. Comparison of the theoretical results with the IR-based estimates shows a reasonable agreement although the theoretical values follow the expectation of a larger charge transfer for stronger acceptor electron affinity in contrast to the experimental observation. Experimentally, the reversed order is at the limit of uncertainty (error ±0.01). This will be discussed in the next section. Table 6.2 also shows the calculated band gaps between the HOMO of the donor and the LUMO of the acceptor molecule that compare well with those extracted from electronic transport measurements.

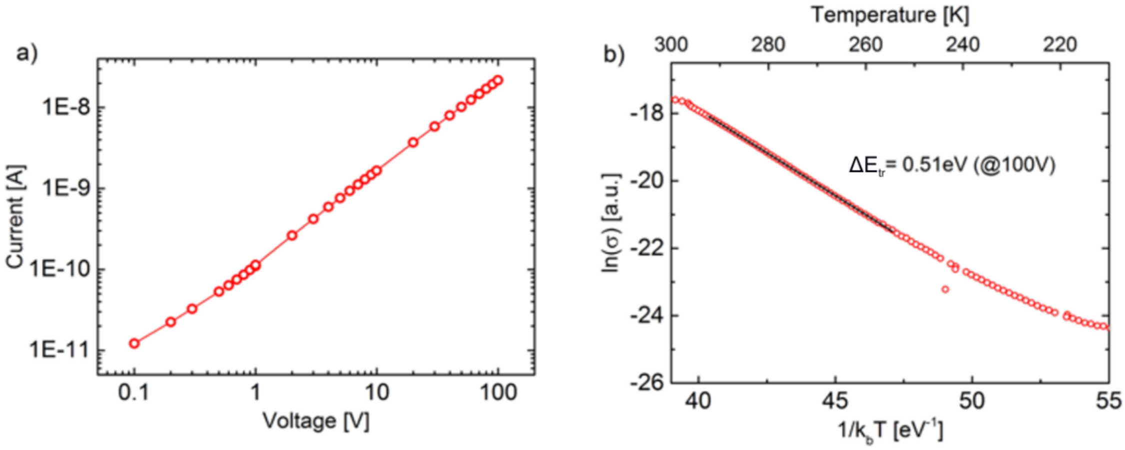

Figure 6.4. Electrical transport measurement for DTBDT-TCNQ crystal: (a) I-V-curve with a linear slope and a resistance of 4.3GΩ. (b) Conductivity versus the inverse temperature at 100 V. The linear slope yields a transport gap of 0.51 eV.

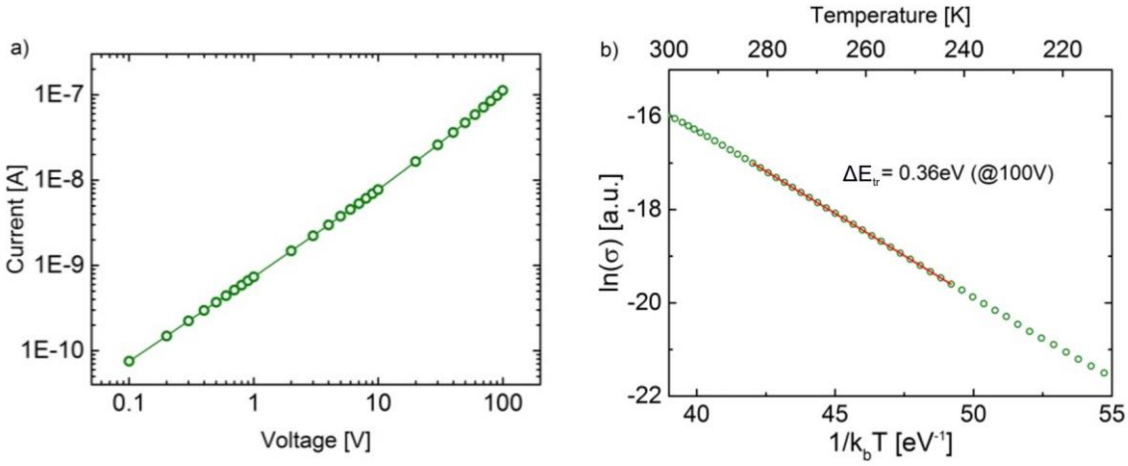

Figure 6.5. Same as Fig. 6.4, but for DTBDT-F_4TCNQ: here the I-V-curve yields a resistance of 0.9 GΩ (a) and the conductivity vs. temperature at 100V. The linear slope yields an energy gap of 0.36eV (b).

Both crystals show a thermally activated conductivity behavior for temperatures above 240 K. DTBDT-TCNQ shows a higher resistivity and hence a larger transport gap in comparison to DTBDT-F_4TCNQ.

Table 6.2. Values from DFT calculations for the charge ρ on TCNQ-F_4TCNQ and the band gap for both DTBDT-TCNQ and DTBDT-F_4TCNQ crystals in comparison to experimental values.

	ρ (e)	Charge gap (eV)	ρ (e)	ΔE_{tr} (eV)
	From DFT calculations		From IR spectroscopy	From transport measurements
DTBDT-TCNQ	0.31	0.48	0.24(1)	0.51(1)
DTBDT-F_4TCNQ	0.36	0.34	0.21(1)	0.36(1)

It should be noted that the calculated gap is the distance between the top of the valence band (upper edge of HOMO) and the bottom of the conduction band (lower edge of LUMO). The experimental gap ΔE_{tr}, determined from the Arrhenius plot (eq. 6.3), excellently agrees with the calculated values (see Table 6.2).

6.4. NEXAFS on DTBDT-TCNQ and DTBDT-F_4TCNQ

Experimental results for the nitrogen and fluorine K-edge NEXAFS spectra for DTBDT-TCNQ and DTBDT-F_4TCNQ are shown in Figure 6.6. Nitrogen and fluorine are exclusively present in the acceptor (see Fig. 6.1 (a)). Therefore, it is possible to follow the change of the unoccupied charge density distribution of the acceptor upon formation of the complex without interfering with orbitals that are localized at the donor.

The nitrogen K-edge NEXAFS spectra of TCNQ (Fig. 6.6 (a)) consist of peaks A-D. The major signal (B) is not split into two components as in previous works, [88], [89] as is evident from theory (see below). The peak maxima are located at photon energies of 396.21, 398.17, 399.17 and 400.96 eV, respectively, as determined by the fit routine. Comparing the nitrogen K-edge spectra of the DTBDT-TCNQ microcrystals with pure TCNQ powder (Fig. 6.6 (a)), two main changes should be noticed: firstly, peak A decreases and broadens. Secondly, the intensity increase of the high energy tail of peak B masks peak

C. In addition, an overall decrease of the absorption intensity is observed, which is attributed to the lower concentration of nitrogen atoms in the mixed compound (16% less in relation to the crystalline TCNQ).

Due to similar configuration of the cyano groups in TCNQ and F_4TCNQ, their nitrogen K-edge spectra have similar shapes. Therefore, the spectra for F_4TCNQ are also represented by peaks A-D with slightly shifted positions of maxima at 395.98, 398.21, 399.35 and 401.25 eV, respectively (Fig. 6.6 (b)). Similarly to the previous case, in the nitrogen spectra for DTBDT-F_4TCNQ the intensity of the highest peak B is lower due to lower nitrogen content. Peaks A and C have higher intensities, which will be discussed below. Figure 6.6 (c) shows the fluorine K-edge NEXAFS spectra of DTBDT-F_4TCNQ in comparison to the pure acceptor F_4TCNQ. The spectra consist of peaks F-I and a weak signal E in the low-energy shoulder of peak F. The intensity is decreased in the CT compound for all peaks due to the fluorine abundance.

Fig. 6.7 presents a summary on the comparison between the experimental NEXAFS data for all systems and the calculated spectra with the Z+1/2 method[10]. The Z+1/2 PDOS (shaded regions) is plotted as well as the convoluted results (blue lines), assuming a life-time broadening of Γ = 0.5 eV. The agreement with the experimental NEXAFS data is remarkable and sets the stage for interpreting the experimental observations.

For the peak assignment the relation of Figs. 6.8 (a), (b) the TCNQ Z+1/2 PDOS (which reproduces the experimental results) with the DOS in TCNQ was used. Keeping in mind that NEXAFS is a local probe that provides information on the N 2p states and through them, of the bonding related to the nitrogen atoms, it is observed that the most prominent peak B in the spectra (Fig. 6.7) corresponds directly to the newly created 2p state through the core hole excitation (sharp peak at 2.2 eV in Fig. 6.8 (b)). Peak A corresponds to the LUMO level of TCNQ which is a σ^* resonance originating from the lowest empty orbitals from the cyano groups in the TCNQ molecule. Peaks C and D are directly associated with the higher unoccupied nitrogen 2p levels hybridizing with carbon states (a molecular orbital picture of the higher energy levels is unrealistic due to the high delocalization of these states). A similar analysis can be done for the acceptor F_4TCNQ (see Fig. 6.8 (c-e)).

---

[10] More detail on the theoretical approaches used in the present work is represented in Chapter 3.6.

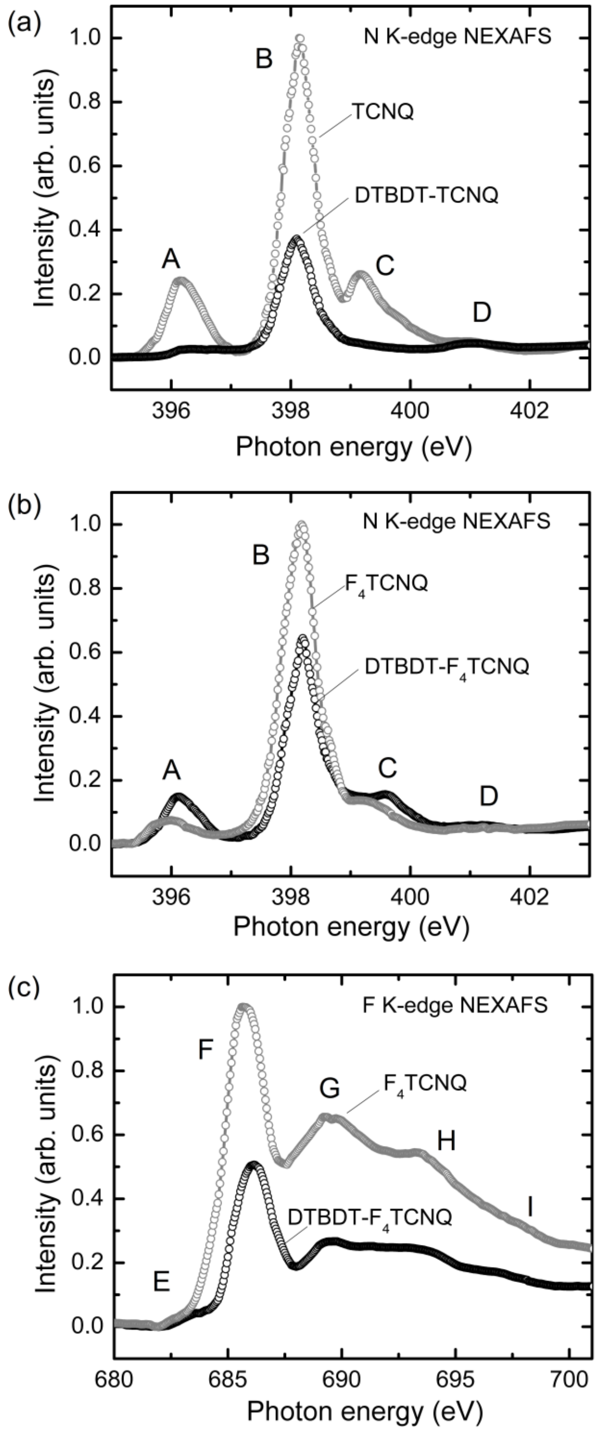

Figure 6.6. Nitrogen (a, b) and fluorine (c) K-edge spectra for pure acceptors and the CT complexes investigated in this work. Spectra of pure acceptors are scaled to 1 at maximum intensity, spectra of CT compounds have correct relative intensities accordingly. The intensity changes partly reflect the different atom densities in pure moieties and compounds.

In order to identify the peak structure in the compounds, the comparison between the DOS of DTBDT-TCNQ and the DOS of DTBDT-TCNQ is shown in Figs. 6.9 (a), (b), where a nitrogen atom has been substituted by a Z+1/2 atom (see Fig. 6.10 for the location of the nitrogen atom in the crystal structure). In Fig. 6.9 (b) the empty N(Z+1/2) states with p-character are plotted (blue curve) which correspond to strong NEXAFS signals because of the large matrix element of the 1s-2p dipole transition. Again, it is obvious that peak B in Fig. 6.7 corresponds to the newly created state through the core-hole that is partly hybridized with the LUMO+2 of the complex in the ground-state.

Since the most interesting is understanding the different charge transfer in DTBDT-TCNQ with respect to DTBDT-F_4TCNQ, the DOS comparison in DTBDT-F_4TCNQ is also shown in Fig. 6.9 (c-d). A high similarity of the results is observed in the vicinity of the Fermi energy in the initial state. The excited core hole provokes a similar shift of the higher lying unoccupied states towards the LUMO as in the case of DTBDT-TCNQ. In addition, Fig. 6.9 (e) shows the unoccupied orbitals localized at the F atom. The contribution of fluorine orbitals to the LUMO is very small.

The good agreement of the main peak positions observed in experiment and theory suggests that for both compounds peak A originates from the LUMO, which is located very close to the Fermi energy. Accordingly, this orbital carries signatures of the charge transfer.

The higher lying orbitals (peaks B, C and D) observed in the experiment are apparently shifted to lower energies by the core hole which is only partially screened. In the initial state they are separated from the LUMO by more than 1 eV and it is therefore unlikely that these orbitals take part in the charge transfer process.

For the assignment of the molecular states Wannier functions were calculated for the conduction band, originating mostly from the LUMO orbital of the acceptor molecules (see Fig. 6.11). In both compounds, the LUMO orbital is located nearly completely at the acceptor molecule. The theoretical results reveal that changes of the DOS weight of the LUMO comparing pure acceptor molecules with the CT compound are very subtle. This reflects the comparatively small charge transfer of a fraction of an electron per molecule. The absolute value of the charge transfer is in fact slightly larger for the case of F_4TCNQ as expected (see Table 2). The contribution of the LUMO localized at the nitrogen atom is again a fraction of the total LUMO. Since the fractional core hole does not change the

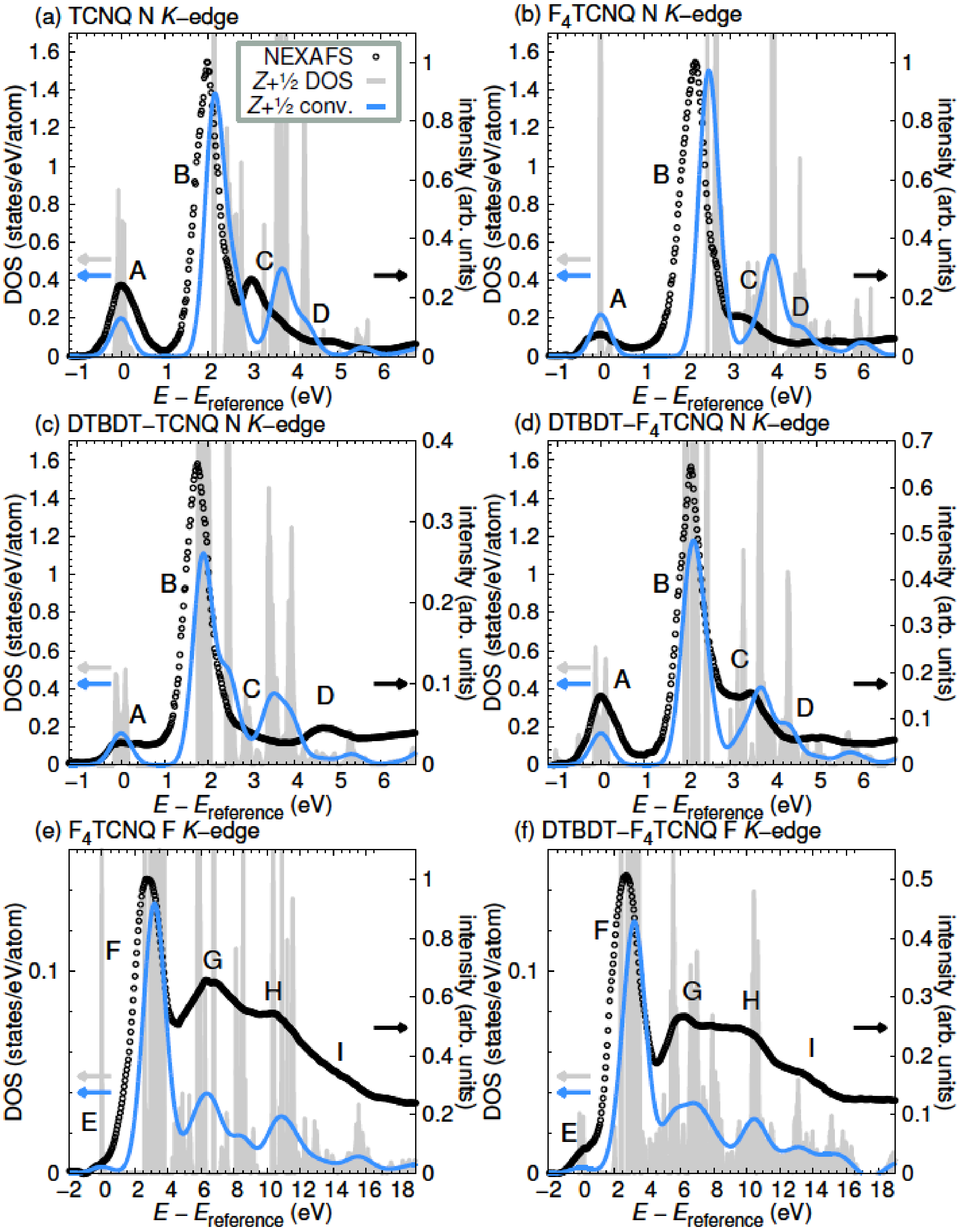

Figure 6.7. Nitrogen and fluorine K-edge NEXAFS measurements (black circles) in comparison with calculated results. Grey lines represent the local 2p densitiy of states for the ion with Z increased by 1/2. Blue lines represent the same data, but broadened with Γ = 0.5 eV for (a) to (d), and with Γ = 1.5 eV for (e) and (f). Experimental spectra of pure acceptors are scaled to 1 at maximum intensity, spectra of CT compounds have correct relative intensities accordingly. The energy scale is explained in the text.

integrated DOS of the LUMO one can also discuss the theoretical results shown in Figs. 6.7 (a) to (d) comparing the intensities of peak A in the pure acceptor with the mixed compound for the presence of half a core hole.

In DTBDT-TCNQ one observes both in the theoretical prediction and the experimental results that peak A decreases between the pure acceptor and the CT system. In contrast, for DTBDT-F_4TCNQ peak A shows an unexpected relative increase. The reason for this observation could be a preferential flat orientation of the DTBDT-F_4TCNQ single crystals on the sample holder. Please note, that DTBDT-F_4TCNQ and DTBDT-TCNQ crystals have different macroscopic shapes (see Fig. 6.1 (d), (e)). In this case the assumption of random orientation is not fulfilled and the preferential orientation very likely leads to a different excitation probability into the LUMO state in both compounds.

As the relative peak heights are no longer a conclusive measure of the charge transfer, one can discuss in the following the peak widths. Compared to the pure acceptor molecules, peak A broadens in the compounds. In the case of DTBDT-TCNQ, peak A even forms a flat region, while in the case of DTBDT-F_4TCNQ peak A develops a shoulder towards higher photon energy. This directly reflects the theoretical result of a band broadening of the LUMO caused by hybridization, see Fig. 6.8 (b) and (d). Without considering the lifetime broadening, the calculated LUMO bandwidth for the pure acceptor molecules is about 0.1 eV. For the compounds it increases to 0.2 eV (DTBDT-TCNQ) and 0.3 eV (DTBDT-F_4TCNQ).

More insight into the charge transfer process is gained from the Wannier functions shown in Fig. 6.11. It can be clearly seen that the LUMO extends to the adjacent donor molecules for both CT compounds. While the amount of intermolecular charge transfer is rather similar for both compounds, the intramolecular charge transfer shows subtle differences. In the case of DTBDT-TCNQ the LUMO shows a larger weight at the cyano groups at both ends of the TCNQ molecule. In the case of DTBDT-F_4TCNQ the LUMO weight is shifted more to the central part of the F_4TCNQ molecule. This might be caused by the strong electronegativity of the four F atoms close to the central part.

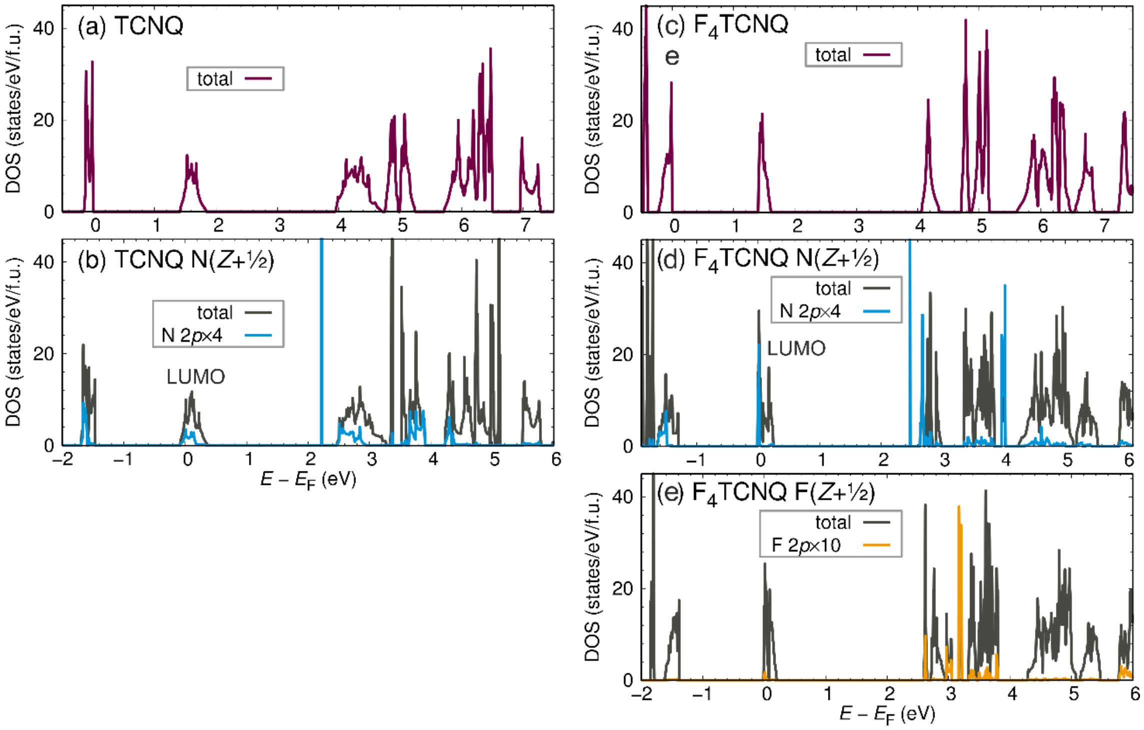

Figure 6.8. (a) Total density of states in TCNQ, (b) DOS in TCNQ with Z+1/2 for one nitrogen. (c) Total density of states in F$_4$TCNQ; total and partial density of states in F$_4$TCNQ with Z+1/2 for one nitrogen (d) and one fluorine (e).

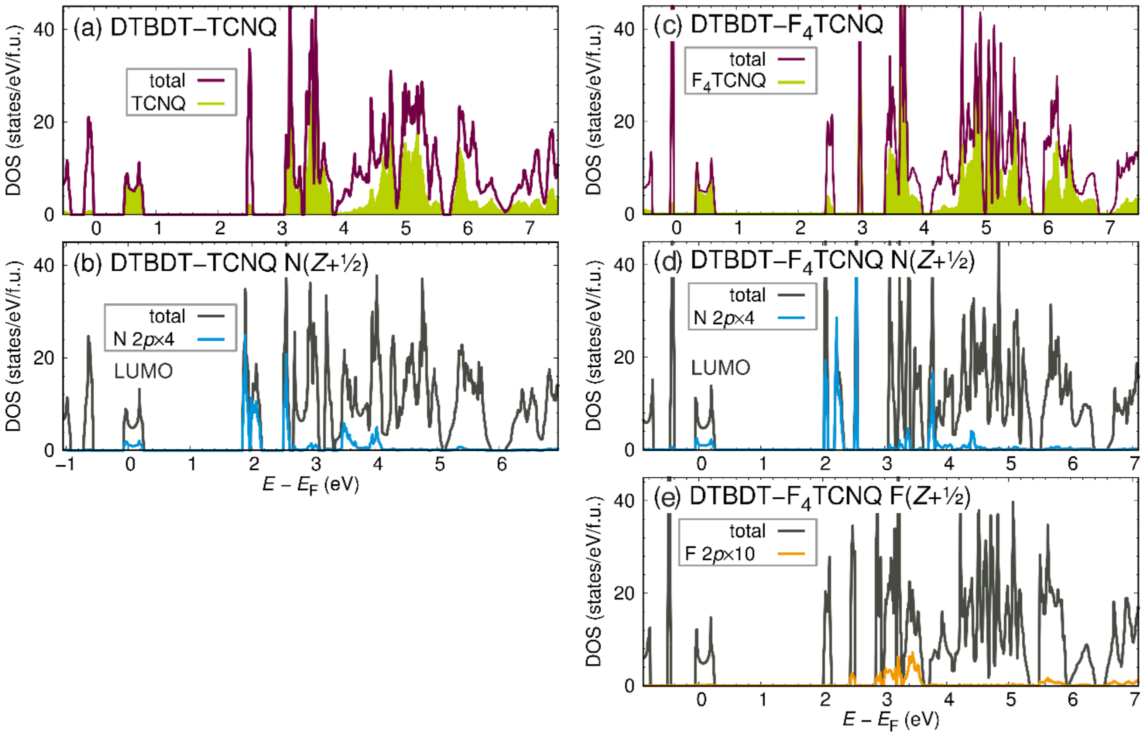

Figure 6.9. (a) Total density of states in DTBDT-TCNQ. (b) Same in DTBDT-TCNQ Z+1/2. (c) Same as in (a) but for DTBDT-F$_4$TCNQ. (d) Same in DTBDT-F$_4$TCNQ with Z+1/2 for one nitrogen, and (e) same with Z+1/2 for one fluorine.

For TCNQ on metal surfaces it was proposed that the charge transfer is initiated by charging the cyano groups [166]. These authors give the interpretation that the ionization of the cyano groups aromatizes the central hexagon ring, which can only take place by changing a specific bond from double to single. In such a scenario, the extra electron is thus accommodated in one of the cyano groups, so that one of the molecular ends remains radical in character, whereas the other end loses the radicaloid character by accumulating one extra electron. Bond conjugation at the dicyanomethylene ends, however, remains, so that both the extra electron and the radical character are delocalized at each cyano group. As a result, one double bond is shifted towards the central ring, which then would lead to the formation of a delocalized (benzene-like) π-state at the central ring. This scenario can be discarded in our case based on an inspection of Fig. 6.11, where the antisymmetric behavior of the LUMO is conserved for both compounds.

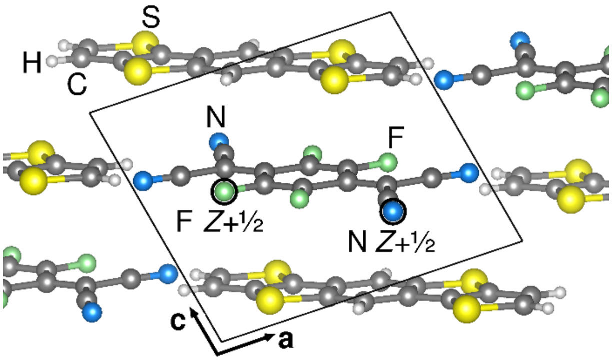

Figure 6.10. Position of the probed nitrogen and fluorine atoms in the CT complex.

Additional support for this explanation can be gained from the fluorine K-edge data. As can be deduced from Fig. 6.7 (e)-(f), the LUMO shows up as the small signal E at the at the low-energy onset of the NEXAFS spectrum, giving evidence of a small overlap between F 1s and the LUMO orbital. The same can be deduced from the small intensity of the LUMO (at 0 eV) in the theory spectra (blue curves in (e) and (f)). We also see from Fig. 6.11 (c) that the LUMO has only a very small contribution located at the fluorine sites.

(a) TCNQ

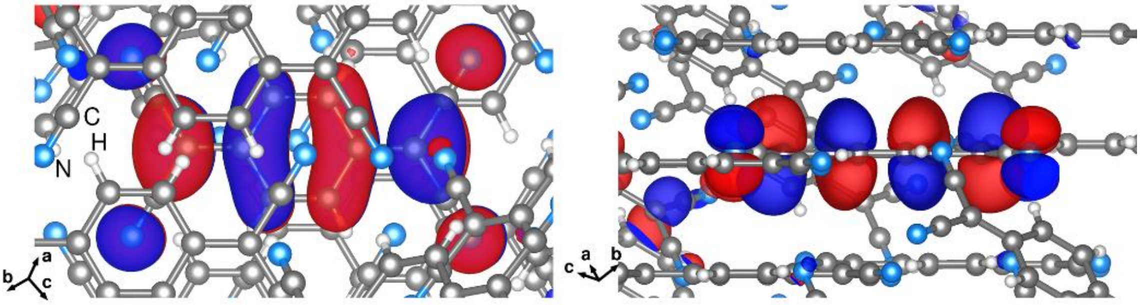

(b) DTBDT−TCNQ

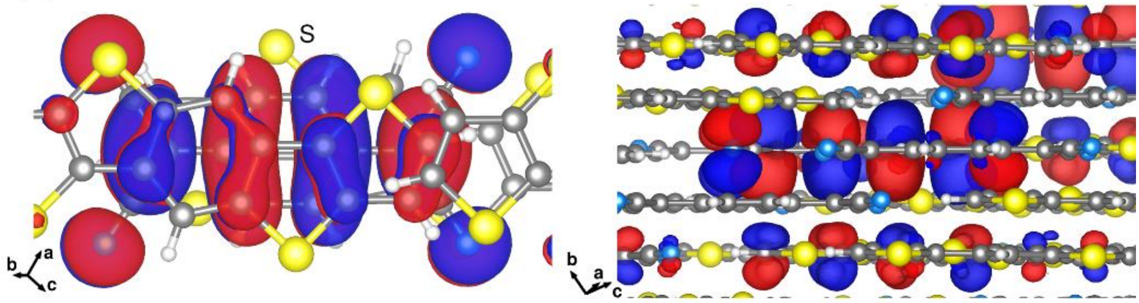

(c) DTBDT−F_4TCNQ

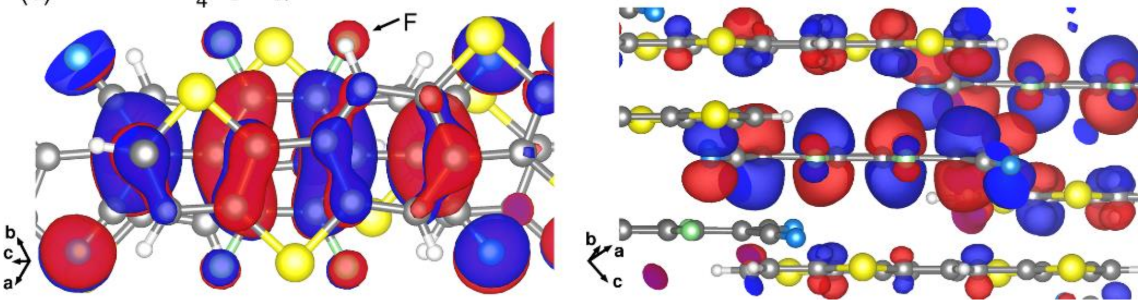

Figure 6.11. Unoccupied molecular orbitals of TCNQ (a) DTBDT-TCNQ (b) and DTBDT-F_4TCNQ (c) relevant for the discussion of the nitrogen K-edge NEXAFS spectra from DFT calculations. Energy values are given with respect to the highest occupied molecular state.

6.5. Summary

In summary, the main merit of this chapter is the successful explanation of NEXAFS spectra of molecules by considering a theoretical approach that includes final state effects beyond the sudden state approximation. While for naked atoms the absorption lines can be calculated exactly using the Hartree-Fock ansatz [167] in compounds a charge transfer multiplet calculation [167], [111] has been established that considers the surrounding of the excited atom as an electrical field distribution which represents a rather crude approximation. In the present chapter, it was found that the final state effect can be considered as an additional fractional positive charge at the core of the atom. This is shown by comparing supercell calculations that consider both the partial screening of the electron-hole Coulomb correlation on a static level and the rearrangement of electronic density with the computationally more effective Z+1/2 calculations. The consideration of fractional charges is quite equivalent to the reduction of the Slater integrals compared to atomic values that has been implemented in the charge transfer multiplet calculation schemes. This approach has the advantage that it is quite close to a first principles calculation and takes into account all molecular orbitals. This theoretical model is rather versatile and requires much less calculation time than a fully ab-initio time-dependent DFT calculation.

The calculations allowed a unique assignment of the experimentally observed NEXAFS peaks to molecular orbitals. For the novel charge transfer compounds DTBDT-TCNQ and DTBDT-F_4TCNQ the peaks at the lowest excitation energy in the nitrogen and fluorine K-edge spectra were identified as originating from the LUMO orbital. The different behavior of this peak comparing the two compounds indicates that the charge transfer mechanism is modified by the fluorine ligands and the resulting different crystal structure, leading to approximately the same amount of electron transfer, although the acceptor strength of F_4TCNQ is much larger.

7. Summary and conclusion

Charge transfer organic compounds are considered as potentially interesting materials for organic electronics for use in electronic devices. However, in order to get closer to the application in industry, several issues need to be addressed and solved. In the present work some fundamental questions related to the electronic structure of organic conductors are discussed. In particular, it is shown that photoemission and X-ray absorption spectroscopy techniques are very useful and sufficient for investigation of the electronic structure and its change crossing phase transition temperatures. Here the main results obtained within the framework of the present work are summarized.

Organic conductor crystals $(DOEO)_4[HgBr_4]\cdot TCE$ were investigated by photoemission methods XPS and HAXPES, exploiting different surface sensitivities in temperatures ranging from room temperature down to 40 K, in order to expand what is known about the electronic structure of this class of compounds. Comparison of the photoemission data with magnetic and transport characteristics gives deeper understanding of the electronic properties and the strong correlations of the main physical properties which exist in the material. All measurements performed in the present work (XPS, HAXPES and SQUID magnetometry), as well as previously published studies on resistivity and electron spin resonance (ESR), in total allow to map the one-dimensional phase diagram with a co-existing semiconducting phase above 120 K, a metallic phase in the region 60 K - 120 K, and an insulating ground state below 60 K. Additionally, the low-temperature phase was found to be antiferromagnetic and to contain a significant amount of co-existing different phases, which have different amounts of spin. The nature of these co-existing phases could not be uncovered in the present work. This requires microscopic techniques and is an interesting object for future studies.

The structure of unoccupied electronic states of TTF-TCNQ crystals was determined using NEXAFS and compared with theoretical calculations, provided by Prof. Dr. E.

Canadell (Bellaterra, Spain) and Prof. Dr. J.-P. Pouget (University Paris Sud, Orsay). The experimental observation of the band gap opening at the Peierls transition at 54 K was shown for the first time in the present work. Furthermore, the investigation of the electronic structure of TTF-TCNQ suggests possible deformation and even pyramidalization of the acceptor molecule TCNQ in the crystal structure below 100 K. Therefore, the pre-transitional structural distortion is also visible indirectly in the electronic structure of the charge transfer system. It should be mentioned that the discussion about orbital-selective temperature-dependent NEXAFS in TTF-TCNQ presented in the present Thesis and published in [86] is consistent with the classical way of NEXAFS analysis for organic charge transfer materials, especially in the discussion of TCNQ acceptor, and previously published investigations [88], [138], [89]. However, the most recent study, performed in collaboration with Prof. Dr. Roser Valentí (University of Frankfurt (M)) on other charge transfer systems [168], uses different theoretical approach and provides therefore additional insights and details that were impossible to get using the classical way of calculations.

The mechanism of charge transfer in DTBDT-TCNQ and DTBDT-F_4TCNQ crystals was investigated using NEXAFS at room temperature. The complex study performed in close cooperation with R. Valentí et al. reveals that the classical theoretical approach based on sudden state approximation is not sufficient for discussion of NEXAFS in organic charge transfer compounds. Instead, consideration of the partial screening of the electron-hole Coulomb correlation on a static level and the faster calculations based on the Z+1/2 approximation (where the core hole effects are simulated by replacing N or F with atomic number Z with an atom with atomic number Z+1/2) give reproducible results with excellent agreement with the experiment. Investigation shows that, in contrast to the widely acknowledged model, only the lowest unoccupied electronic orbitals of acceptors are involved in the charge transfer by hybridization with donor electronic states. The different behavior of the LUMO peak comparing the two compounds indicates that the mechanism of charge transfer is modified by the fluorine ligands in the central part of the acceptor molecule and the resulting different crystal structure, leading to approximately the same amount of electron transfer, although the acceptor strength of F_4TCNQ is much larger.

8. Perspectives and Outlook

Very little research investigating the valence electronic structure of organic materials is currently available. Restrictions of the present techniques make it almost impossible to carry out electronic band mapping. However, an experimental study of the electronic structure of the valence bands would help greatly in broadening the understanding of many phenomena like the Mott insulator transition or the Peierls transition or superconductivity in organics. The first successful measurements were recently performed using time-of-flight momentum microscopy on classical metals [169]. This new method detects all photoelectrons in the full half-space above the sample surface with a few meV energy resolution and 10^{-2} $Å^{-1}$ momentum resolution. Maximum detection efficiency (full solid angle) means minimum sample damage (all photoelectrons recorded simultaneously via time-of-fight detection). Hence, this method is ideally suited for the study of sensitive organic species. Possibly, the new technique would allow for direct access to the electronic structure of the organic conductors and allow for the investigation of electronic redistributions more efficiently.

Concerning materials under investigation, during the present work, first under-pressure measurements on $(DOEO)_4[HgBr_4]{\cdot}TCE$ crystals were performed on magnetic susceptibility and electron transport in order to obtain relevant information for the two-dimensional pressure - temperature phase diagram for this compound. Theoretical predictions and pilot measurements do not exclude superconductivity under a pressure of more than 3 kbar. However, this should be investigated in more detail, as more statistics and reproducibility of the results are needed.

Photoemission and X-ray absorption spectroscopies still can provide much valuable information on novel organic conductors due to the versatility of these methods for the experimental investigation of the electronic structure.

Appendix 1

Investigation on charge transfer complex formation in triangulene based thin films

Besides the experiments performed on crystalline samples, described and discussed in the main part of the present work, several series of spectroscopic studies were done in the laboratory on thin molecular films. Due to the leak of existing theoretical calculations, and the limitations of the infrared spectroscopy on thin films, the discussion of this topic is not complete. Hence, these data are placed in the appendix, as a first guideline for future investigations.

Thin molecular films – why?

Studies of the crystalline phase are the traditional way to look at the properties of new charge-transfer compounds. However, it is not always possible to synthesize crystals suitable for spectroscopic methods using classical methods like vapor diffusion and electrocrystallization due to technical limitations, for example, the non-existence of a suitable common solvent. That is why in such cases thin film evaporation in ultra-high vacuum (UHV) is a good alternative. Usually donors and acceptors are being co-evaporated *in-situ* in the necessary stoichiometric ratio. This approach appears suitable, as it was discovered for the classical donor-acceptor system (BEDT-TTF)–TCNQ, where

BEDT-TTF is bis-etilenedithiatetrathiafulvalene and TCNQ is tetracyanoquinodimethane, that UHV co-deposition can lead to the formation of a microcrystalline layer of a new charge transfer (CT) phase in a thin film [170]. Such kinds of thin films can be investigated using spectroscopic methods UPS [21], [171], [172], [173], inverse photoelectron spectroscopy (IPES) [174], [175], infrared spectroscopy (IR) [21], [176] or NEXAFS [145], [146], [89], [87] and scanning tunneling microscopy (STM) [21], [177], [178], [179], [180]. Furthermore, it was shown that the surface could be not only a passive template but it is able to stabilize radicals by donating electron density to the latter, influencing the mobility and coupling affinity of molecules [179].

However, in case of thin film deposition there is an additional scenario. The interface between organic molecules and metallic substrate appears and the charge transfer between substrate and film can occur. It was reported that for F_4TCNQ (tetrafluorotetracyanoquinodimethane, Fig. A-1.1) on various substrates, pronounced electron-transfer from the metal to the molecule in the monolayer occurs [172], [173], [174], [175], [181], [182], [183]. When the organic film is grown in bad vacuum where the metal surface is passivated by an oxide layer formation or hydrocarbon coverage, the metal wave function is not coupled with the organic wave function and interface states are not formed, so partial charge transfer does not take place [173].

The new class of donors and acceptors is represented by derivatives of the compound (4,4,8,8,12,12-hexamethyl-4*H*,8*H*,12*H*-benzo[1,9]quinolizino[3,4,5,6,7-*defg*]acridine) [184], so-called heterotriangulene or triangulene (Fig. A.1). Based on this precursor, many new donors and acceptors with more complicated structures, including polymers, were recently synthesized [177], [178], [179], [184], [185], [186], [187], [188]. It was shown that most of these molecules could be investigated via scanning tunneling microscopy [177], [178], [179]. That provides expectations of the possibility of using surface spectroscopy methods for electronic structure investigations.

In the following, UPS and NEXAFS results are represented for a series of molecular beam deposited thin films of triangulene and its trimethoxy derivative donors in combination with a sequence of three acceptors (see Fig. A-1.1) in comparison to density functional theory (DFT) calculations. Ultraviolet photoelectron spectroscopy provides the information about occupied valence states while NEXAFS measurements give direct access to the unoccupied ones. Finally, the whole information about the density of states is available for these charge-transfer systems.

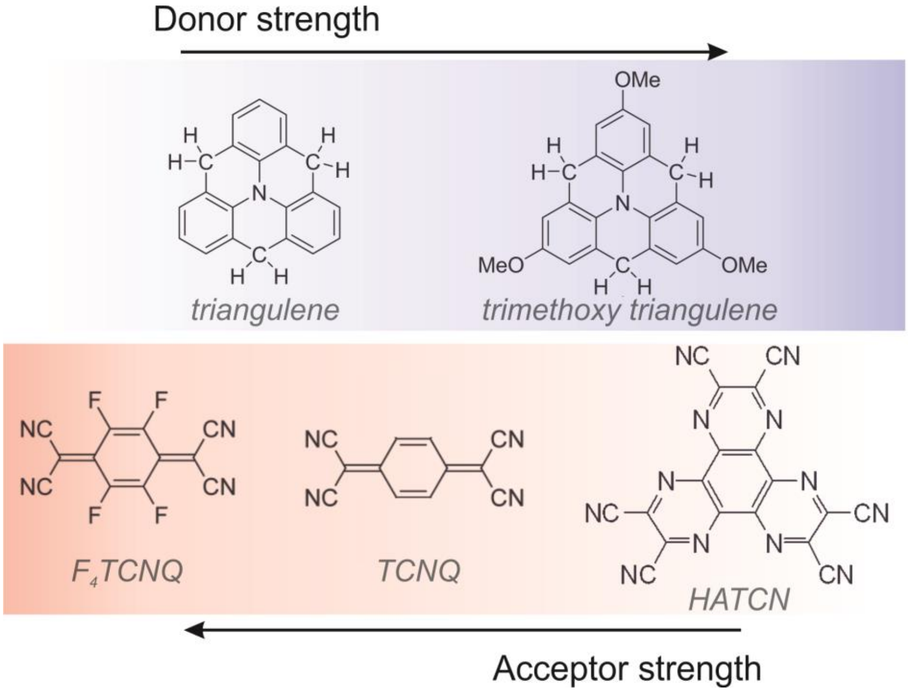

Figure A-1.1. Molecular structures of donors based on triangulene derivatives and three acceptors studied in the present work.

Also it is very interesting to compare CT complex formation and film growth mechanisms in a series of compounds where the donor/acceptor properties were tuned via the donor/acceptor strength. For this purpose triangulene (Tria) and trimethoxy triangulene (Ome) were used as donors and TCNQ, F_4TCNQ and HATCN (1,4,5,8,9,11-hexaazatriphenylene hexacarbonitrile) as acceptors.

Sample preparation and experimental details

The UPS experiments were performed in a UHV chamber equipped with a photoelectron spectrometer, a helium discharge lamp and 6 Helmholtz coils in order to compensate magnetic fields inside the chamber (Fig. A-1.2). The He I line ($h\nu$=21.23 eV) was used for excitation. The photon beam is oriented under 45° to the entrance lens of the spectrometer and the sample can be rotated in the plane perpendicular to the plane of the incidence. For co-deposition of donor and acceptor molecules, in particular for species with low sublimation temperatures, a special load-lock system for crucibles was used [21]. The base pressure was 10^{-9} mbar. Firstly, a gold film was deposited onto a silicon wafer with native SiO_x surface layer using an e-beam evaporator (UHV evaporator type Focus EFM 3). Freshly deposited gold films exhibited a work function Φ of 4.8 – 5.0 eV, indicative of a polycrystalline surface [189], [190]. Clean gold films were used as substrates with high electronegativity and relatively flat valence region on the spectrum, providing a good reference for the Fermi energy and being a good substrate for molecular growth.

The NEXAFS measurements were done using soft X-rays from the WERA beamline at ANKA, Karlsruhe, at an energy resolution of 150 meV. In the total electron yield mode employed, the drain current from the sample is detected. The electron emission yield originates from a subsequent Auger process that neutralizes the core hole and leads to the emission of Auger electrons and slow secondary electrons. The information depth is about 5 nm.

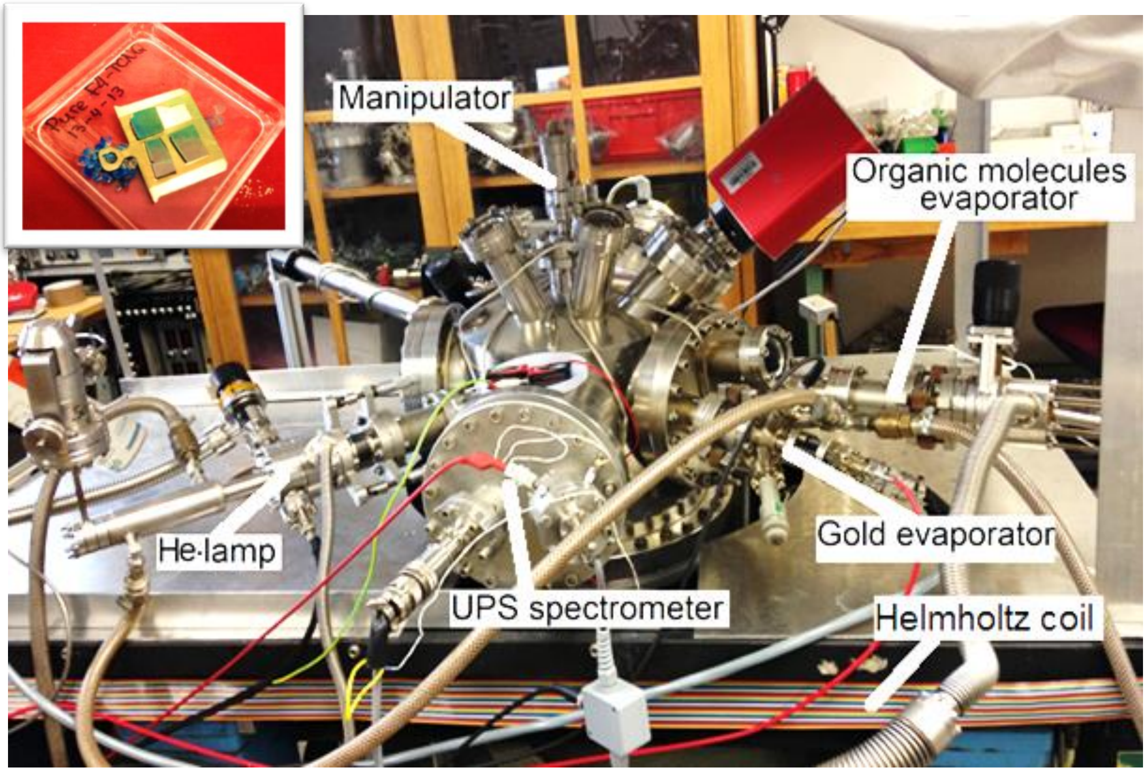

Figure A-1.2. Experimental UHV setup for the UPS investigation of in-situ evaporated organic materials under laboratory conditions. The inset represents a typical thin molecular film on the sample holder.

The calculations[11] were performed using the Orca program [108] for geometry optimization and potential energy surface scans. The BP86 [191], [192] functional with the Ahlrichs def2-TZVP [193], [194] basis sets for all the atoms in combination with the def2-TZV/J Coulomb fitting basis for the resolution of identity were used. The Grimme's D3 dispersion correction [195] with BJ-damping [196] was used. Potential energy surface scans were performed optimizing geometries of complexes of F_4TCNQ with triangulene and trimethoxy triangulene donors, in cofacial geometry and by varying the intermolecular distance between the molecular centers along the x and y axes. The complexes with the relative energy of less than 3 kcal/mol were chosen for further investigations. Electron binding energies or ionization potentials of molecules were calculated by the delta self-consistent field (ΔSCF) method applied together with the B3LYP functional in conjunction with DZ, DZP and TZP (for separate molecules also with TZ2P and QZ4P) basis sets within ADF 2013 program.

Triangulene and trimethoxy triangulene were synthesized in Max-Planck Institute for Polymer Research (Mainz)[12]; F_4-TCNQ was commercial (Fisher Scientific). Molecular films were sublimed at crucible temperatures of 423 K (Tria), 463 K (Ome), 438 K (F_4TCNQ), 480 K (TCNQ) and 440 K (HATCN).

Part 1: Triangulene derivatives in composition with acceptor F_4TCNQ

A series of photoelectron spectra taken during co-deposition of triangulene and trimethoxy triangulene donors on clean fresh Au surfaces are shown in Fig. A-1.3. Peaks in the spectra correspond to the highest occupied molecular orbital (HOMO) and several low-lying molecular orbitals. For pure triangulene on Au (Fig. A-1.3., a), the work function Φ drops from 4.9 to 3.6 eV during deposition (Fig. A-1.4., a). The shape of

---

[11] The DFT calculations were performed by Dr. Tatyana Shubina (Computer-Chemie-Centrum and Interdisciplinary Center for Molecular Materials, Erlangen).

[12] The synthesis was performed by Dr. Milan Kivala, (Max-Planck Institute for Polymer Research, Mainz).

coverage dependence of the work function shows a slight decrease in the first part and then a sharp drop until the minimum value upon further deposition. In the case of a trimethoxy triangulene film on the Au surface (Fig. A-1.3., b) the work function drop is from 5.0 to 4.2 eV (Fig. A-1.4., b) during evaporation which is less than that observed for triangulene. Part of the drop in Φ in both cases reflects the push-back effect, i.e. Pauli repulsion on the spill-out charge of the metal surface by the valence electrons in molecules of the first monolayer. This reduces the surface dipole of the metal and thus lower the work function. However, the strong and rapid drop for triangulene (Fig. A-1.4., a) can only be explained by an additional charge transfer from the donor molecules to the Au substrate. This is accompanied by a peak at 0.7 eV binding energy (Fig. A-1.3., a, red and blue curves), indicative of an interface state.

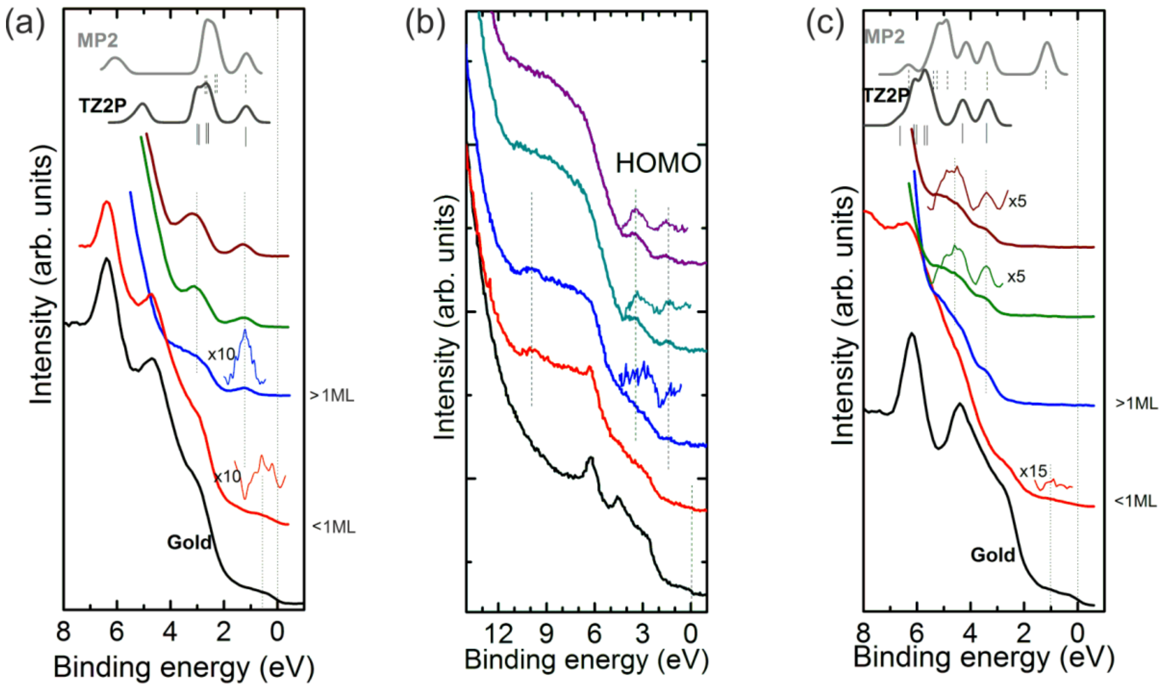

Figure A-1.3. Coverage series of He I UPS spectra of triangulene (a), trimethoxy triangulene (b) and F_4TCNQ (c) on Au. The lowest spectrum shows always the signal from the clean gold film, as reference. The sequence of spectra was taken during the growth of the pure donor / pure acceptor film. The upper panel shows comparison of the experiment with the theoretical calculations (courtesy Tatyana Shubina).

The system F_4TCNQ on Au (Fig. A-1.3., c) is more complicated and was described in detail in Refs. [172], [173], [174]. During molecular deposition to the substrate, a weak peak appears at 1.10 eV below E_F in the submonolayer regime. The peak positions and work function change from 4.8 to 6.1 eV (Fig. A-1.4., c) are in agreement with literature [172], [173], [174]. The low-energy peak is not observable for the multilayer since only molecules closest to the substrate are involved in the charge transfer [173].

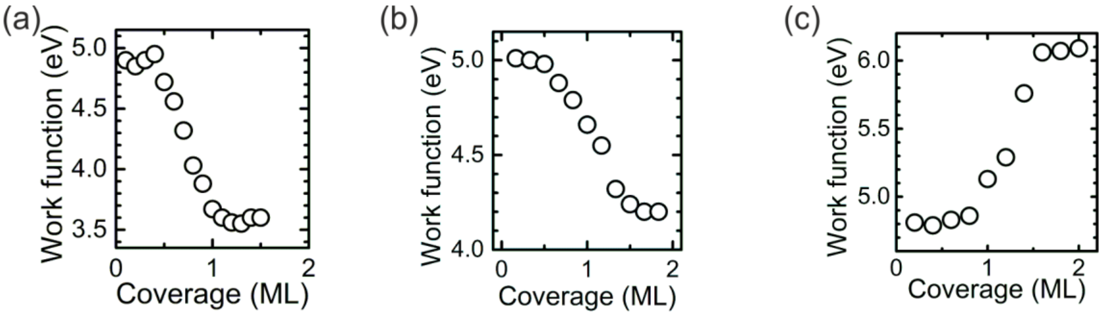

Figure A-1.4. Work functions of the pure triangulene donor (a), trimethoxy triangulene (b) and F_4TCNQ (c) on Au substrate.

Figure A-1.5. shows a sequence of photoelectron spectra for mixed phases of triangulene – F_4TCNQ (a) and trimethoxy triangulene - F_4TCNQ (b) that were deposited layer by layer due to difference in evaporation temperatures.

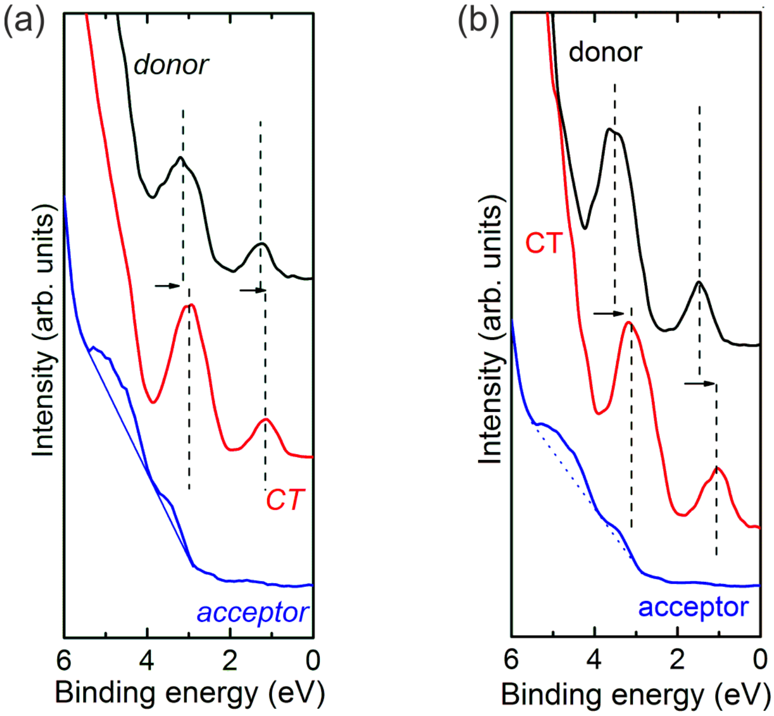

Figure A-1.5. He I UPS spectra of charge transfer complexes triangulene-F_4TCNQ (a) and trimethoxy triangulene-F_4TCNQ (b) on Au. Bottom spectra show the signal from the pure acceptor, the top spectra were taken for the pure donor and the center spectra were taken during layer-by-layer deposition of the donor and acceptor.

When comparing the UPS series for the pure donors with spectra of the mixtures, one observes the following spectral shifts of the HOMO positions: 150 meV for the Tria-

F_4TCNQ compound and 400 meV for the Ome-F_4TCNQ mixture. From this, one concludes that there is a formation of new compounds with a band structure, where the HOMO levels are located at new positions in comparison to pure species.

NEXAFS spectra at the nitrogen K-edge were taken for thin films of triangulene and trimethoxy triangulene donors, F_4TCNQ acceptor, and a charge transfer (CT) mixture of them on fresh clean Au surfaces. Typical results for the nitrogen K-edge spectra are shown in Figure A-1.6. Nitrogen is present in the donors and in the acceptor as well. It is interesting to note, that signals from the triangulene skeleton and from the acceptor groups are energetically separated in the NEXAFS spectrum. Donor signals are situated in the energy range 400-415 eV, while acceptor lines are in the 396-405 eV energy rage.

The spectra for the nitrogen K-edge for triangulene, F_4TCNQ, and CT complex of them (Fig. A-1.6, a), as well as the spectra for nitrogen K-edge for trimethoxy triangulene, F_4TCNQ, and CT complex of them (Fig. A-1.6, b) are represented in comparison to the theoretical calculations. The NEXAFS spectra could be compared to the theoretical lowest unoccupied molecular orbital (LUMO) and to several more unoccupied molecular orbitals, situated above the LUMO.

In the spectrum of the mixture phase based on the triangulene donor (Fig. A-1.6., a) the pre-peak intensity at 398.5 eV is significantly smaller than the pre-peak intensity for pure F_4TCNQ film. This is an indication of a change of the density of unoccupied states in the corresponding orbitals of the acceptor, since NEXAFS is a probe for the unoccupied electronic states.

In the case of charge-transfer complex based on trimethoxy triangulene donor (Fig. A-1.6., b) the mixture phase spectrum looks different from the previous case. The peak at 398.5 eV is almost nonexistent. This is a fingerprint of a strong filling of unoccupied states in the F_4TCNQ acceptor. A disappearance of the first peak of the acceptor NEXAFS spectrum was also detected for the system F_4TCNQ on Cu surface with complete charge transfer[166]. And it is exactly what one could expect to see for the mixture Ome-F_4TCNQ. The mixture phase spectrum also includes peaks attributed to the pure donor. This could be a result of inhomogeneous film growth where, together with CT phase, there is a small amount of pure donor phase. With a beam size of 60x40 µm it is possible to detect all phases under this beam surface in the measurements.

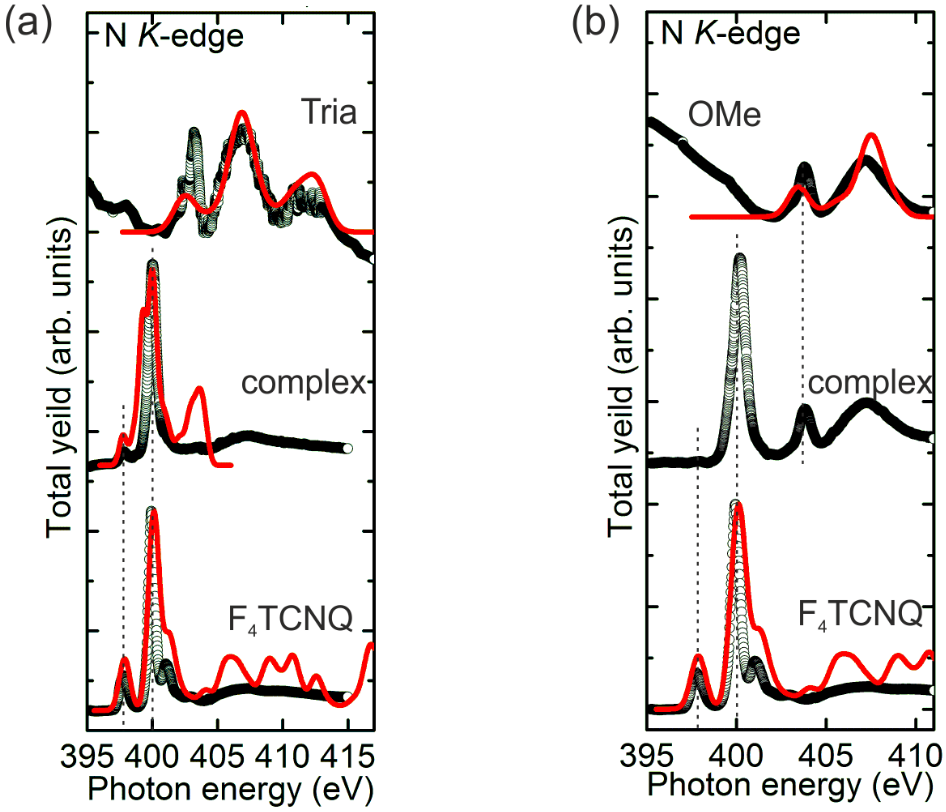

Figure A-1.6. (a) Nitrogen K-edge NEXAFS spectra of the triangulene donor (top), CT complex (middle) and F_4TCNQ acceptor (bottom). (b) Same for the trimethoxy triangulene donor (top), CT complex (middle) and F_4TCNQ acceptor (bottom). Circles denote experimental data. Thin curves show theoretical calculations (courtesy T. Shubina). The yield scales are normalized to the maxima of the highest peaks.

Figures A-1.7-A-1.9. show theoretically calculated energy positions of the investigated pure species in comparison to their charge transfer mixture. The incomplete theoretical investigation does not allow for the discussion of the orbital separation and orbital filling with charge transfer complex formation. However, it is clearly seen that this process is much stronger for the Ome-F_4TCNQ mixture.

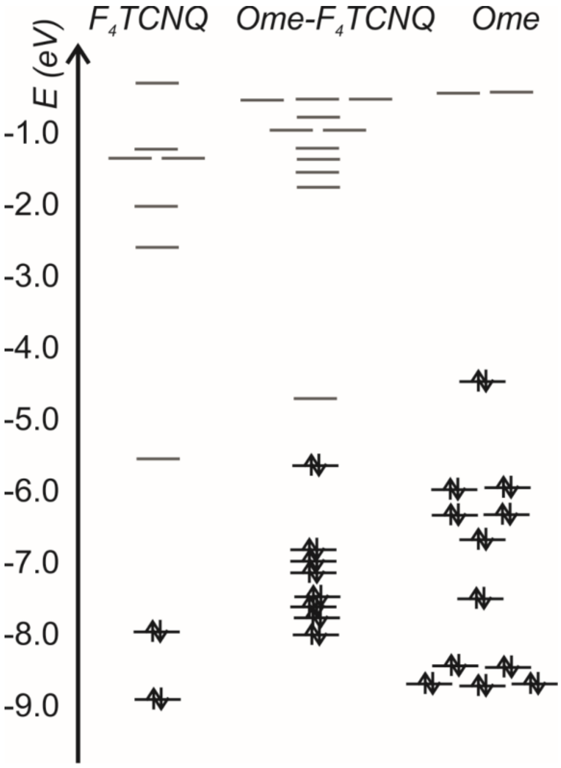

Figure A-1.7. Calculated level diagram for the charge transfer complex and separate donor and acceptor molecules (left: F_4TCNQ, middle: CT, right: trimethoxytriangulene) at the B3LYP-D3/TZP level. Orbital energy levels in eV. (courtesy T. Shubina)

Generally, when considering the potential application in organic electronics, it is very important that the amount of charge transfer is around 0.3 *e* and that it could be tuned. For this reason, the LUMO of the acceptor should be situated slightly above the HOMO of the donor in energy scale. Therefore, the tendency of the donor-acceptor pair to the complete charge transfer of 1 *e* would be not supported energetically. In contrast to this, in the present case both donors, triangulene and trimethoxy triangulene, have their HOMOs situated above the LUMO of F_4TCNQ, supporting a complete charge transfer. Experimentally, the tendency for complete charge transfer is also clearly seen by filling of the orbital corresponding to the peak at 398.5 eV in the NEXAFS spectra.

MO	F4-TCNQ	Energy, eV	Triangulene	Energy, eV	OMe-Triangulene	Energy, eV
LUMO	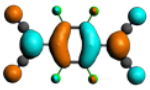	-5.59	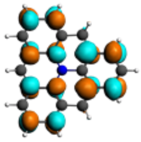	-0.59	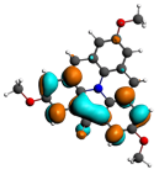	-0.48
HOMO	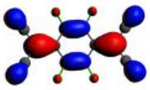	-8.04	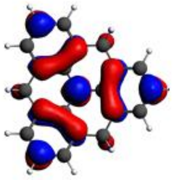	-5.04	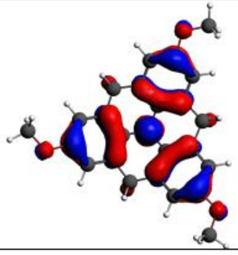	-4.51

Figure A-1.8. Theoretically calculated HOMO and LUMO energy levels of the investigated compounds.

MO	CT1	Energy, eV
LUMO	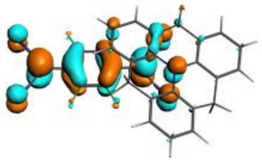	-4.77
HOMO	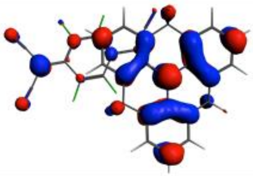	-5.71

Figure A-1.9. Theoretically calculated HOMO and LUMO energy levels of the charge transfer compound Ome-F_4TCNQ.

In conclusion to part 1, the investigation of the complex formation of Tria-F_4TCNQ and Ome-F_4TCNQ by means of UPS, NEXAFS and DFT shows complete or almost complete charge transfer with complete vanishing of the pre-peak in NEXAFS of F_4TCNQ and shifts of the HOMO of 150 meV and 400 meV for triangulene and trimethoxy triangulene, respectively.

Part 2: Triangulene derivatives in composition with acceptor TCNQ

To continue the systematic analysis of charge transfer molecular thin films based on triangulene derivatives, the acceptor TCNQ with a LUMO level situated at -4.82 eV below the vacuum level was used. The level diagram (Fig. A-1.10) suggests a complete charge transfer for Ome-TCNQ due to the HOMO of the donor being situated above the LUMO of the acceptor. In contrast, the HOMO of the Tria donor is situated below the LUMO of the acceptor, establishing the precondition for a partial, controlled charge transfer.

Investigation of thin molecular films of the pure species in comparison to the mixtures (Fig. A-1.11) shows a 340 meV shift to lower energies in the case of the HOMO of triangulene-TCNQ and 400 meV shift in the case of Ome-TCNQ (the same direction and value as seen in the complex with a F_4TCNQ acceptor). Taking into account the relative energetic positions of donors and the TCNQ acceptor, one can conclude that the CT is still complete in Ome-TCNQ and should be incomplete in the case of Tria-TCNQ.

The HOMO shift of Tria-TCNQ is larger than in the mixture Tria-F_4TCNQ, although the TCNQ acceptor is weaker. This could be understood from a structural point of view. Spatially the TCNQ molecule is smaller than F_4TCNQ and does not have the additional four fluorine atoms, that can stabilize the molecule and additionally enforce screening of the central part. Therefore, the intramolecular distances between Tria and TCNQ could be significantly smaller than those on case of F_4TCNQ, providing larger charge transfer.

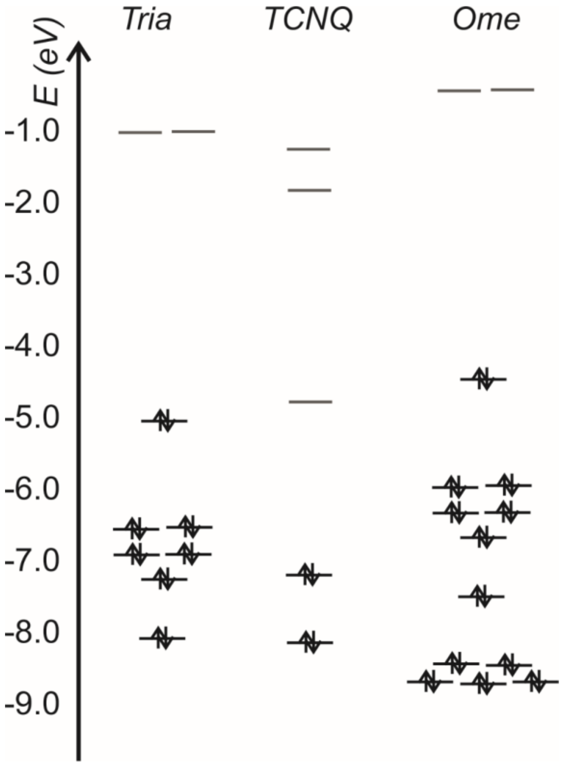

Figure A-1.10. Schematic level diagram for the two donors and TCNQ acceptor molecules.

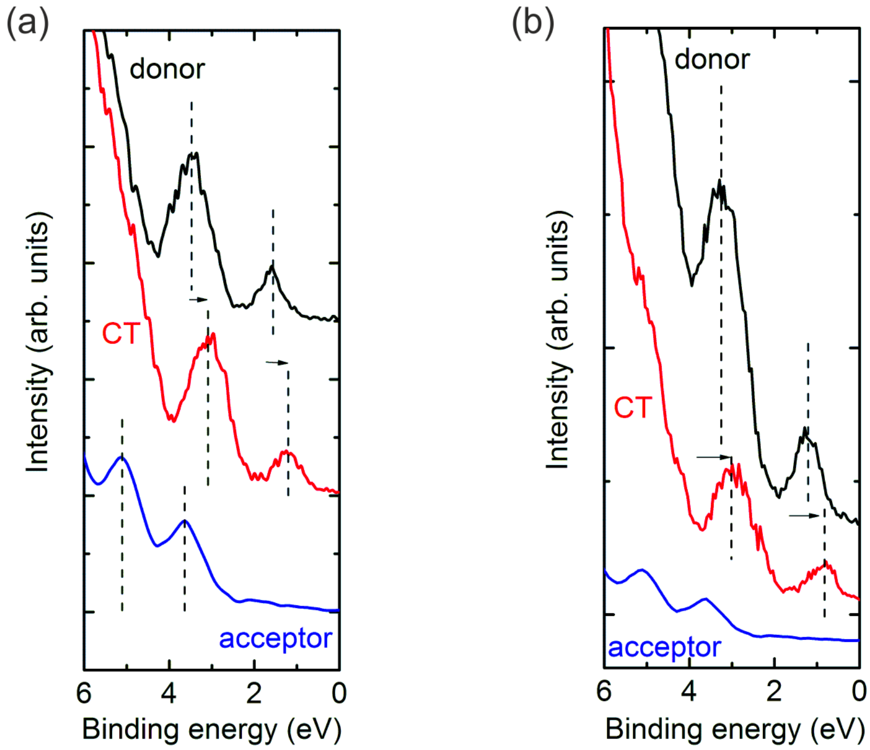

Figure A-1.11. He I UPS spectra of charge transfer complexes triangulene-TCNQ (a) and trimethoxy triangulene-TCNQ (b) on Au. Bottom spectra show the signal from the pure acceptor, the top spectra were taken for the pure donor and the center spectra were taken during layer-by-layer deposition of the donor and acceptor.

Part 3: Triangulene derivatives in composition with acceptor HATCN

The acceptor HATCN has its LUMO situated at -4.6 eV below the vacuum level, making it the weakest of the acceptors studied here. That means that the charge transfer is supposed to be less than 1 *e* and the smallest in the whole sequence of experiments due to the LUMO of the acceptor lying above the HOMO of both donors (Fig. A-1.12).

Analysis of the UPS spectra of donors, HATCN acceptor, and their mixtures shows charge transfer complex formation, that can be seen as energetic shifts of the HOMO level for the mixture compound in comparison with the pure donors (Fig. A-1.13). however, unlike the previous cases for TCNQ and F_4TCNQ, the HOMO shifts to higher and lower binding energies. For Tria-HATCN the shift of 110 meV to higher binding energies is observed, while for the Ome-HATCN compound the shift is 200 meV to lower binding energies.

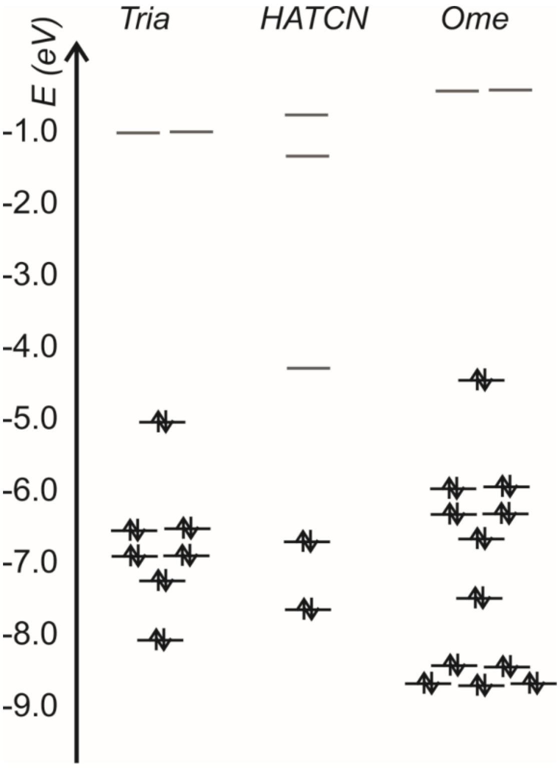

Figure A-1.12. Schematic level diagram for the two donors and the HATCN acceptor molecules.

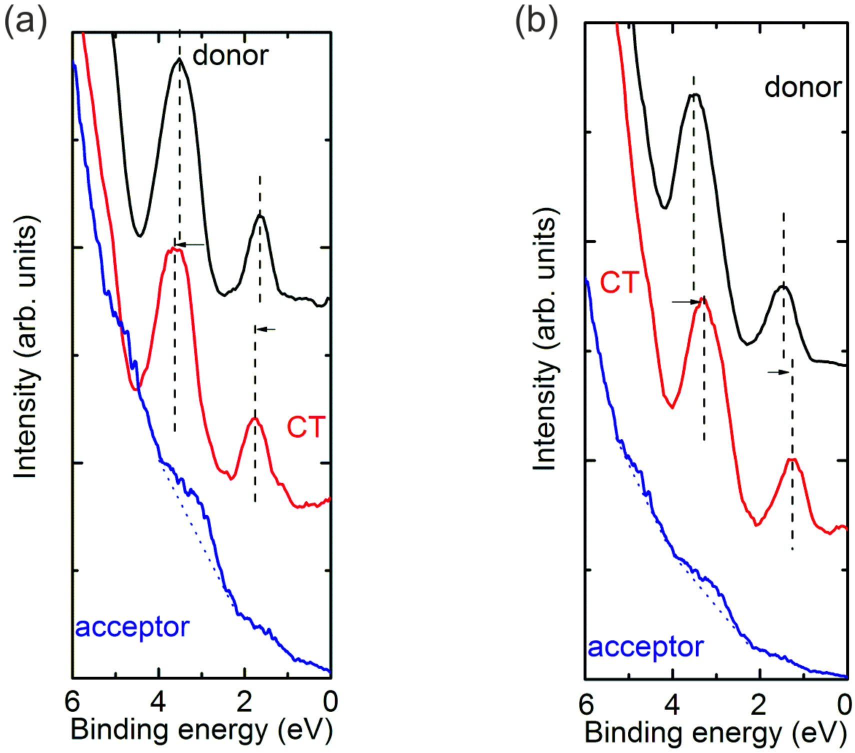

Figure A-1.13. He I UPS spectra of the charge transfer complexes triangulene-HATCN (left) and trimethoxy triangulene- HATCN (right) on Au. Bottom spectra show the signal from the pure acceptor, the top spectra were taken for the pure donor and the center spectra were taken during layer-by-layer deposition of the donor and acceptor.

Comparison of charge transfer properties in complexes based on triangulenes

The systematic investigation and comparison of the charge transfer mechanisms in the novel class of triangulene donors with three different acceptors reveal interesting spectroscopic features that are summarized in Table A-1.1.

Trimethoxy triangulene shows a constant value of 400 meV for the HOMO shift for mixtures with both F_4TCNQ and TCNQ acceptors as a result of complete or almost complete charge transfer, and a 200 meV shift for the mixture with HATCN being an indication of partial charge transfer. This is in agreement with values of E_A and I_D for the acceptors and the trimethoxy triangulene donor, respectively.

Table A-1.1. Experimental energy shifts of the HOMO levels in triangulene compounds as revealed by ultraviolet photoelectron spectroscopy. Values of ionization potentials of donors are taken from cyclovoltammetry performed at MPI-P, while the electron affinity values of the acceptors are taken from [174], [197].

	F_4TCNQ (E_A = -5.24 eV)	TCNQ (E_A = -4.82 eV)	HATCN (E_A = -4.60 eV)
Tria (I_D = 4.96)	150 meV → (full CT)	340 meV →	110 meV ←
Ome (I_D = 4.86)	400 meV → (full CT)	400 meV → (full CT)	200 eV→

Triangulene shows a shift of the HOMO of 150 meV to higher binding energies for the mixture with F_4TCNQ, a shift of 340 meV also to higher binding energies for the mixture with TCNQ, and a shift of 110 meV to lower binding energies for the mixture with HATCN.

As a possible outlook for this topic, two main points should be taken into account. First of all, theoretical calculations are very important and will allow valuable discussions on the origins of peak shifts, filling of molecular orbitals, and the non-trivial dependence of the electronic shift as a function of acceptor strength. Secondly, NEXAFS investigations on thin films of mixtures with TCNQ and HATCN are absent because of the low stability of the mixed compounds. The complex NEXAFS study on these thin films performed were unsuccessful because the films re-sublimated too fast in UHV. Hence, *in-situ* preparation of the investigated materials is required and measurements must be done immediately after film deposition.

Appendix 2

Donor-acceptor interaction in 1D organic conductors

Some more investigations were performed in the framework of a very fruitful collaboration with Dr. K. Medjanik (MAX II Laboratory, Lund), Prof. Dr. J.-P. Pouget (University Paris-Sud) and Prof. Dr. E. Canadell (University of Barcelona). This topic is of high interest because it shows experimentally the complicated nature of the electronic structure of organic conductors with mixing of donor and anion components in the molecular orbitals. Since this research was not the central part of the present Thesis, the main results and conclusions are listed in this Appendix. The full extended version of the discussion is published in [11] and [198].

Fabre and Bechgaard salts

The Fabre and Bechgaard salts $(TMTTF)_2X$ and $(TMTSF)_2X$, where TMTTF is tetramethyltetrathiafulvalene, TMTSF is tetramethyltetraselenafulvalene and X = PF_6, AsF_6, ClO_4, NO_3 are among the most typical examples of organic 1D conductors whose electronic properties can be tuned by changing the TMTTF/TMTSF nature of the donor, the monovalent anion X (meaning applying a “chemical pressure” to the crystal) or by applying an external physical pressure [199]. The general phase diagram of these two classes of quasi-one-dimensional organic conductors was discussed in Chapter 2.1.1. (see also

Fig. 2.6). The work reported here was focused on two examples of the Fabre and Bechgaard family, $(TMTTF)_2AsF_6$ and $(TMTSF)_2PF_6$ (see Fig. A-2.1), synthesized in the group of Prof. Dr. J.-P. Pouget.

$(TMTTF)_2X$ salts exhibit a continuous electron localization upon cooling which manifests by the onset of an activated conductivity below $T_\rho \approx 200 - 250$ K. For the $(TMTTF)_2AsF_6$ compound the charge localization transition temperature is 230 K. There is one more transition occurring being due to symmetry breaking - charge ordering (CO). $(TMTTF)_2AsF_6$ crystals exhibit a CO transition at $T_{CO} = 102$ K and it has an insulating ground state [1].

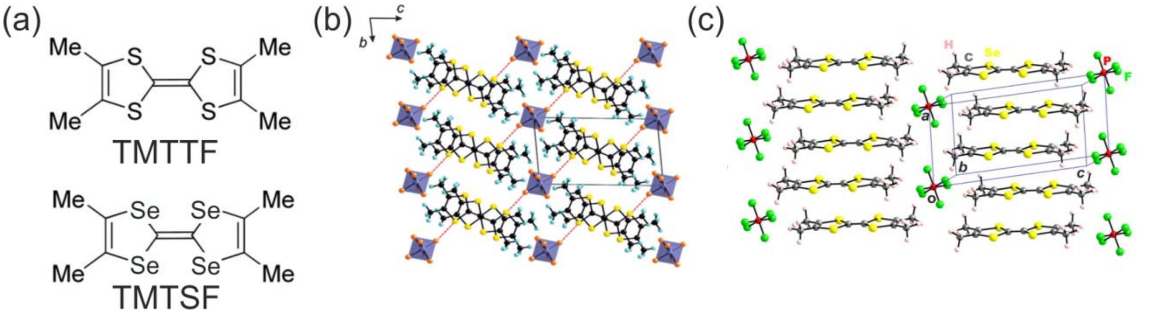

Figure A-2.1. (a) Molecular structure of TMTTF and TMTSF donors. (b) Centro-symmetric structure of $(TMTTF)_2AsF_6$ projected along the *a* stacking direction. The short S⋯F contact distances are also indicated as orange dashed lines. (c) Quasi-planar organic molecule stack of TMTSF along the *a*-axis separated by PF_6 anions in the *c**-direction.

In the TMTSF salts, the interstack interaction is stronger than in the TMTTF salts. This is because the shortest Se-Se distance along the *b*-axis in the TMTSF family is less than twice the van der Waals radius of the Se atoms, whereas in the TMTTF family the shortest S-S distance along the *b*-axis is more than twice the van der Waals radius of the sulfur atoms. For this reason, TMTTF based salts are more 1D than the TMTSF based salts [200].

In the $(TMTSF)_2PF_6$ compound a Tomonaga-Luttinger liquid phase [201] was found at high temperatures due to the 1D nature of the electronic overlaps and to the presence of sizeable electron-electron repulsions. Upon cooling, the electronic structure exhibits a 1D to 2D dimensional crossover around 100 K [202] which results in a de-confinement of the wave function in the *b* direction due to the sizeable overlap of the Se wave functions in the inter-stack directions. Upon further cooling the high temperature reorientation jump of the anion inside the methyl group cavities and the methyl group disorder progressively vanish

[203]. Then $(TMTSF)_2PF_6$ undergoes a spin density wave metal-insulator transition at 12 K stabilized by the nesting of its quasi-1D Fermi surface. Upon pressure the nesting condition deteriorates, the metallic state is restored and finally $(TMTSF)_2PF_6$ exhibits a superconducting ground state below about 1 K [204].

Temperature-dependent NEXAFS on $(TMTTF)_2AsF_6$

Two $(TMTTF)_2AsF_6$ single crystals were studied at MAX II, Lund, Sweden (beamline I1011) by NEXAFS spectroscopy [145]. Fig. A-2.2 (a) shows NEXAFS spectra taken at the sulfur L-egde of TMTTF. The deconvolution of the S 2p NEXAFS spectra gives four prominent resonances, observed at room temperature. Fig. A-2.2 (b) presents F K-edge spectra at different temperatures. The signal is clearly composed of four peaks at room temperature, labelled 1 to 4, with increasing photon energy.

In the present work the calculations were carried out using a numerical atomic orbitals density functional theory (DFT) approach [99], [148] which was developed for efficient calculations in large systems and implemented in the SIESTA code [205].

Comparison of the experimental results with calculated density of states (Fig. A-2.3) leads to the assignment of sulfur NEXAFS spectra as follows: peak 1 to the TMTTF a_g σ^* orbital, peak 2 to the three π^* orbitals b_{3g}, a_u and b_{2g}, peak 3 to the b_{3u} and the lower b_{2u} σ^* orbitals, and finally peak 4 to the upper σ^* b_{2u} orbital. The fluorine NEXAFS spectra has an assignment as follows: peak 1 is due to the AsF_6^- LUMO (at ~2.4 eV) and peak 3 (around 5.5 eV higher in energy) originating from the group of three nearly degenerate AsF_6^- LUMO+1/LUMO+2/LUMO+3 orbitals. Peaks 2 and 4 of the F 1s spectra are due to the interaction of the set of LUMO+1/LUMO+2/LUMO+3 orbitals of AsF_6^- with the S d_{z^2}, d_{xz} and d_{yz} orbitals (peak 2) and S $d_{x^2-y^2}$ and d_{xy} orbitals (peak 4) of TMTTF.

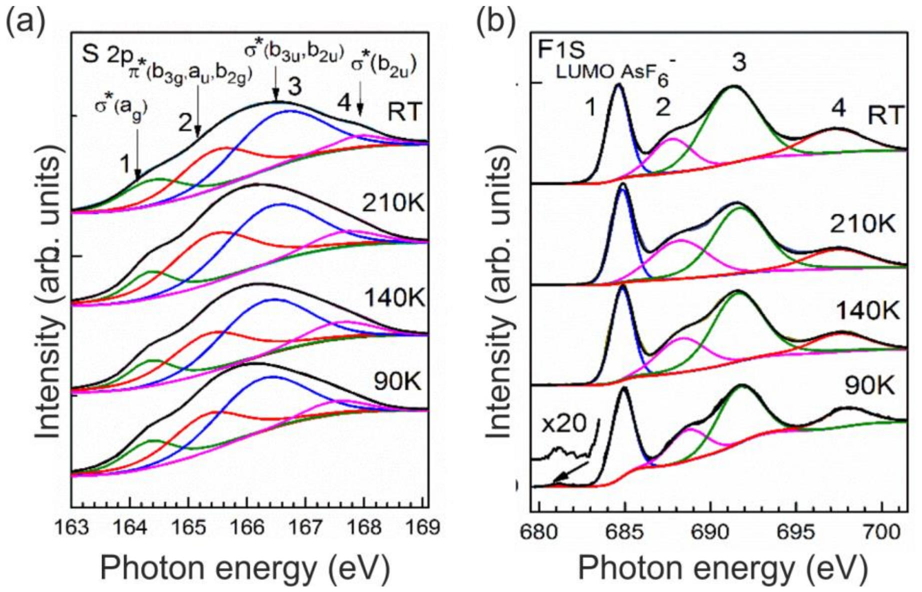

Figure A-2.2. (a) Sulfur 2p and (b) fluofine 1s NEXAFS spectra of $(TMTTF)_2AsF_6$ taken at room temperature, 210, 140 and 90 K in normal incidence. Each spectrum is deconvoluted using a multi-peak fit routine.

Peaks in the S 2p spectra exhibit a negative shift with cooling whereas those of the F 1s spectra are positively shifted. This clearly points to a definite increase in the interaction between the empty levels of the TMTTF and AsF_6^-. The energy shifts measure the mixing between levels of the two partners whereas the intensities probe the relative weight of orbitals of different components.

The intensity of peak 1 in the F 1s spectra does not change significantly above T_{CO} (Fig. A-2.2) which indicates that the orbital mixing into the AsF_6^- LUMO does not really change. From room temperature to T_ρ the main changes are the negative shifts of all peaks in the S 2p spectra and a positive shift of all peaks in the F 1s spectra (Fig. A-2.2). There is also a sizeable increase of the intensity of peak 2 in the F 1s spectra compensated by smaller decrease of intensity of peaks 1, 3 and 4. After a strong change around the charge localization transition, the evolution of the relative intensity peaks of the S 2p spectra looks as if they were trying to recover the situation at RT. Below T_ρ the continuous increase of the donor-anion interactions leads to a larger mixing of the orbitals of the two systems and thus to a progressive decrease of the participation of the sulfur orbitals in the TMTTF levels. Consequently, the evolution of the relative peak intensity should go in the opposite direction before and after T_ρ. When the CO transition occurs, the donor-anion interactions still increase while there is a significant charge disproportionation between the two TMTTF donors [206].

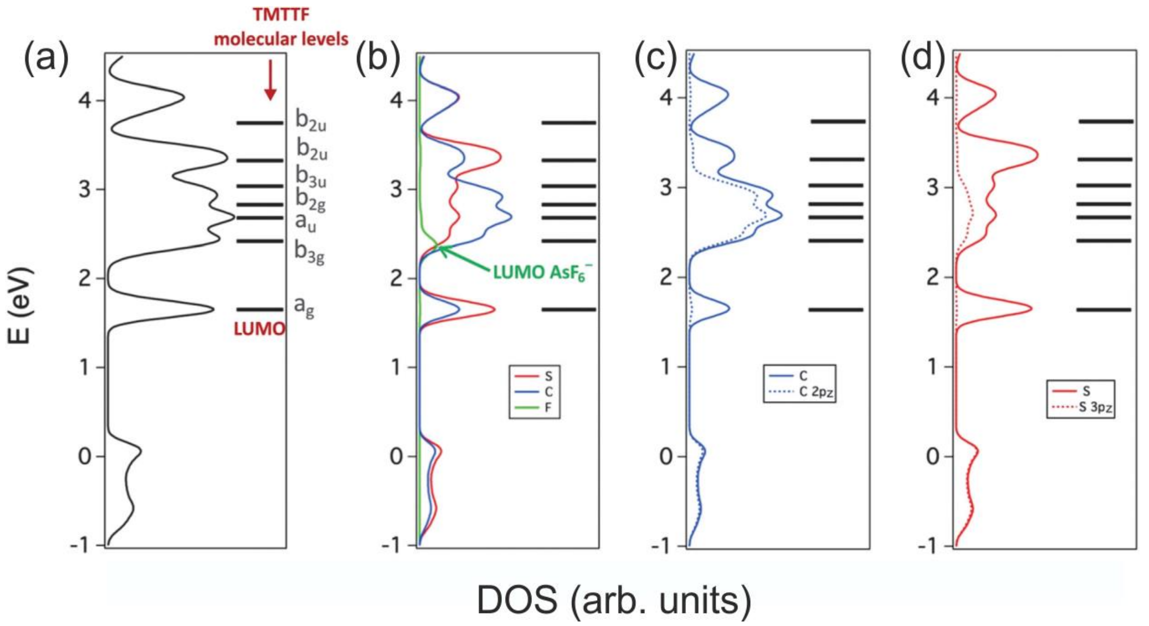

Figure A-2.3. Total DOS (a) and local projections (PDOS) of the contributions of the sulfur, carbon and fluorine atoms (b) as well as π-type contribution (dotted line) for the carbon (c) and sulfur (d) atoms in $(TMTTF)_2AsF_6$.The molecular energy levels of TMTTF are also included.

To summarize, the temperature evolution of the energy shifts and peak intensities are consistent with a continuous increase of the donor-anion interactions, mostly through the F⋯S contacts, as well as with a substantial mixing of the sulfur d-type orbitals on the unoccupied π* and σ* empty molecular orbitals of TMTTF.

Temperature-dependent NEXAFS on $(TMTSF)_2PF_6$

These experiments were performed at the same conditions as in the previous case at the I1011 beamline of the MAX II storage ring and discussed in comparison to theoretical calculations, performed in a similar manner as in the previous sub-chapter.

The C 1s spectra exhibit three distinctive peaks. The first one (labeled 1 in Fig. A-2.4, a) is assigned to the σ-type LUMO of TMTSF. Peaks 2 and 3 both contain σ- and π-type TMTSF contributions. Peak 2 is dominated by the σ-type states and the third one is dominated by the π-type states. Some more information on the σ and π type contributions is represented in Fig. A-2.5. The π levels tend to concentrate in the lower energy levels when the temperature decreases. This provides a simple rationalization for the intensity increase of peak 2 which according to the θ dependence should be dominated by σ levels at room temperature. For the same reason, the intensity decrease of peak 3, which according to the θ dependence should be dominated by π levels at room temperature, is easily understandable. Consequently, it could be suggested that the σ- and π-type levels associated with the LUMO+1 to LUMO+5 of TMTSF experience a complex redistribution as a function of temperature, something which strongly contrasts with the case of the $(TMTTF)_2AsF_6$ salt [11]. In the latter case the nature of the different peaks remains constant for all temperatures even if the intensity evolves as a result of the charge localization phenomenon and the charge ordering transition.

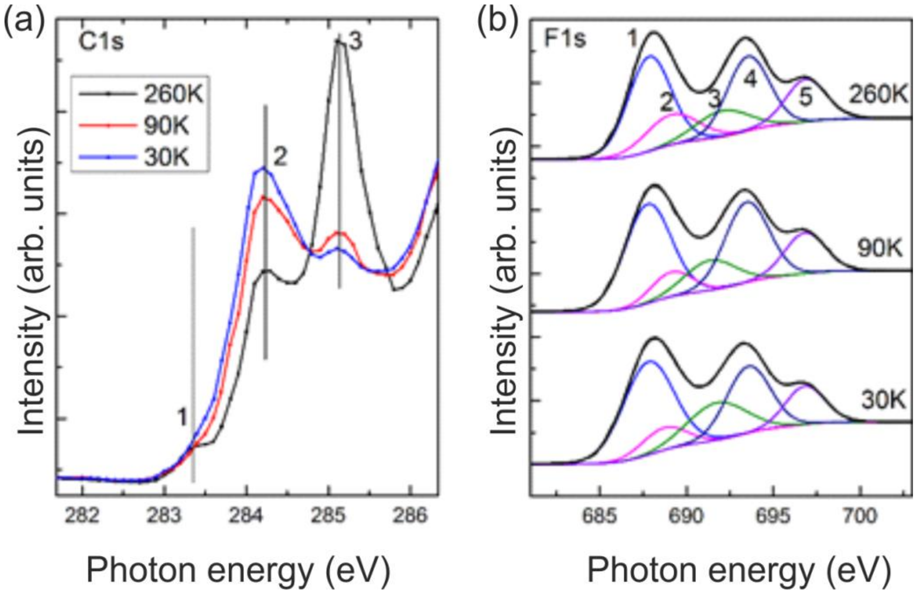

Figure A-2.4. Carbon 1s (a) and fluorine 1s NEXAFS spectra of $(TMTSF)_2PF_6$ (b) taken at 260, 90 and 30 K in the normal incidence. Each spectrum is deconvoluted using a multi-peak fit routine.

The temperature dependence of the F 1s spectrum is shown in Fig. A-2.4, b. The deconvolution reveals five pronounced peaks which are labeled from 1 to 5 with increasing energy. Although the shape of these orbitals is very similar to those previously reported for the AsF_6^- anion [11], the energy separation between the LUMO and LUMO+i orbitals is now around 3.1 eV whereas for AsF_6^- the difference obtained with the same computational approach was found to be considerably larger, 4.8 eV. This observation is in agreement with the fact that in our previous work concerning $(TMTTF)_2AsF_6$ peaks 1 and 3 of the F 1s spectra, which were separated by 6.8 eV, were attributed to the LUMO and LUMO+i levels of the anion. In the present case (see Fig. A-2.4) these levels are associated with peaks 1 and 4 and now the separation is noticeably smaller, only 5.2 eV. The larger separation found for the AsF_6^- anion is mostly due to the more extended nature of the As orbitals which overlap better with the F 2p orbitals leading to a larger splitting

Comparison of the experimental results with DFT calculations reveals two main features. First, no phosphorous or fluorine levels occur within the whole energy range of the LUMO to LUMO+6 levels of TMTSF. This means that the LUMO of PF_6^- is located at higher energies. This is very different from the case of $(TMTTF)_2AsF_6$ where the LUMO of AsF_6 was practically aligned with the LUMO+1 of the donor. The origin of this important difference is that the *d* orbitals of selenium are considerably more spread and thus the interaction between the TMTSF and PF_6^- molecular orbitals is considerably stronger so that the PF_6^- levels are pushed quite high in energy. Second, there is not a clear separation between σ and π levels of TMTSF.

The replacement of selenium for sulfur in the molecular network of the TMTTF donors leads to a strong intermingle of σ and π type components of the molecular levels in the region of the LUMO+1 to LUMO+5 orbitals, i.e. those responsible for the stronger peaks in the C 1s spectra. Since the geometry of the TMTSF donor varies with temperature, the proportion of the two components may change in the spectra at different temperatures. Since the temperature variation may affect both the separation of the different levels and the mixing of σ and π components, it is difficult to have some guideline to understand the temperature evolution of the C 1s spectra (Fig. A-2.4).

An important difference with the $(TMTTF)_2AsF_6$ salt is that the first peak of the F 1s spectra occurs now around 3 eV higher in energy. This behavior is quite different from that found in the $(TMTTF)_2AsF_6$ salt. In the present case there is a very broad and continuous contribution of the PF_6 projected DOS with two peaks centered at around 6.6 and 10.2 eV. The contribution of the LUMO+i levels was also found quite broad for $(TMTTF)_2AsF_6$ but the contribution of the LUMO was found to be narrow. In addition, the lower peak is centered now at around 6.6 eV from the Fermi level which is approximately 4 eV higher than in $(TMTTF)_2AsF_6$ (see Fig. 7b in [198]). This is in good agreement with the above mentioned shift of the first peak in the F 1s spectra of the two salts.

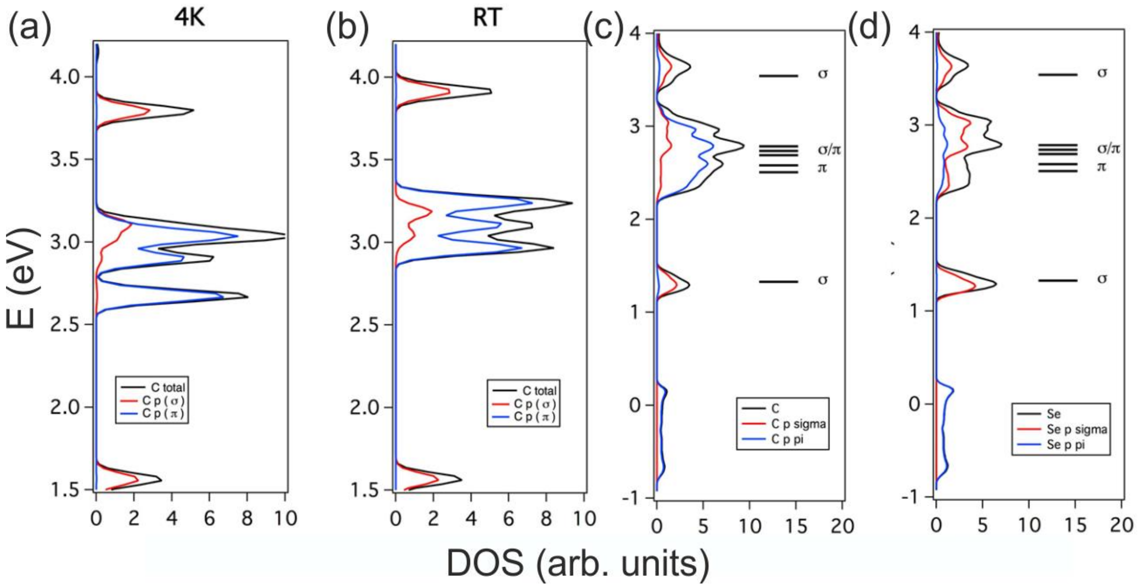

Figure A-2.5. Projection of the *σ*- (red) and *π*- (blue) contributions of the 2*p* orbitals of carbon to the DOS of discrete TMTSF levels calculated using the crystal structure of $(TMTSF)_2PF_6$ at 4K (a) and room temperature (b). Energies (in eV) are relative to the energy of the HOMO. Decomposition of the contributions of the carbon (c) and selenium (d) to the DOS of $(TMTSF)_2PF_6$ into *σ*- (red) and *π*- (blue) type components are also shown. The molecular energy levels of TMTSF are included.

The chalcogen *d* orbital contribution is considerably stronger than it was in the $(TMTTF)_2AsF_6$ salt. The important observations from this are: (i) there is Se *d* orbital participation in all donor empty levels, and (ii) all along the DOS region with F contributions there is also Se *d* orbital participation. This means that there is a strong interaction between donor and anion empty levels mostly mediated by the F 2*p*-Se 4*d* interactions through the short F···Se contact distances. The first consequence of this strong interaction is that the LUMO and LUMO+i orbitals of the anion are pushed to considerably higher energies than in $(TMTTF)_2AsF_6$, as clearly shown by the F 1s spectra. The second consequence is that both the LUMO and LUMO+i levels become very broad leading to a continuous contribution of more than 10 eV as probed in the F 1s spectra. Hence the de-convolution of the F 1s spectra into a series of broad contributions shows that the main peaks 1 and 4 are centered at the LUMO and LUMO+i levels, whereas weaker peaks 2, 3 and 5 essentially describe the large broadening of these levels because of the F 2*p*-Se 4*d* interactions.

The evolution of the different peaks would not be as informative as it was in the case of $(TMTTF)_2AsF_6$ [11] because of the strong TMTSF-PF_6 interaction leading to a large mixing of levels. However, the more distinctive features of F 1s NEXAFS spectra are: (i) the stronger variations of both relative intensity and shift are those of peaks 2 and 3 describing the TMTSF-PF_6 interaction in between the two main peaks 1 and 4, (ii) the shifts of all other peaks increase when the temperature is lowered because the interactions increase with thermal contraction, and (iii) both relative intensity and shift of peaks 2 and 3 exhibit an opposite evolution. All these observations are consistent with the above description of the F 1s spectra with two main contributions, peak 1 (LUMO) and peak 4 (LUMO+i), showing a ”normal” evolution with temperature and a broad region in between them, including peaks 2 and 3 associated with the large mixing of donor-anion levels through the F 2*p*-Se 4*d* interactions.

Summary

Despite the structural similarity the NEXAFS spectra of $(TMTSF)_2PF_6$ and $(TMTTF)_2AsF_6$ exhibit remarkable differences.

The charge localization phenomenon and the CO transition of $(TMTTF)_2AsF_6$ correspond to subtle changes in the electronic structure. The strongest effect was observed for the fluorine and sulfur atomic species exhibiting systematic shifts of the F 1s and S 2p lines up to +0.85 eV and -0.4 eV, respectively. Remarkably, these photon energy shifts occur in opposite directions with respect to the RT spectra The opposite shifts found in the F 1s and S 2p spectra reflect substantial changes in the electronic environment of the sulfur atoms of TMTTF and the fluorine atoms of the anions. The changes observed below T_ρ suggest an increase of participation of the S *d* orbitals in the empty states of TMTTF as well as an increase of the donor-anion interactions. The appearance of a new F 1s pre-edge signal upon entry into the CO phase at 90 K is a fingerprint of the charge disproportionation. The data suggest that the loss of the inversion center associated with the CO transition is due to an anionic displacement towards the sulfur atom of the hole-rich TMTTF.

In case of $(TMTSF)_2PF_6$ a significant change of the relative intensity of the C K-edge transitions upon cooling was found and has been accounted for on the basis of subtle relative energy variations of the unoccupied donor levels. This effect corresponds to an unexpected thermal dependence of the DFT density of states and results from a delicate modification of the σ /π empty orbitals mixing associated with the non-planarity variation of the TMTSF donors. This effect does not play a visible role in the case of $(TMTTF)_2AsF_6$. Sizeable energy shifts of the different F K-edge components upon cooling from RT are also observed, as previously found in $(TMTTF)_2AsF_6$. They correspond to an increase of the mixing of donor-anion levels through an enhancement of F 2p - Se 4d interactions upon cooling as a result of the lattice contraction.

Appendix 3

Estimation of the charge-transfer amount in organic complexes

When novel charge transfer complexes are being synthesized, the classical way of several steps is needed to characterize the unknown properties. First of all, the crystal structure has to be investigated. It will give the starting point for theoretical calculations and discussions. For the electronic structure investigation, a “nice to have” information is the amount of charge transfer between donor and acceptor molecules in the crystal. As it was shown in Chapter 6, a NEXAFS investigation together with IR-spectroscopy allow to discuss the mechanism of the charge transfer in organic compounds. This Appendix is dedicated to one more very fruitful collaboration with Antonia Morherr (group of Prof. Dr. Cornelius Krellner, University Frankfurt (M)). In more details this topic is available in [207]. Since the main work was done by A. Morherr, here only the IR investigation of the charge transfer amount is represented.

Several novel charge transfer complexes based on the phenanthrene (PHN) donor molecule were obtained by physical vapor transport [207]. As anionic counter-ion three different acceptors of one family with gradually increasing acceptor strength were used: TCNQ, F_2TCNQ and F_4TCNQ. According to the simplest assumptions, the amount of the transferred charge is proportional to the acceptor strength and, therefore, should increase in the sequence PHN-TCNQ << PHN- F_2TCNQ << PHN-F_4TCNQ.

Infrared spectroscopy was measured on polycrystalline samples of PHN-TCNQ, PHN- F_2TCNQ and PHN-F_4TCNQ and compared to spectra recorded from powders of pure acceptors TCNQ, F_2TCNQ and F_4TCNQ, respectively. Spectra were obtained using Nicolet 730 FT-IR spectrometer[13] between 4000 and 500 cm^{-1} at room temperature. Resolution of the measurements was 1 cm^{-1}.

Infrared spectroscopy is a very convenient experimental technique for the estimation of the charge transfer due to the linear dependence between the frequency shift of the C≡N stretching mode and the transferred charge. The charge transfer is calculated using the equation (6.2) [161]. This equation has been applied for both TCNQ and F_4TCNQ acceptors, and some other molecules [162], [149], [163].

Figure A-3.1 shows the IR spectra for three measurements of novel compounds, described above. Table A-3.1 summarizes the obtained results and lists also the reference values necessary for calculations.

Table A-1.1. Frequency shifts of the C≡N stretching mode for investigated samples PHN-TCNQ, PHN- F_2TCNQ and PHN-F_4TCNQ and the transferred charge, calculated using eq.(A-1).

	PHN-TCNQ	PHN- F_2TCNQ	PHN-F_4TCNQ
ω_0 (cm^{-1})	2222.7	2229.5	2227.7
ω_1 (cm^{-1})	2186.0 [149]	2186.0 [165]	2190.0 [165]
ω_{CT} (cm^{-1})	2214.6	2218.2	2225.4
CT	0.22 *e*	0.26 *e*	0.05 *e*

---

[13] The spectrometer for these study was kindly provided by Max-Planck Institute for Polymer Research.

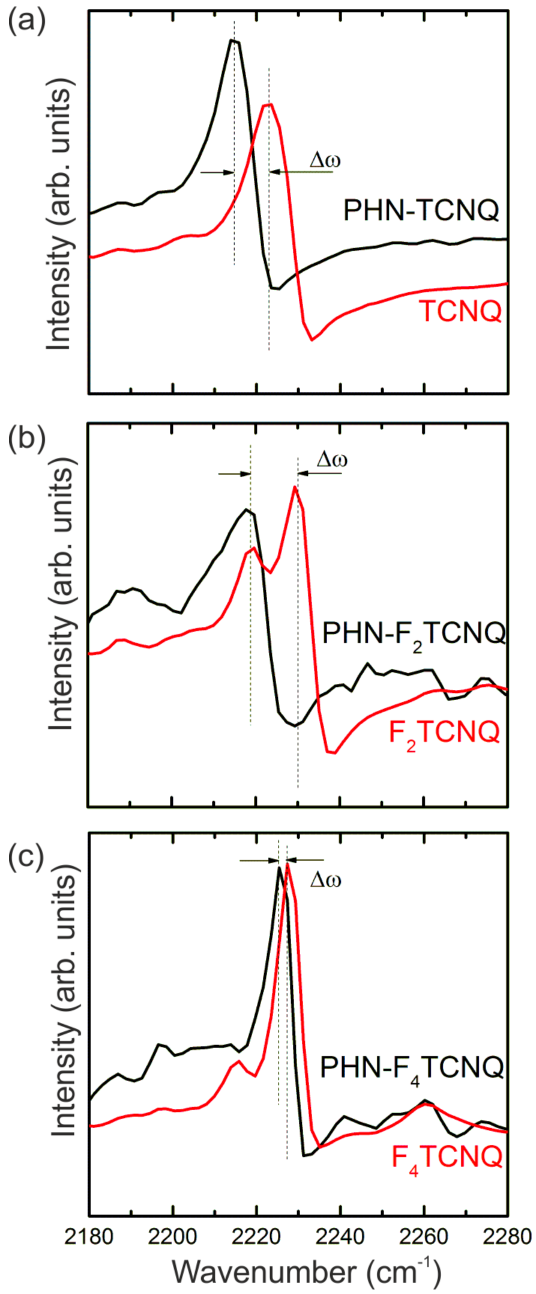

Figure A-3.1. IR spectra of polycrystalline samples in the C≡N stretching mode region for phenanthrene-TCNQ (a), phenanthrene-F_2TCNQ (b) and phenanthrene- F_4TCNQ (c) salts. The C≡N stretching vibrations is always red-shifted in the case of charge transfer compounds, compared to the pure acceptors.

Similarly to the DTBDT case, discussed in Chapter 6 and the example of the TMP family [139] (where TMP = tetramethoxypyrene), charge transfer complexes based on phenanthrene do not always hold the assumption about the direct proportionality between charge transfer and frequency shift of the C≡N stretching mode in IR spectroscopy.

The observed non-linear dependence of the charge transfer amount as a function of the acceptor strength could be caused by (i) structural aspects, meaning obstructed molecular orbitals overlapping due to molecular screening or (ii) a complicated charge transfer mechanism with local charge disproportionation inside the acceptor molecule due to strongly involved fluorine atoms suppressing the aromatization of the central part of the TCNQ molecule.

List of abbreviations and symbols

1D	One-dimensional
2D	Two-dimensional
2PPE	Two-photon photoelectron spectroscopy
3D	Three-dimensional
A	Acceptor
a	Interplanar distance
AC	Alternating current
AF	Antiferromagnetic
AFI	Antiferromagnetic insulator
ARPES	Angular-resolved photoelectron spectroscopy
BEDT-TTF	Bis(ethylenedithio)tetrathiafulvalene
BOW	Bond ordering wave
CA	Tetrachloro-p-benzoquinone
CDW	Charge density wave
CO	Charge ordering
CT	Charge transfer
C	Curie constant
D	Donor
DC	Direct current
DFT	Density functional theory
DOEO	1,4-(dioxanediyl-2,3-dithio)ethylenedioxotetrathiafulvalene
DOS	Density of states
DTBDT	Dithieno[2,3-d;2’,3’-d’]benzo[1,2-b;4,5-b’]dithiophene
E	Energy

e	Charge of electron
E_A	Electron affinity
E_B	Binding energy
E_F	Fermi energy
ESCA	Electron spectroscopy for chemical analysis
ESR	Electron spin resonance
E_{vac}	Vacuum energy level
I_D	Ionization potential
FWHM	Full width at half-maximum
g	g-factor
TSF	Tetraselenafulvalene
TMTTF	Tetramethyltetrathiafulvalene
HMTSF	Hexamethylene-tetraselena-fulvalene
F_4TCNQ	Tetrafluoro-tetracyanoquinodimethane
H	Magnetic field
H	Hamiltonian
H_c	Critical field
HAXPES	Hard X-ray photoelectron spectroscopy
IMFP	Inelastic mean free path
IR	Infra-red
k	Momentum
k_B	Boltzmann constant
M	Madelung energy
M	Magnetic field
MD	Mott-dimer
n	Charge carrier density
N	Number of electrons in the band
NI	Neutral-ionic transition
NEXAFS	Near-edge X-ray absorption fine structure
OFET	Organic field-effect transistor
OLED	Organic light emitting diod
OPV	Organic photovoltaic cell
p	Base pressure in the ultra-high vacuum chamber

PDOS	Partial density of states
PES	Photoelectron spectroscopy
PLD	Periodic lattice distortion
R	Resistivity
S	Spin
SDW	Spin density wave
SC	Superconductor
STM	Scanning tunneling microscopy
STS	Scanning tunneling spectroscopy
SP	Spin-Peierls phase
SQUID	Superconducting quantum interference device
T	Temperature
t	Intermolecular transfer integral
T_c	Critical temperature
TCE	1,1,2-trichloroethane
UHV	Ultra-high vacuum
UPS	Ultra-violet photoelectron spectroscopy
V_{ij}	Long-range Coulomb repulsion
W	Bandwidth
XANES	X-ray absorption near-edge structure
XPS	X-ray photoelectron spectroscopy
Δg	Energy gap
$\hbar$	Planck’s constant
χ	Magnetic susceptibility
θ	Curie temperature
ω	Vibration frequency
μ	Carrier mobility
υ	Amount of material
τ	Relaxation time
Φ	Work function

Bibliography

[1] D. Jerome, H.J. Schulz, "Organic conductors and superconductors," *Advances in Physics*, vol. 51, pp. 293-479, 2002.

[2] F. Kagawa, K. Miyagawa, K. Kanoda, "Magnetic Mott criticality in a k-type organic salt probed by NMR," *Nature Physics*, vol. 5, pp. 880-884, 2009.

[3] J.-P. Pouget, "Structural aspects of the Bechgaard and Fabre salts: an update," *Crystals*, vol. 2, pp. 466-520, 2012.

[4] K. Yamamoto, A. Kowalska and K. Yakushi, "Direct observation of ferroelectric domains created by Wigner crystallization of electrons in α-[bis(ethylenedithio)tetrathiafulvalene]2I3," *Appl. Phys. Lett.*, vol. 96, p. 122901 , 2010.

[5] S. Iwai, K. Yamamoto, F. Hiramatsu, H. Nakaya, Y. Kawakami, and K. Yakushi, "Hydrostatic pressure effect on photoinduced insulator-to-metal transition in the layered organic salt α−(BEDT−TTF)2I3," *Phys. Rev. B*, vol. 77, p. 125131, 2008.

[6] G. Saito, "Multifunctional Molecular Conductors," *Eur. J. Inorg. Chem.*, pp. 3785-3788, 2014.

[7] T. Isono, H. Kamo, A. Ueda, K. Takahashi, M. Kimata, H. Tajima, S. Tsuchiya, T. Terashima, S. Uji, H. Mori, "Gapless Quantum Spin Liquid in an Organic Spin-1/2 Triangular-Lattice κ−H3(Cat-EDT-TTF)2," *Phys. Rev. Lett.*, vol. 112, p. 177201, 2014.

[8] R. Shibaeva, E. Yagubskii, "Molecular Conductors and Superconductors Based on Trihalides of BEDT-TTF and Some of Its Analogues," *Chem. Rev.*, vol. 104, p. 5347, 2004.

[9] D. Jérome, "Organic Superconductivity: A Mouse may be of Service to a Lion," in *Superconductivity in New Materials*, Elsevier, 2011, pp. 149-216.

[10] P. Lunkenheimer, J. Müller, S. Krohns, F. Schrettle, A. Loidl, B. Hartmann, R.Rommel, M. de Souza, C. Hotta, J. A. Schlueter, M. Lang, "Multiferroicity in an organic charge-transfer salt that is suggestive of electric-dipole-driven magnetism," *Nature Materials*, vol. 11, pp. 755-758, 2012.

[11] K. Medjanik, A. Chernenkaya, S. A. Nepijko, G. Öhrwall, P. Foury-Leylekian, P. Alemany, E. Canadell, G. Schönhense and J.-P. Pouget, "Donor–anion interactions at the charge localization and charge ordering transitions of (TMTTF)2AsF6 probed by NEXAFS," *Phys. Chem. Chem. Phys.*, vol. 17, pp. 19202-19214, 2015.

[12] K. Medjanik, M. de Souza, D. Kutnyakhov, A. Gloskovskii, J. Müller, M. Lang, J.-P. Pouget, P. Foury-Leylekian, A. Moradpour, H. J. Elmers and G. Schönhense, *European Phys. J. B*, vol. 87, p. 256, 2014.

[13] W.A. Little, "Possibility of Synthesizing an Organic Superconductor," *Phys. Rev. A*, vol. 134, p. 1416, 1964.

[14] T. J. Kistenmacher, T. E. Philips, and D.O. Cowan, "The crystal structure of the 1:1 radical cation–radical anion salt of 2,2'-bis-l,3-dithiole (TTF) and 7,7,8,8-tetra-cyanoquinodimethane (TCNQ)," *Acta Cryst. B*, vol. 30, p. 763, 1974.

[15] G. Saito, Y. Yoshida, "Development of conductive organic molecular assemblies: organic metals, superconductors, and excitonic functional materials," *Bull. Chem. Soc. Jpn.*, vol. 80, no. 1, pp. 1-137, 2007.

[16] K. P. Goetz, D. Vermeulen, M. E. Payne, C. Kloc, L. E. McNeil and O. D. Jurchescu, "Charge-transfer complexes: new perspectives on an old class of compounds," *J. Mater. Chem. C*, vol. 2, pp. 3065-3076, 2014.

[17] D. P. Goswami and M.L. Kaira, "A new approach to molecular synthesis and crystal growth of one-dimensional organic charge transfer complex TTF—TCNQ," *Journal ofCrystal Growth*, vol. 135, pp. 196-198, 1994.

[18] M. D. Ward, D. C. Johnson, "Electrocrystallization and structural and physical properties of charge-transfer complexes derived from [(.eta.6-C6Me6)2M]2+ (M = Fe, Ru) and TCNQ (TCNQ = tetracyanoquinodimethane)," *Inorg. Chem.*, vol. 26, pp. 4213-4227, 1987.

[19] O. Kataeva, M. Khrizanforov, Y. Budnikova, D. Islamov, T. Burganov, A. Vandyukov, K. Lyssenko, B. Mahns, M. Nohr, S. Hampel, and M. Knupfer, "Crystal Growth, Dynamic and Charge Transfer Properties of New Coronene Charge Transfer Complexes," *Cryst. Growth Des.*, vol. 16, pp. 331-338, 2016.

[20] I. Shokaryev, A. J. C. Buurma, O. D. Jurchescu, M. A. Uijttewaal, G. A. de Wijs, T. T. M. Palstra, and R. A. de Groot, "Electronic Band Structure of

Tetracene−TCNQ and Perylene−TCNQ Compounds," *J. Phys. Chem. A*, vol. 112, pp. 2479-2502, 2008.

[21] K. Medjanik, S. Perkert, S. Naghavi, M. Rudloff, V. Solovyeva, D. Chercka, M. Huth, S. A. Nepijko, C. Felser, M. Baumgarten, K. Müllen, H. J. Elmers, G. Schönhense, "Formation of an intermolecular charge-transfer compound in UHV codeposited tetramethoxypyrene and tetracyanoquinodimethane," *Phys. Rev. B*, vol. 82, p. 245419, 2010.

[22] T. Ishiguro, K. Yamaji, G. Saito, Organic superconductors, Berlin Heidelberg: Springer-Verlag, 1989.

[23] N. Thorup, G. Rindorf, H. Soling and K. Bechgaard, "The structure of di(2,3,6,7-tetramethyl-1,4,5,8-tetraselenafulvalenium) hexafluorophosphate, (TMTSF)2PF6, the first superconducting organic solid," *Acta Cryst.*, vol. 37, pp. 1236-1240, 1981.

[24] D. Jerome, "Organic superconductors: when correlations and magntism walk in," *J. Supercond. Nov. Magn.*, vol. 25, pp. 633-655, 2012.

[25] N Toyota, M. Lang, J. Mueller, Low-dimensional molecular metals, Springer, 2007.

[26] S.S.P. Parkin, E.M. Engler, R.R. Schumaker, R. Lagier, V.Y. Lee, J. Voiron, K. Carneiro, J.C. Scott and R.L. Greene , "A sulphur based organic molecular superconductor: (BEDT-TTF)4(Re04)2," *J. Phys. Colloques*, vol. 44, pp. C3-791-C3-797, 1983.

[27] E. B. Yagubskii, I. F. Shchegolev, V. N. Laukhin, P. A. Kononovich, M. V. Kartsovnik, A. V. Zvarykina, L. I. Buravov, "Normal-pressure superconductivity in an organic metal (BEDT-TTF)2I3 [bis (ethylene dithiolo) tetrathiof ulvalene triiodide]," *J. Exper. Theor. Phys. Lett.*, vol. 38, p. 12, 1984.

[28] K. Kanoda, "Recent progress in NMR studies on organic conductors," *Hyperfine Interact.*, vol. 104, pp. 235-249, 1997.

[29] K. Kikuchi, S. Ikeda, H. Nishikawa, T. Kodama, I. Ikemoto, J. Yamada, "Oxygen and selenium substituted derivatives of DOET donor: synthesis and properties," *Synthetic Metals*, vol. 120, pp. 901-902, 2001.

[30] A.A. Bardin, A..I Kotov, G.V. Shilov, L.I. Buravov, "Synthesis, Conductivity, and the Crystal Structure of a New Stable Metal, b"-(DOEO)2HSeO4 H2O," *Crystallog. Rep.*, vol. 50, p. 928, 2005.

[31] A. A. Bardin, A. I. Kotov, L. I. Buravov, S. S. Khasanov, R. P. Shibaeva, "Metal–Insulator Interplays Rendered by Lattice Transformations and Structural Disorder in DOEO Salts," *Eur. J. Inorg. Chem.*, vol. 24, p. 4017, 2014.

[32] A.A. Bardin, A.I. Kotov, S.S. Khasanov, G.V. Shilov, L.I. Buravov, L. Ouahab, E.B. Yagubskii, "The Radical-Cation Salt (DOEO)4[HgBr]4TCE: Synthesis, Structure and Conductivity," *Rus. J. Coord. Chem.*, vol. 32, p. 88, 2006.

[33] J. P. Pouget, "Bond and charge ordering in low-dimensional organic conductors," *Physica B*, vol. 407, p. 1762, 2012.

[34] Z. Z. Wang, J. C. Girard, C. Pasquier, D. Jérome, K. Bechgaard, "Scanning tunneling microscopy in TTF-TCNQ: Phase and amplitude modulated charge density waves," *Phys. Rev. B*, vol. 67, p. 121401, 2003.

[35] K. Yamaji, S. Megtert and R. Comes, "2D displacement pattern in TSeF-TCNQ model analysis of the 2k F diffuse lines," *J. Phys. France*, vol. 42, pp. 1327-1343, 1981.

[36] K. Yamaji, J.P. Pouget, R. Cornes and K. Becngaard, "Analysis of 2kF X-ray diffuse scattering intensity in HMTSF-TCNQ," *J. Phys. Colloques*, vol. 44, pp. C3-1321-C3-1323, 1983.

[37] J. P. Pouget, S. K. Khanna, F. Denoyer, R. Comès, A. F. Garito, and A. J. Heeger, "X Ray Observation of 2kF and 4kF Scatterings in Tetrathiafulvalene-Tetracyanoquinodimethane (TTF-TCNQ)," *Phys. Rev. Lett.*, vol. 37, p. 437, 1976.

[38] S. Kagoshima, T. Ishiguro, and H. Anzai, "X-Ray Scattering Study of Phonon Anomalies and Superstructures in TTF-TCNQ," *J. Phys. Soc. Japan*, vol. 41, p. 2061, 1976.

[39] H.M. McConnell, B.M. Hoffman and R.M. Metzger, "Charge transfer in molecular crystals," *Proc. Natl. Acad. Sci.*, vol. 53, pp. 46-50, 1965.

[40] G. Saito, J.P. Ferraris, "Requirements for an "Organic Metal"," *Bull. Chem. Soc. Jpn.*, vol. 53, pp. 2141-2145, 1980.

[41] G. Saito, T. Murata, "Mixed valency in organic charge transfer complexes," *Phil. Trans. R. Soc. A*, vol. 366, pp. 139-150, 2008.

[42] B. T. Matthias, H. Suhl, and E. Corenzwit, "Spin Exchange in Superconductors," *Phys. Rev. Lett.*, vol. 1, pp. 92-94, 1959.

[43] E. Coronado, P. Day, "Magnetic molecular conductors," *Chem. Rev.*, vol. 104, pp. 5419-5448, 2004.

[44] D. Jerome, "The physics of organic superconductors," *Science,* vol. 252, pp. 1509-1514, 1991.

[45] L. Balicas, K. Behnia, W. Kang, P. Auban-Senzier, E. Canadell, D. Jerome, "(TMTTF)2Br: The First Organic Superconductor in the (TMTTF)2X Family," *Adv. Mater.,* vol. 6, pp. 762-765, 1994.

[46] T. Takahashi, D. Jérome and K. Bechgaard, "Observation of a magnetic state in the organic superconductor (TMTSF) 2ClO4 : influence of the cooling rate," *Journal de Physique Lettres,* vol. 43, pp. 565-574, 1982.

[47] A. M. Kini , U. Geiser , H. H. Wang , K. D. Carlson , J. M. Williams , W. K. Kwok , K. G. Vandervoort , J. E. Thompson , D. L. Stupka, "A new ambient-pressure organic superconductor, .kappa.-(ET)2Cu[N(CN)2]Br, with the highest transition temperature yet observed (inductive onset Tc = 11.6 K, resistive onset = 12.5 K)," *Inorg. Chem.,* vol. 29, pp. 2555-2557, 1990.

[48] J. Bardeen, L. N. Cooper, and J. R. Schrieffer, "Theory of Superconductivity," *Phys. Rev.,* vol. 108, p. 1175, 1957.

[49] J. Bardeen, L. N. Cooper, and J. R. Schrieffer, "Microscopic Theory of Superconductivity," *Phys. Rev.,* vol. 106, p. 162, 1957.

[50] M. K. Wu, J. R. Ashburn, C. J. Torng, P. H. Hor, R. L. Meng, L. Gao, Z. J. Huang, Y. Q. Wang, and C. W. Chu, "Superconductivity at 93 K in a new mixed-phase Y-Ba-Cu-O compound system at ambient pressure," *Phys. Rev. Lett.,* vol. 58, p. 908, 1987.

[51] F. Steglich, J. Aarts, C. D. Bredl, W. Lieke, D. Meschede, W. Franz, and H. Schäfer, "Superconductivity in the Presence of Strong Pauli Paramagnetism: CeCu2Si2," *Phys. Rev. Lett.,* vol. 43, p. 1892, 1979.

[52] H. R. Ott, H. Rudigier, Z. Fisk, and J. L. Smith, "UBe13: An Unconventional Actinide Superconductor," *Phys. Rev. Lett.,* vol. 50, p. 1595, 1983.

[53] I. Askerzade, Unconventional Superconductors, Springer-Verlag Berlin Heidelberg, 2012.

[54] I. Zeljkovic and J. E. Hoffman, "Interplay of chemical disorder and electronic inhomogeneity in unconventional superconductors," *Phys. Chem. Chem. Phys.,* vol. 15, p. 13462, 2013.

[55] J. Wosnitza, "Superconductivity in layered organic metals," *Crystals,* vol. 2, pp. 248-265, 2012.

[56] T. Adachi, E. Ojima, K. Kato, H. Kobayashi, T. Miyazaki, M. Tokumoto, A. Kobayashi, "Superconducting Transition of (TMTTF)2PF6 above 50 kbar [TMTTF = Tetramethyltetrathiafulvalene]," *J. Am. Chem. Soc.,* vol. 122, pp. 3238-3239, 2000.

[57] H.H. Wang, K.D. Carlson, U. Geiser, A.M. Kini, A.J. Schultz, J.M. Williams, L.K. Montgomery, W.K. Kwok, U. Welp, K.G. Vandervoort, S.J. Boryschuk, A.V.Strieby Crouch, J.M. Kommers, D.M. Watkins, J.E. Schriber, D.L. Overmyer, D. Jung, J.J. Novoa, M.-H. Wha, "New κ-phase materials, κ-(ET)2Cu[N(CN)2]X.X=Cl, Br and I. The synthesis, structure and superconductivity above 11 K in the Cl (Tc = 12.8 K, 0.3 kbar) and Br(Tc = 11.6 K) salts," *Synthetic Metals,* vol. 42, pp. 1983-1990, 1991.

[58] J.-P. Pouget, P. Foury-Leylekian, P. Alemany, E. Canadell, "Charge ordering in low dimensional organic conductors: Structural aspects," *Phys. Status Solidi,* vol. 249, pp. 937-942, 2012.

[59] P. Foury-Leylekian, S. Petit, G. Andre, A. Moradpour, J.P. Pouget, "Neutron scattering evidence for a lattice displacement at the charge ordering transition of (TMTTF)2PF6," *Phys. B: Cond. Mat.,* vol. 405, p. S95–S97, 2010.

[60] P. Lunkenheimer, B. Hartmann, M. Lang, J. Müller, D. Schweitzer, S. Krohns, and A. Loidl, "Ferroelectric properties of charge-ordered α−(BEDT−TTF)2I3," *Phys. Rev. B,* vol. 91, p. 245132, 2015.

[61] M. de Souza, J.-P. Pouget, "Charge ordering transition in (TMTTF)2X explored by dilatometry," *J. Phys.: Condens. Matter,* vol. 25, p. 343201, 2013.

[62] J. Hubbard, "Generalized Wigner lattices in one dimension and some applications to tetracyanoquinodimethane (TCNQ) salts," *Phys. Rev. B*, vol. 17, pp. 494-505, 1978.

[63] B. J. Powell, R. H. McKenzie, "Strong electronic correlations in superconducting organic charge transfer salts," *J. Phys.: Condens. Matter*, vol. 18, pp. R827-R866, 2006.

[64] K. Miyagawa, K. Kanoda, A. Kawamoto, "NMR studies on two-dimensional molecular conductors and superconductors: Mott transition in k-(BEDT-TTF)2X," *Chem. Rev.,* vol. 104, pp. 5635-5653, 2004.

[65] M. de Souza, L. Bartosch, "Probing the Mott physics in k-(BEDT-TTF)2X salts via thermal expansion," *J. Phys.: Condens. Matter,* vol. 27, p. 053203, 2015.

[66] T. Sasaki, "Mott-Anderson Transition in Molecular Conductors: Influence of Randomness on Strongly Correlated Electrons in the κ-(BEDT-TTF)2X System," *Crystals*, vol. 2, pp. 374-392, 2012.

[67] V. Gantmakher, Electrons in disordered media, Moscow: FIZMATLIT, 2013.

[68] M. Dressel, "Ordering phenomena in quasi-one-dimensional organic conductors," *Naturwissenschaften*, vol. 94, pp. 527-541, 2007.

[69] J. B. Torrance, J. E. Vazquez, J. J. Mayerle, and V. Y. Lee, "Discovery of a Neutral-to-Ionic Phase Transition in Organic Materials," *Phys. Rev. Lett.*, vol. 46, pp. 253-257, 1981.

[70] Y. Otsuka, H. Seo, K. Yoshimi, T. Kato, "Neutral-ionic transition and ferroelectricity in charge-transfer complex: QMC study," in *International School and Workshop on Electronic Crystals*, Corsica, 2011.

[71] J. Clarke, A. I. Braginski, The SQUID Handbook, Weinheim: WILEY-VCH Verlag GmbH & Co. KGaA, 2004.

[72] M. McElfresh, Fundamentals of magnetism and magnetic measurements featuring Quantum Design's magnetic property measurement system, Perdue University, 1994.

[73] B.S. Deaver Jr., W.M. Fairbank, "Experimental evidence for quantized flux in superconducting cylinders," *Phys. Rev. Lett.*, vol. 7, p. 43, 1961.

[74] B. M. Weckhuysen, R. Heidler, R. A. Schoonheydt, "Electron Spin Resonance Spectroscopy," in *Molecular Sieves. Series 4.*, Heidelberg, Springer-Verlag Berlin, 2004, pp. 295-335.

[75] C. Poole, Jr., H. A. Farach, Handbook of electron spin resonance, Berlin Heidelberg: Springer-Verlag New York, 1999.

[76] A. S. Chernenkaya, O. V. Koplak, A. I. Kotov, R. B. Morgunov, E. B. Yagubskii, "Two types of charge carrier localization centers in (DOEO)4[HgBr4] · TCE single crystals," *Physics of the Solid State*, vol. 54, pp. 2391-2394, 2012.

[77] S. D. Jackson and J. S. J. Hargreaves, Metal oxyde catalysis, Weinheim: WILEY-VCH Verlag GmbH & Co. KGaA, 2009.

[78] F. Reinert, S. Hüfner, "Photoemission spectroscopy - from early days to recent applications," *New Journal of Physics*, vol. 7, p. 97, 2005.

[79] C. Fadley, "Basic Concepts of X-ray Photoelectron Spectroscopy," in *Electron Spectroscopy: Theory, Techniques and Applications*, Academic Press, 1978, pp. 2-157.

[80] C. Fadley, "X-ray photoelectron spectroscopy: Progress and perspectives," *J. Electron. Spectrosc. Relat. Phenom.*, vol. 178, p. 2, 2010.

[81] M. P. Seah, W. A. Dench, "Quantitative electron spectroscopy of surfaces: A standard data base for electron inelastic mean free paths in solid," *Surf. Interface Anal.*, vol. 1, p. 2, 1979.

[82] J. Strempfer, S. Francoual, D. Reuther, D. K. Shukla, A. Skaugen, H. Schulte-Schrepping, T. Kracht and H. Franz, "Resonant scattering and diffraction beamline P09 at PETRA III," *J. Synchrotron Rad.*, vol. 20, pp. 541-549, 2013.

[83] A. Gloskovskii, G. Stryganyuk, G. H. Fecher, C. Felser, S. Thiess, H. Schulz-Ritter, W. Drube, G. Berner, M. Sing, R. Claessen, M. Yamamoto, "Magnetometry of buried layers—Linear magnetic dichroism and spin detection in angular resolved hard X-ray photoelectron spectroscopy," *J. Electron. Spectrosc. Relat. Phenom.*, vol. 185, p. 47, 2012.

[84] J. Stöhr, NEXAFS spectroscopy. Springer Series in Surface Science, Springer: Heidelberg, 1992.

[85] G. Hähner, "Near edge X-ray absorption fine structure spectroscopy as a tool to probe electronic and structural properties of thin organic films and liquids," *Chem. Soc. Rev.*, vol. 35, p. 1244, 2006.

[86] A. Chernenkaya, K. Medjanik, P. Nagel, M. Merz, S. Schuppler, E. Canadell, J.-P. Pouget, G. Schönhense, "Nature of the empty states and signature of the charge density wave instability and upper Peierls transition of TTF-TCNQ by temperature-dependent NEXAFS spectroscopy," *Eur. Phys. J. B*, vol. 88, p. 13, 2015.

[87] M. Sing, J. Meyer, M. Hoinkis, S. Glawion, P. Blaha, G. Gavrila, C. S. Jacobsen, R. Claessen, "Structural vs electronic origin of renormalized band widths in TTF-TCNQ: An angular dependent NEXAFS study," *Phys. Rev. B*, vol. 76, p. 245119, 2007.

[88] J. Fraxedas, Y. J. Lee, I. Jimenez, R. Gago, R. M. Nieminen, P. Ordejón, and E. Canadell, "Characterization of the unoccupied and partially occupied states of TTF-TCNQ by XANES and first-principles calculations," *Phys. Rev. B*, vol. 68, p. 195115, 2003.

[89] K. Medjanik, D. Chercka, P. Nagel, M. Merz, S. Schuppler, M. Baumgarten, K. Müllen, S. A. Nepijko, H. J. Elmers, G. Schönhense, H. O. Jeschke, R. Valenti,

"Orbital-Resolved Partial Charge Transfer from the Methoxy Groups of Substituted Pyrenes in Complexes with Tetracyanoquinodimethane—A NEXAFS Study," *J. Am. Chem. Soc.*, vol. 134, pp. 4694-4699, 2012.

[90] J. Stöhr, R. Jaeger, J. Feldhaus, S. Brennan, D. Norman, and G. Apai, "Extended absorption fine structure studies above the carbon, nitrogen, oxygen, and fluorine K absorption edges," *Applied Optics*, vol. 19, pp. 3911-3919, 1980.

[91] R. J. Elliott, "Intensity of Optical Absorption by Excitons," *Phys. Rev.*, vol. 108, p. 1384, 1957.

[92] L. G. Parrat, "Electronic Band Structure of Solids by X-Ray Spectroscopy," *Rev. Mod. Phys.*, vol. 31, p. 616, 1959.

[93] P. R. Bevington, D. K. Robinson, Data reduction and error analysis for the physical sciences, New York: McGraw-Hill, 1979.

[94] J. Fraxedas, S. Molas, A. Figueras, I. Jimenes, R. Gago, P. Auban-Senzier, and M. Goffman, "Thin Films of Molecular Metals TTF-TCNQ," *J. Solid St. Chem.*, vol. 168, p. 384, 2002.

[95] J.S. Chappel, A.N. Bloch, W.A. Bryden, M. Maxfield, T.O. Poehler, D.O. Cowan, "Degree of charge transfer in organic conductors by infrared absorption spectroscopy," *J. Am. Chem. Soc.*, vol. 103, p. 2442, 1981.

[96] B. Stuart, Infrared spectroscopy: fundamentals and applications, Wiley, 2004.

[97] J.M. Hollas, Modern spectroscopy, Wiley, 2004.

[98] Y. J. Lee, R. M. Nieminen, P. Ordejon, and E. Canadell, "First-principles characterization of the electronic structure of the molecular superconductor β−(BEDT−TTF)2IBr2," *Phys. Rev. B*, vol. 67, p. 180505(R), 2003.

[99] W. Kohn and L. J. Sham, "Self-Consistent Equations Including Exchange and Correlation Effects," *Phys. Rev.*, vol. 140, p. A1133, 1965.

[100] P. Ordejón, E. Artacho, and J. M. Soler, "Self-consistent order-N density-functional calculations for very large systems," *Phys. Rev. B*, vol. 53, p. R10441(R), 1996.

[101] J. M. Soler, E. Artacho, J. D. Gale, A. Garcia, J. Junquera, P. Ordejon, D. Sanchez-Portal, "The SIESTA method for ab initio order-N materials simulation," *J. Phys.: Condens. Matter*, vol. 14, p. 2745, 2002.

[102] J.P. Perdew, K. Burke, M. Enzerhof, "Generalized Gradient Approximation Made Simple," *Phys. Rev. Lett.*, vol. 77, p. 3865, 1996.

[103] N. Troullier and J. L. Martins, "Efficient pseudopotentials for plane-wave calculations," *Phys. Rev. B*, vol. 43, p. 1993, 1991.

[104] L. Kleinman and D. M. Bylander, "Efficacious Form for Model Pseudopotentials," *Phys. Rev. Lett.*, vol. 48, p. 1425, 1982.

[105] S. G. Louie, S. Froyen, and M. L. Cohen, "Nonlinear ionic pseudopotentials in spin-density-functional calculations," *Phys. Rev. B*, vol. 26, p. 1738, 1982.

[106] E. Runge and E. K. U. Gross, "Density-Functional Theory for Time-Dependent Systems," *Phys. Rev. Lett.*, vol. 52, p. 997, 1984.

[107] M. A. Marques, N. T. Maitra, F. M. Nogueira, E. Gross, A. Rubio, Fundamentals of Time-Dependent Density Functional Theory, Heidelberg: Springer-Verlag Berlin, 2012.

[108] F. Nesse, "The ORCA program system," *WIREs Comput Mol Sci*, vol. 2, pp. 73-78, 2012.

[109] P. Blaha, K. Schwarz, G. K. H. Madsen, D. Kvasnicka, J. Luitz, WIEN2K, An Augmented Plane Wave + Local Orbitals Program for Calculating Crystal Properties, Karlheinz Schwarz, Techn. Universitaet Wien, 2001.

[110] K. Koepernik, H. Eschrig, "Full-potential nonorthogonal local-orbital minimum-basis band-structure scheme," *Phys. Rev. B*, vol. 59, p. 1743, 1999.

[111] F. de Groot, R. K. Hocking, C. Piamonteze, B. Hedman, K. Hodgson, E. Solomon, "New Developments in Charge Transfer Multiplet Calculations: Projection Operators, Mixed-Spin States and π-Bonding," in *13th International Conference On X-Ray Absorption Fine Structure (XAFS13)*, Stanford, California, USA, 2006.

[112] A. Lapinski, A.I. Kotov, "Optical properties of the conducting salt (DOEO)4HgBr4 TCE," *Chem. Phys.*, vol. 326, p. 551, 2006.

[113] A. Lapinski, A. Gasecka, A. Graja, et al., "Spectral investigation of the phase-transition behavior in (DOEO)4HgBr4TCE salt," *Opt. Mater.*, vol. 34, p. 1651, 2012.

[114] A. Lapinski, A.I. Kotov, "TD-DFT investigation of the electronic spectra of (DOEO)4HgBr4 TCE salt," *Mol. Phys.*, vol. 106, p. 33, 2008.

[115] A. Chernenkaya, Organic conductors. Localization of charge carriers in the compounds based on BEDT-TTF, Saarbrucken, Germany: LAP LAMBERT Academic Publishing GmbH & Co., 2011.

[116] A. Chernenkaya, O.V. Koplak, K. Medjanik, A.I. Kotov, R. Morgunov, E. Yagubskii, H.-J. Elmers, G. Schoenhense, "Temperature dependence of electronic and magnetic properties of (DOEO)4[HgBr4]·TCE single crystals," *Physics of the Solid State,* vol. 54, p. 2391, 2012.

[117] R. B. Morgunov, A. I. Dmitriev, A. S. Chernenkaya, K. Yakushi, K. Yamamoto, Y. Tanimoto, "Spin Dynamics of Charge Carriers in the Process of Their Localization in α'(BEDT–TTF)2IBr2 Single Crystals," *J. Exper. Theor. Phys.*, vol. 111, p. 857, 2010.

[118] O. Kahn, Molecular Magnetism, VCH. Publishers Inc., New York, 1993.

[119] S. Diehl, T. Methfessel, U. Tutsch, J. Müller, M. Lang, M. Huth, M. Jordan, H.-J. Elmers, "Disorder-induced gap in the normal density of states of the organic superconductor -(BEDTTTF)2Cu[N(CN)2Br," *J. Phys.: Condens. Matter,* vol. 27, p. 265601, 2015.

[120] J. R. Anderson, G. Kido, Y. Nishina, M. Górska, L. Kowalczyk, Z. Golacki, "In8uence of pair-exchange interaction on the magnetization of IV-VI-compound diluted magnetic semiconductors," *Phys. Rev. B,* vol. 41, p. 1014, 1990.

[121] M. Sing, U. Schwingenschlögl, R. Claessen, M. Dressel, and C. S. Jacobsen, "Surface characterization and surface electronic structure of organic quasi-one-dimensional charge transfer salts," *Phys. Rev. B*, vol. 67, p. 125402, 2003.

[122] Y. Iwasa, K. Mizuhashi, T. Koda, Y. Tokura, G. Saito, "Metal-insulator transition and antiferromagnetic order in bis(ethylenedithio)tetrathiafulvalene tetracyanoquinodimethane (BEDT-TTF)(TCNQ)," *Phys. Rev. B,* vol. 49, p. 3580, 1994.

[123] S. Yasin, M. Dumm, B. Salameh, P. Batail, C. Meźière, M. Dressel, "Transport studies at the Mott transition of the two-dimensional organic metal κ-(BEDT-TTF)2Cu[N(CN)2]BrxCl1-x," *Eur. Phys. J. B,* vol. 79, p. 383, 2011.

[124] E.M. Conwell (Editor) , Highly Conducting Quasi-One-Dimensional Organic Crystals, Semiconductors and Semimetal, New York: Academic Press, Vol. 27, 1988.

[125] S. K. Khanna, J. P. Pouget, R. Comès, A. F. Garito, and A. J. Heeger, "X-ray studies of 2kF and 4kF anomalies in tetrathiafulvalene-tetracyanoquinodimethane (TTF-TCNQ)," *Phys. Rev. B,* vol. 16, p. 1468, 1977.

[126] F. Zwick, D. Jérome, G. Margaritondo, M. Onellion, J. Voit, and M. Grioni, "Band Mapping and Quasiparticle Suppression in the One-Dimensional Organic Conductor TTF-TCNQ," *Phys. Rev. Lett.*, vol. 81, p. 2974, 1998.

[127] M. Grioni, S. Pons, and E. Frantzeskakis, "Recent ARPES experiments on quasi-1D bulk materials and artificial structures," *J. Phys.: Condens. Matter,* vol. 21, p. 023201, 2009.

[128] D. Jérome, "Organic conductors : from charge density wave TTF-TCNQ to superconducting," *Chem. Rev.*, vol. 104, p. 5565, 2004.

[129] J. P. Pouget, "X-ray diffuse scattering as precursor of incommensurate Peierls transitions in one-dimensional organic charge transfer conductors," *Z. Kristallogr.*, vol. 219, p. 711, 2004.

[130] Y. Bouveret, and S. Megtert, "Structural determination of the lowest temperature modulated phase," *Journal de Physique,* vol. 50, p. 1649, 1989.

[131] G. Shirane, S. M. Shapiro, R. Comès, A. F. Garito, and A. J. Heeger, "Phonon dispersion and Kohn anomaly in tetrathiafulvalene-tetracyanoquinodimethane (TTF-TCNQ)," *Phys. Rev. B,* vol. 14, p. 2325, 1976.

[132] J. E. Eldridge, Y. Lin, T. C. Mayadunne, L. K. Montgomery, S. Kaganov, and T. Miebach, "Resonant Raman scattering from a charge-density-wave system (TTF-TCNQ)," *Solid State Commun.*, vol. 105, p. 427, 1998.

[133] K. Murata, K. Yokogawa, S. Arumugam, H. Yoshino, "Pressure Effect on Organic Conductors," *Crystals,* vol. 2, p. 1460, 2012.

[134] W. D. Grobman, and B. D. Silverman, "Intramolecular screening of crystal fields and the X-ray-photoemission determination of charge transfer in TTF-TCNQ," *Solid State Commun.*, vol. 19, p. 319, 1976.

[135] C. Rojas, J. Caro, M. Grioni, and J. Fraxedas, "Surface characterization of metallic molecular organic thin films: tetrathiafulvalene tetracyanoquinodimethane," *Surface Science,* vol. 482, p. 546, 2001.

[136] J. M. Williams, J. R. Ferraro, R. J. Thorn, K. D. Carlson, U. Geiser, H. H. Wang, A. M. Kini and M.-H. Whangbo, Organic Superconductors, Prentice Hall, Englewood Cliffs, 1992.

[137] R. Claessen, M. Sing, U. Schwingenschlögl, P. Blaha, M. Dressel, C. S. Jacobsen, "Spectroscopic Signatures of Spin-Charge Separation in the Quasi-One-Dimensional Organic Conductor TTF-TCNQ," *Phys. Rev. Lett.*, vol. 88, p. 096402, 2002.

[138] M. Sing, U. Schwingenschlögl, R. Claessen, P. Blaha, J. M. P. Carmelo, L. M. Martelo, M. Dressel, C. S. Jacobsen, "Electronic structure of the quasi-one-dimensional organic conductor TTF-TCNQ," *Phys. Rev. B,* vol. 68, p. 125111, 2003.

[139] M. Rudloff, K. Ackermann, M. Huth, H.O. Jeschke, M. Tomic, "Charge transfer tuning by chemical substitution and uniaxial pressure in the organic complex tetramethoxypyrene–tetracyanoquinodimethane," *Phys. Chem. Chem. Phys.,* vol. 17, p. 4118, 2015.

[140] M. M. Alam, S. A. Jenekhe, "Efficient Solar Cells from Layered Nanostructures of Donor and Acceptor Conjugated Polymers," *Chem. Mater.,* vol. 16, pp. 4647-4656, 2004.

[141] X. Guo, M. Baumgarten, K. Müllen, "Designing π-conjugated polymers for organic electronics," *Prog. Polym. Sci.,* vol. 38, p. 1832, 2013.

[142] A. Mishra, C.Q. Ma, P. Bäuerle, "Functional Oligothiophenes: Molecular Design for Multidimensional Nanoarchitectures and Their Applications," *Chem. Rev.,* vol. 109, p. 1141, 2009.

[143] P. Gao, D. Beckmann, H. N. Tsao, X. Feng, V. Enkelmann, M. Baumgarten, W. Pisula, K. Müllen, "Dithieno[2,3- d ;2′,3′- d ′]benzo[1,2- b ;4,5- b ′]dithiophene (DTBDT) as Semiconductor for High-Performance, Solution-Processed Organic Field-Effect Transistors," *Adv. Mater.,* vol. 21, pp. 213-216, 2009.

[144] D. Bayer, S. Diehl, M. Baumgarten, K, Muellen, T. Methfessel, H. J. Elmers, "Tuning the hole injection barrier in the intermolecular charge-transfer compound DTBDT-F4TCNQ at metal interfaces," *Phys. Rev. B,* vol. 89, p. 175435, 2014.

[145] F.Rochet, F.Bournel, J.-J.Gallet, G.Dufour, L.Lozzi, F. Sirotti, "Electronic Structure of 1,3,5,7-Cyclooctatetraene Chemisorbed on Si(001)-2×1 at 300 K Studied by PES, NEXAFS, and Resonant Valence Band Spectroscopy," *J. Phys. Chem. B,* vol. 106, p. 4973, 2002.

[146] T. Miyamoto, Y. Kitajima, H. Sugawara, T. Naito, T. Inabe, K. Asakura, "Origin of Photochemical Modification of the Resistivity of Ag(DMe-DCNQI)2 Studied by X-ray Absorption Fine Structure," *J. Phys. Chem. C,* vol. 113, p. 20480, 2009.

[147] W. Chen, Q. D. Chen, H. Q. Li, H. Huang, W. Y. Zhan, S. Chen, G. X. Yu, S. W. A. Thye, "Molecular Orientation Dependent Energy Level Alignment at Organic−Organic Heterojunction Interfaces," *J. Phys. Chem. C,* vol. 113, p. 12839, 2009.

[148] P. Hohenberg and W. Kohn, "Inhomogeneous Electron Gas," *Phys. Rev.*, vol. 136, p. B864, 1964.

[149] B. Mahns, O. Kataeva, D. Islamov, S. Hampel, F. Steckel, C. Hess, M. Knupfer, B. Büchner, C. Himcinschi, T. Hahn, R. Renger, J. Kortus, "Crystal Growth, Structure, and Transport Properties of the Charge-Transfer Salt Picene/2,3,5,6-Tetrafluoro-7,7,8,8-tetracyanoquinodimethane," *Cryst. Growth Des.,* vol. 14, pp. 1338-1346, 2014.

[150] R.A. Laudise, Ch. Kloc, P.G. Simpkins, T. Siegrist, "Physical vapor growth of organic semiconductors," vol. 187, pp. 449-454, 1998.

[151] R. E. Long, R. A. Sparks and K. N. Trueblood, "The crystal and molecular structure of 7,7,8,8-tetracyanoquinodimethane," *Acta Crystallographica,* vol. 18, p. 932, 1965.

[152] T. J. Emge , M. Maxfield , D. O. Cowan, T. Kistenmacher, "Solution and Solid State Studies of Tetrafluoro-7,7,8,8-Tetracyano-p-Quinodimethane, TCNQF4. Evidence for Long-Range Amphoteric Intermolecular Interactions and Low-Dimensionality in the Solid State Structure," *Mol. Cryst. Liq. Cryst.,* vol. 65, p. 161, 1981.

[153] F. Neese, "The ORCA program system," *Comput. Mol. Sci.*, vol. 2, pp. 73-78, 2012.

[154] C. Hébert-Souche, P.-H. Louf, P. Blaha, M. Nelhiebel, J. Luitz, P. Schattschneider, K. Schwarz, B. Jouffrey, "The orientation-dependent simulation of ELNES," *Ultramicroscopy,* vol. 83, pp. 9-16, 2000.

[155] C. Hébert, "Practical aspects of running the WIEN2k code for electron spectroscopy," *Micron,* vol. 38, pp. 12-28, 2007.

[156] J. Luitz, M. Maier, C. Hébert, P. Schattschneider, P. Blaha, K. Schwarz and B. Jouffrey, "Partial core hole screening in the Cu L3 edge," *Eur. Phys. J. B,* vol. 21, pp. 363-367, 2001.

[157] T. J. Kistenmacher, T. J. Emge, A. N. Bloch and D. O. Cowan, "Structure of the red, semiconducting form of 4,4',5,5'-tetramethyl-Δ2,2'-bi-1,3-diselenole-7,7,8,8-tetracyano-p-quinodimethane, TMTSF–TCNQ," *Acta Crystallographica* , vol. 38, p. 1193, 1982.

[158] L. Zhu, E.-G. Kim, Y. Yi, and J.-L. Bredas, "Charge Transfer in Molecular Complexes with 2,3,5,6-Tetrafluoro-7,7,8,8-tetracyanoquinodimethane (F4-TCNQ): A Density Functional Theory Study," *Chemistry of Materials,* vol. 23, p. 5149, 2011.

[159] R. Bozio, I. Zanon, A. Girlando, C. Pecile, "Influence of the Intermolecular Charge Transfer Interaction on the Solution and Solid State Infrared Spectra of 7,7,8,8-Tetracyanoquinodimethane (TCNQ) Alkaline Salts," *J. Chem. Soc., Faraday Trans. 2: Mol. Chem. Phys.,* vol. 74, p. 235, 1978.

[160] Z. G. Soos, H. J. Keller, K. Ludolf, J. Queckbörner, D. Wehe, S. Flandrois, "Ionicity and paramagnetism of strong organic charge-transfer complexes," *J. Chem. Phys.,* vol. 74 (9), p. 5287, 1981.

[161] J. G. Robles-Martinez, A. Salmeron-Valverde, J. Arguelles-Ramirez and A. Zehe, "Variation of Charge Transfer in Zn-naphtholimines with TCNQ," *Molecular Engineering,* vol. 8, p. 411, 1999.

[162] P. Pingel, L. Zhu, K. S.k Park, J.-O. Vogel, S. Janietz, E.-G. Kim, J. P. Rabe, J.-L. Bredas, and N. Koch, "Charge-Transfer Localization in Molecularly Doped Thiophene-Based Donor Polymers," *J. Phys. Chem. Lett.,* vol. 1, p. 2037, 2010.

[163] A. Salmeron-Valverde, J. G. Roblez-Martinez, J. Garcia-Serrano, R. Gomez, R. M. Ridaura, M. Quintana, A. Zehe, "A Study of the Degree of Charge Transfer in TTF Molecular Complexes with Nitro-Carboxylated Fluorene Derivatives," *Molecular Engineering,* vol. 8, p. 419, 1999.

[164] Z. Iqbal, C. W. Christoe, and D. K. Dawson, "Infrared absorption and reflection studies of organic radical salt: K+TCNQ−," *J. Chem. Phys.,* vol. 63, p. 4485, 1975.

[165] M. Meneghetti and C. Pecile, "Charge–transfer organic crystals: Molecular vibrations and spectroscopic effects of electron–molecular vibration coupling of the strong electron acceptor TCNQF4," *The Journal of Chemical Physics,* vol. 84, p. 4149, 1986.

[166] T.-C. Tseng, C. Urban, Y. Wang, R. Otero, S. L. Tait, M. Alcamı, D. Écija, M. Trelka, J. M. Gallego, N. Lin, M. Konuma, U. Starke, A. Nefedov, A. Langner, C. Woll, M. A. Herranz, F. Martın, Nazario Martın, K. Kern, R. Miranda, "Charge-transfer-induced structural rearrangements at both sides of organic/metal interfaces," *Nature Chemistry,* pp. 374-379, 2010.

[167] R. D. Cowan and J. B. Mann, "Stabilization of solution of the Hartree–Fock equations," *J. Comput. Phys.,* vol. 16, pp. 160-166, 1974.

[168] A. Chernenkaya, A. Morherr, S. Backes, K. Medjanik, W. Popp, S. Witt, X. Kozina, S. A. Nepijko, G. Öhrwall, M. Bolte, C. Krellner, M. Baumgarten, H. J. Elmers, G. Schönhense, H. O. Jeschke, and R. Valentí, "Microscopic origin of the charge transfer in single crystals based on thiophene derivatives: a combined NEXAFS and density functional theory approach," *J. Am. Chem. Soc.,* 2016, submitted.

[169] S.V. Chernov, K. Medjanik, C. Tusche, D. Kutnyakhov, S.A. Nepijko, A. Oelsner, J. Braun, J. Minár, S. Borek, H. Ebert, H.J. Elmers, J. Kirschner, G. Schönhense, "Anomalous d-like surface resonances on Mo(110) analyzed by time-of-flight momentum microscopy," *Ultramicroscopy,* vol. 159, p. 453, 2015.

[170] V. Solovyeva, K. Keller and M. Huth, "Organic charge transfer phase formation in thin films of the BEDT-TTF/TCNQ donor–acceptor system," *Thin Solid Films,* vol. 517, pp. 6671-6676, 2009.

[171] K. Medjanik, D. Kutnyakhov, S. A. Nepijko, G. Schönhense, S. Naghavi, V. Alijani, C. Felser, N. Koch, R. Rieger, M. Baumgarten, K. Müllen, "Electronic structure of large disc-type donors and acceptors," *Phys. Chem. Chem. Phys.,* vol. 12, pp. 7184-7193, 2010.

[172] N. Koch, S. Duhm, J. P. Rabe, A. Vollmer, R. L. Johnson, "Optimized hole injection with strong electron acceptors at organic-metal interfaces," *Phys. Rev. Lett.,* vol. 95, p. 237601, 2005.

[173] S. Braun, W. R. Salaneck, "Fermi level pinning at interfaces with tetrafluorotetracyanoquinodimethane (F4-TCNQ): The role of integer charge transfer states," *Chem. Phys. Lett.,* vol. 438, pp. 259-262, 2007.

[174] W. Gao, A. Kahn, "Electronic structure and current injection in zinc phthalocyanine doped with tetrafluorotetracyanoquinodimethane: Interface versus bulk effects," *Organic electronics,* vol. 3, pp. 53-63, 2002.

[175] A. Kahn, N. Koch, W. Gao, "Electronic Structure and Electrical Properties of Interfaces between Metals and pi-Conjugated Molecular Films," *J. Polym. Sc.: Polym. Phys.,* vol. 41, pp. 2529-2548, 2003.

[176] D. Nanova, S. Beck, A. Fuchs, T. Glaser, C. Lennartz, W. Kowalsky, A. Pucci, M. Kroeger, "Charge transfer in thin films of donor–acceptor complexes studied by infrared spectroscopy," *Organic electronics,* vol. 13, pp. 1237-1244, 2012.

[177] F. Schlütter, F. Rossel, M. Kivala, V. Enkelmann, J.-P. Gisselbrecht, P. Ruffieux, R. Fasel, K. Müllen, "π-Conjugated Heterotriangulene Macrocycles by Solution and Surface-supported Synthesis toward Honeycomb Networks," *J. Am. Chem. Soc.,* vol. 135, pp. 4550-4557, 2013.

[178] M. Bieri, S. Blankenburg, M. Kivala, C. A. Pignedoli, P. Ruffieux, K. Müllen, R. Fasel, "Surface-supported 2D heterotriangulene polymers," *Chem. Commun.,* vol. 47, pp. 10239-10241, 2011.

[179] M. Bieri, M.-T. Nguyen, O. Gröning, J. Cai, M. Treier, K. Aït-Mansour, P. Ruffieux, C. A. Pignedoli, D. Passeroni, M. Kastler, K. Müllen, R. Fasel, "Two-

Dimensional Polymer Formation on Surfaces: Insight into the Roles of Precursor Mobility and Reactivity," *J. Am. Chem. Soc.*, vol. 132, pp. 16669-16676, 2010.

[180] E. F. Aziz, A. Vollmer, S. Eisebitt, W. Eberhard, P. Pingel, Dieter Neher, N. Koch, "Localized Charge Transfer in a Molecularly Doped Conducting Polymer," *Adv. Mater.*, vol. 19, pp. 3257-3260, 2007.

[181] O. Rana, R. Srivastava, G. Chauhan, M. Zulfequar, M. Husain, P. C. Srivastava, M. N. Kamalasanan, "Modification of metal–organic interface using F4-TCNQ for enhanced hole injection properties in optoelectronic devices," *Phys. Status Solidi A*, vol. 209, pp. 2539-2545, 2012.

[182] S. Braun, X. Liu, W. R. Salaneck, M. Fachlman, "Fermi level equilibrium at donor–acceptor interfaces in multi-layered thin film stack of TTF and TCNQ," *Organic Electronics,* vol. 11, pp. 212-217, 2010.

[183] N. Koch, "Energy levels at interfaces between metals and conjugated organic molecules," *J. Phys.: Condens. Matter,* vol. 20, p. 184008, 2008.

[184] M. Kivala, W. Pisula, S. Wang, A. Marwinskiy, J.-P. Gisselbreicht, X. Feng, K. Müllen, "Columnar Self-Assembly in Electron-Deficient Heterotriangulenes," *Chem. Eur. J.*, vol. 19, pp. 8117-8128, 2013.

[185] S. Wang, M. Kivala, I. Lieberwirth, K. Kirchhoff, X. Feng, W. Pisula, K. Müllen, "Dip-coating-induced fiber growth of a soluble heterotriangulene," *Chem. Phys. Chem.*, vol. 12, pp. 1648-1651, 2011.

[186] N. Makarov, S. Mukhopadhyay, K. Yesudas, J.-L. Brédas, J. W. Perry, A. Pron, M. Kivala, K. Müllen, "Impact of Electronic Coupling, Symmetry, and Planarization on One- and Two-Photon Properties of Triarylamines with One, Two, or Three Diarylboryl Acceptors," *J. Phys. Chem. A,* vol. 116, pp. 3781-3793, 2012.

[187] R. Liu, C. von Malotki, L. Arnold, N. Koshino, H. Higashimura, M. Baumgarten, and K. Müllen, "Triangular Trinuclear Metal-N4 Complexes with High Electrocatalytic Activity for Oxygen Reduction," *J. Am. Chem. Soc.*, vol. 133, pp. 10372-10375, 2011.

[188] P. O. Dral, M. Kivala, T. Clark, "Doped Polycyclic Aromatic Hydrocarbons as Building Blocks for Nanoelectronics: A Theoretical Study," *J. Org. Chem.*, vol. 78, pp. 1894-1902, 2013.

[189] P. A. Anderson, "Work Function of Gold," *Phys. Rev.*, vol. 115, p. 553, 1959.

[190] W.M.H. Sachtler, G.J.H. Dorgelo, A.A. Holscher, "The work function of gold," *Surface Science,* vol. 5, pp. 221-229, 1966.

[191] A. D. Becke, "Density-functional exchange-energy approximation with correct asymptotic behavior," *Phys. Rev. A,* vol. 38, pp. 3098-3100, 1988.

[192] J. P. Perdew, "Density-functional approximation for the correlation energy of the inhomogeneous electron gas," *Phys. Rev. B,* vol. 33, p. 8822, 1986.

[193] A. Schkifer, H. Horn, R. Ahlrichs , "Fully optimized contracted Gaussian basis sets for atoms Li to Kr," *J. Chem. Phys.,* vol. 97, p. 2571, 1992.

[194] F. Weigend, R. Ahlrichs, "Balanced basis sets of split valence, triple zeta valence and quadruple zeta valence quality for H to Rn: Design and assessment of accuracy," *Phys. Chem. Chem. Phys.,* vol. 7, pp. 3297-3305, 2005.

[195] S. Grimme, J. Antony, S. Ehrlich, H. Krieg, "A consistent and accurate ab initio parametrization of density functional dispersion correction (DFT-D) for the 94 elements H-Pu," *J. Chem. Phys.,* vol. 132, p. 154104, 2010.

[196] S. Grimme, S. Ehrlich, L. Goerigk, "Effect of the Damping Function in Dispersion Corrected Density Functional Theory," *J. Comput. Chem.,* vol. 32, p. 1456, 2011.

[197] M. Baumgarten, *Private communications*, 2013.

[198] K. Medjanik, A. Chernenkaya, X. Kozina, S.A. Nepijko, G. Öhrwall, P. Foury-Leylekian, P. Alemany, G. Schönhense, E. Canadell, J.-P. Pouget, "NEXAFS investigation of the unoccupied electronic levels in the Bechgaard salt (TMTSF)2PF6," *Phys. Chem. Chem. Phys.,* 2016, submitted.

[199] C. Bourbonnais, D. Jerome, "Electronic Confinement in Organic Metals," *Science,* vol. 281, p. 1155, 1998.

[200] M. d. Souza, Thermal Expansion and Transport Properties of Low-Dimensional Organic Conductors (PhD Thesis), 2008.

[201] A. Schwartz, M. Dressel, G. Gruener, V. Vescoli, L. Degiorgi, and T. Giamarchi, "On-chain electrodynamics of metallic (TMTSF)2X salts: Observation of Tomonaga-Luttinger liquid response," *Phys. Rev. B,* vol. 58, pp. 1261-1371, 1998.

[202] A. Pashkin, M. Dressel, M. Hanfland, and C. A. Kuntscher, "Deconfinement transition and dimensional crossover in the Bechgaard-Fabre salts: Pressure- and temperature-dependent optical investigations," *Phys. Rev. B,* vol. 81, p. 125109, 2010.

[203] P. Foury-Leylekian, S. Petit, I. Mirebeau, G. André, M. de Souza, M. Lang, E. Ressouche, A. Moradpour, and J.-P. Pouget, "Low-temperature structural effects in

the (TMTSF)2PF6 and AsF6 Bechgaard salts," *Phys. Rev. B*, vol. 88, p. 024105, 2013.

[204] D. Jérome, A. Mazaud, M. Ribault, K. Bechgaard, "Superconductivity in a synthetic organic conductor (TMTSF)2PF6," *J. Physique Lett.*, vol. 41, p. 95, 1980.

[205] [Online]. Available: http://departments.icmab.es/leem/siesta/.

[206] D. S. Chow, F. Zamborszky, B. Alavi, D. J. Tantillo, A. Baur, C. A. Merlic, and S. E. Brown, "Charge Ordering in the TMTTF Family of Molecular Conductors," *Phys. Rev. Lett.*, vol. 85, p. 1698, 2000.

[207] A. Morherr, S. Witt, A. Chernenkaya, G. Schönhense, J.-P. Bäcker, M. Bolte, C. Krellner, "Crystal Growth of new charge-transfer salts based on pi-conjugated donor molecules," *CrystEngComm*, 2016, submitted.

List of own publications

Parts of this work have been published in the following articles:

1. A. Chernenkaya, A. Morherr, S. Backes, W. Popp, S. Witt, X. Kozina, S. A. Nepijko, M. Bolte, K. Medjanik, G. Öhrwall, C. Krellner, M. Baumgarten, H. J. Elmers, G. Schönhense, H. O. Jeschke, and R. Valentí, Microscopic origin of the charge transfer in single crystals based on thiophene derivatives: a combined NEXAFS and density functional theory approach, *Journal of Chemical Physics*, **145**, 034702, 2016.
2. A. Chernenkaya, O. Koplak, K. Medjanik, A. Kotov, R. Morgunov, E. Yagubskii, H.-J. Elmers, G. Schönhense, Temperature dependence of electronic and magnetic properties of $(DOEO)_4[HgBr_4]\cdot TCE$ single crystals, *Solid State Phenomena*, **233-234**, 173-176, 2015.
3. A. Chernenkaya, K. Medjanik, P. Nagel, M. Merz, S. Schuppler, E. Canadell, J.-P. Pouget, G. Schönhense, Nature of the empty states and signature of the charge density wave instability and upper Peierls transition of TTF-TCNQ by temperature-dependent NEXAFS spectroscopy, *European Physical Journal B*, **88**, 13, 2015.
4. O.V. Koplak, A. Chernenkaya, K. Medjanik, A. Brambilla, A. Gloskovskii, A. Calloni, G. Schönhense, F. Ciccacci, R.B. Morgunov, Spectroscopic fingerprints for charge localization in the organic semiconductor $(DOEO)_4[HgBr_4]\cdot TCE$ *European Physical Journal B,* **88**, 120, 2015.
5. K. Medjanik, A. Chernenkaya, S. A. Nepijko, G. Öhrwall, P. Foury-Leylekian, P. Alemany, E. Canadell, G. Schönhense, J.-P. Pouget, Observation of the charge localization and charge ordering transitions in $(TMTTF)_2AsF_6$ using NEXAFS, *Physical Chemistry Chemical Physics*, **17**, 19202, 2015.
6. K. Medjanik, A. Chernenkaya, X. Kozina, S. A. Nepijko, G. Öhrwall, P. Foury-Leylekian, P. Alemany, G. Schönhense, E. Canadell, and J.-P. Pouget, NEXAFS investigation of the unoccupied electronic levels in the Bechgaard salt $(TMTSF)_2PF_6$ *Journal of Physical Chemistry A*, **120**, 8574–8583, 2016.

7. A. Morherr, S. Witt, A. Chernenkaya, G. Schönhense, J.-P. Bäcker, M. Bolte, and C. Krellner, Crystal Growth of new charge-transfer salts based on π-conjugated donor molecules, *Physica B* **496**, 98–105, 2016.

Other publications:

8. S.A. Nepijko, A. Chernenkaya, K. Medjanik, S.V. Chernov, M. Klimenkov, O.V. Vlasenko, S.S. Petrovskaya, L.V. Odnodvorets, Ya. V. Zaulichnyy, G. Schönhense Soft X-ray emission spectroscopy used for the characterization of aC and CN_x thin films, *Thin Solid Films*, **557**, 109-113, 2015.
9. S.A. Nepijko, A. Chernenkaya, K. Medjanik, S.V. Chernov, D.V. Shapko, I.Yu. Protsenko, W. Schulze, G. Schönhense Investigation of a Ge nanoparticle film by means of electron stimulated photon emission spectroscopy. *Journal of Electron Spectroscopy and Related Phenomena* **193**, 54, 2014.
10. H. J. Elmers, A. Chernenkaya, K. Medjanik, M. Emmel, G. Jakob, G. Schönhense, D. Gottlob, I. Krug, F. M. F. de Groot, A. Gloskovskii Exchange coupling in the correlated electronic states of amorphous GdFe films. *Physical Review B* **88**, 174407, 2013.
11. A. Chernenkaya, O. Koplak, A. Kotov, R. Morgunov, E. Yagubskii Two types of charge carriers localization centers in $(DOEO)_4[HgBr_4]TCE$. *Fizika Tverdogo Tela (Solid State Physics)*, **54**, 12, 2073-2077, 2012 (in Russian). *Physics of the Solid State* **54**, 12, 2391-2394, 2012.
12. A. Chernenkaya, A.I. Dmitriev, M. Kirman, O.V. Koplak, R.B. Morgunov ESR Spectra of Charge Carriers in the α'- and β- phases of $(BEDT\text{-}TTF)_2IBr_2$ Single Crystals, *Solid State Phenomena* **190**, 615-618, 2012.
13. A. Chernenkaya, M. Kirman, A. Dmitriev, R. Morgunov, O. Koplak, Y. Tanimoto Low-temperature Phase Transition Detected By ESR in α'-$(BEDT\text{-}TTF)_2IBr_2$ Single Crystals, *Applied Magnetic Resonance* **41**, 2-3,. 363-370, 2011.
14. M. Kirman, A. Dmitriev, A. Chernenkaya, R. Morgunov Low-temperature Phase Transition Detected By ESR in α'-$(BEDT\text{-}TTF)_2IBr_2$ Single Crystals (in Russian). *Fizika Tverdogo Tela (Solid State Physics)*, **53**, 6, 1203-1207, 2011.
15. A.I. Dmitriev, A.S. Chernenkaya, Spin dynamics and charge order-disorder phase transition detected by EPR in α’-$(BEDT\text{-}TTF)_2IBr_2$, *Magnetic resonance in solids*, **12**, 2, 17-21, 2010.

16. R. B. Morgunov, A. I. Dmitriev, A. S. Chernen'kaya, K. Yakushi, K. Yamamoto and Y. Tanimoto Spin Dynamics of Charge Carriers in the Process of Their Localization in α'-(BEDT–TTF)$_2$IBr$_2$ Single Crystals. *Zhurnal Eksperimental'noi i Teoreticheskoi Fiziki*, **138**, 4, 970–978, 2010 (in Russian). *Journal of Experimental and Theoretical Physics,* **111**, 5, 857–864, 2010.
17. R. Morgunov, A. Dmitriev, A. Chernenkaya, K. Yamamoto, K. Yakushi, Y. Tanimoto Charge order–disorder phase transition detected by EPR in α′-(BEDT-TTF)$_2$IBr$_2$, *Physica B: Condensed Matter*, **405**, 11(1), S138-S140, 2010.

Books and book chapters:

A. Chernenkaya Organic conductors. Localization of charge carriers in the compounds based on BEDT-TTF. LAP LAMBERT Academic Publishing GmbH & Co. Saarbrucken, Germany, 77 p., ISBN: 978-3-8454-0974-0, 2011 (in Russian).

Presented posters in conferences:

1. A. Chernenkaya, A. Morherr, K. Medjanik, S. Witt, X. Kozina, S.A. Nepijko, G. Öhrwall, M. Bolte C. Krellner, H. O. Jeschke, R. Valenti, M. Baumgarten, G. Schönhense, Orbital-selective NEXAFS: origin of the charge transfer in single crystals based on thiophene derivatives, *The 11th International Symposium on Crystalline Organic Metals Superconductors and Magnets (ISCOM2015),* Bad Gögging, Germany, September 06-11, 2015, p. 180.
2. A. Chernenkaya, K. Medjanik, R. Morgunov, P. Nagel, M. Merz, S. Schuppler, A. Gloskovskii, E. Yagubskii, G. Schönhense, Temperature-dependent NEXAFS and HAXPES: charge carrier localization in (DOEO)4[HgBr]4•TCE two-dimensional organic conductor, *International Winterschool on Electronic Properties of Novel Materials,* Kirchberg in Tirol, Austria, March 07 - 14, 2015, p. 47.
3. A. Chernenkaya, A. Kotov, K. Medjanik, A. Gloskovskii, P. Nagel, M. Merz, S. Schuppler, O. Koplak, R. Morgunov, E. Yagubskii, H. Elmers and G. Schönhense, Electron density redistribution as a result of magnetic ordering in (DOEO)$_4$[HgBr]$_4$TCE crystals, *59th annual conference on magnetism and magnetic materials*, Honolulu, Hawaii, November 3-7, 2014, p.848.
2. A. Chernenkaya, K. Medjanik, A. Kotov, P. Nagel, M. Merz, S. Schuppler, A. Gloskovskii, R. Morgunov, E. Yagubskii, H.J. Elmers, E. Canadell, J.-P. Pouget, M.

Baumgarten, G. Schönhense Charge carrier localization in $(DOEO)_4[HgBr]_4$•TCE and Peierls transition in TTF-TCNQ single crystals by temperature-dependent NEXAFS and HAXPES, *School on UV and X-ray Spectroscopies of Correlated Electron Systems*, Ecole de Physique des Houches, France, September 1-12, 2014, p.34.

3. A. Chernenkaya, A. Kotov, K. Medjanik, A. Gloskovskii, P. Nagel, M. Merz, S. Schuppler, R. Morgunov, E. Yagubskii, H.J. Elmers, G. Schönhense Electronic and magnetic properties of $(DOEO)_4[HgBr]_4$•TCE single crystals, *German Conference for Research with Synchrotron Radiation, Neutrons and Ion Beams at Large Facilities*, Bonn, Germany, September 21-23, 2014, ID 539.
4. A. Chernenkaya, A. Kotov, K. Medjanik, A. Gloskovskii, P. Nagel, M. Merz, S. Schuppler, R. Morgunov, E. Yagubskii, H.J. Elmers, G. Schönhense Temperature dependence of electronic and magnetic properties of $(DOEO)_4[HgBr]_4$•TCE single crystals *Moscow International Symposium on Magnetism*, Moscow, Russia, June 29 – Jule 04, 2014, p.760.
5. A. Chernenkaya, A. Kotov, K. Medjanik, A. Gloskovskii, P. Nagel, M. Merz, S. Schuppler, R. Morgunov, E. Yagubskii, H.J. Elmers, G. Schönhense Characterization of ambient pressure phases in $(DOEO)_4[HgBr]_4$•TCE. *2nd Internatioanal Symposiums on "Novel states in correlated condensed matter – from modelsystems to real materials"*, Königstein, Germany, April 08-10, 2014, p. 68.
6. A. Chernenkaya, K. Medjanik, M. Kivala, P. Nagel, M. Merz, S. Schuppler, T. Shubina, M. Baumgarten, K. Müllen, G. Schönhense Orbital-Resolved Near-Edge Adsorption Fine Structure (NEXAFS) on novel partial charge-transfer compounds based on triangulene derivatives, *2nd Internatioanal Symposiums on "Novel states in correlated condensed matter – from modelsystems to real materials"*, Königstein, Germany, April 08-10, 2014, p. 69.
7. A. Chernenkaya, S. Köhler, E. Gati, V. Ksenofontov, K. Medjanik, A. Kotov, R. Morgunov, E. Yagubskii, H.-J. Elmers, M. Lang, and G. Schönhense. Under-pressure measurements of resistivity and magnetic susceptibility and the pressure-temperature phase diagram of $(DOEO)_4[HgBr_4]$TCE organic charge-transfer crystals. *DPG Spring Meeting*, Dresden, Germany, March 30 – April 04, 2014, p. 443.
8. A. Chernenkaya, A. Kotov, K. Medjanik, A. Gloskovskii, O.V. Koplak, R.B. Morgunov, E. Yagubskii , H. J. Elmers, G. Schönhense. Temperature dependence of electronic and magnetic properties of $(DOEO)_4[HgBr_4]$ TCE single crystals. *The 10th*

International Symposium on Crystalline Organic Metals Superconductors and Magnets (ISCOM2013), Montreal, Canada, July 14-19, 2013, p. 134.

Talks:

1. A. Chernenkaya Spectroscopy on highly-correlated organic conductors, *Group seminary*, Physics department, University of Mainz, Germany, January 2016.
2. A. Chernenkaya, Series of lectures: (i) General introduction in photoemission and Near Edge X-Ray Absorption Fine Structure (NEXAFS) as measurement techniques; (ii) Using the photoemission methods and NEXAFS for investigating the low-temperature phase transition in high-correlated organic conductors. *Annual student seminar of Transregio SFB/TR49*, Cologne, Germany, October 07-09, 2015.
3. A. Chernenkaya, K. Medjanik, P. Nagel, M. Merz, S. Schuppler, E. Canadell, J.-P. Pouget, G. Schönhense. Temperature-dependent NEXAFS in TTF-TCNQ: nature of the empty electronic states of TCNQ and their thermal evolution due to the charge density wave instability, *Annual student seminar of Greaduate School of Excellence Materials Science in Mainz*, Lissbon, Portugal, October 01-05, 2015.
4. A. Chernenkaya, K. Medjanik, P. Nagel, M. Merz, S. Schuppler, E. Canadell, J.-P. Pouget, G. Schönhense. Temperature-dependent NEXAFS in TTF-TCNQ, *Annual Retreat of the SFB/TR49*, Langenselbold, Germany, September 24-25, 2015.
5. A. Chernenkaya, K. Medjanik, P. Nagel, M. Merz, S. Schuppler, E. Canadell, J.-P. Pouget, G. Schönhense, Nature of the empty electronic states of TCNQ and their thermal evolution due to the CDW instability of TTF-TCNQ revealed by NEXAFS, *Annual retreat Transregio SFB TR49*, Freiburg, Germany, April 08-10, 2015.
6. A. Chernenkaya, K. Medjanik, P. Nagel, M. Merz, S. Schuppler, E. Canadell, J.-P. Pouget, G. Schönhense, Nature of the empty electronic states of TCNQ and their thermal evolution due to the CDW instability of TTF-TCNQ revealed by NEXAFS, *DPG Spring Meeting*, Berlin, Germany, March 15-20, 2015, p. 496.
7. A. Chernenkaya, K. Medjanik, M. Kivala, P. Nagel, M. Merz, S. Schuppler, T. Shubina, M. Baumgarten, K. Müllen, and G. Schönhense. Investigation of novel partial charge-transfer compounds based on triangulene derivatives by ultraviolet photoelectron spectroscopy (UPS) and near-edge X-ray adsorption fine structure

(NEXAFS). *DPG Spring Meeting*, Dresden, Germany, March 30 – April 04, 2014, p. 346.

8. A. Chernenkaya Organic metals and superconductors. Phase diagram of $(DOEO)_4[HgBr_4]$, *Group seminary*, Physics department, University of Mainz, Germany, February 2014.
9. A. Chernenkaya, V. Ksenofontov, A. Kotov, O. Koplak, K. Medjanik, A. Gloskovskii, P. Nagel, M. Merz, S. Schuppler, R. Morgunov, E. Yagubskii, H.J. Elmers, G. Schönhense. Pressure induced transition from AFM insulator to SC ground state in (DOEO)4[HgBr]4·TCE, *Annual retreat Transregio SFB TR49*, Bensheim, Germany, September 19-20, 2013.
10. A. Chernenkaya, K. Medjanik, A. Kotov, A. Gloskovskii, O. Koplak, E. Yagubskii, G. Schönhense, R. Morgunov Particularities of Charge Carrier Localization in $(DOEO)_4[HgBr_4]\cdot$TCE Single Crystals. *DPG Spring Meeting*, Regensburg, Germany, March 10-15, 2013, p. 140.
11. A. Chernenkaya Organic metals. Charge carriers localization in $(DOEO)_4[HgBr_4]$ – *Group seminary*, Physics department, University of Mainz, Germany, December 2012.
12. A. Chernenkaya Charge carrier localization in $(BEDT\text{-}TTF)_2IBr_2$ family, *Group seminary*, Physics department, University of Mainz, Germany, February 2012.

Teaching activities:

- Winter Semester 2013/2014 – Assistant of Professor on lectures “Surface Physics”.
- Summer Semester 2014 – Tutor for the experiment “Field emission microscopy” in the frame of the advanced laboratory courses for physics students.
- Winter Semester 2014/2015 - Assistant of Professor on lectures “Surface Physics”.
- Winter Semester 2014/2015 - Supervisor of Bachelor student in Surface Physics.

Curriculum Vitae

Acknowledgment